

Summer 8-2014

Modeling that Leads to the Prediction of Photocatalytic Coatings Characterization

Biju Bajracharya
University of Southern Mississippi

Follow this and additional works at: <https://aquila.usm.edu/dissertations>



Part of the [Environmental Engineering Commons](#), and the [Other Computer Engineering Commons](#)

Recommended Citation

Bajracharya, Biju, "Modeling that Leads to the Prediction of Photocatalytic Coatings Characterization" (2014). *Dissertations*. 277.
<https://aquila.usm.edu/dissertations/277>

This Dissertation is brought to you for free and open access by The Aquila Digital Community. It has been accepted for inclusion in Dissertations by an authorized administrator of The Aquila Digital Community. For more information, please contact Joshua.Cromwell@usm.edu.

The University of Southern Mississippi

MODELING THAT LEADS TO
THE PREDICTION OF PHOTOCATALYTIC COATINGS CHARACTERIZATION

by

Biju Bajracharya

Abstract of a Dissertation
Submitted to the Graduate School
of The University of Southern Mississippi
in Partial Fulfillment of the Requirements
for the Degree of Doctor of Philosophy

August 2014

ABSTRACT

MODELING THAT LEADS TO

THE PREDICTION OF PHOTOCATALYTIC COATINGS CHARACTERIZATION

by Biju Bajracharya

August 2014

One of the abundant sources of energy on earth is a solar energy which is the clean and safest energy source. It is also known as universal energy, the most important source of renewable energy available today. On realizing that the light source has a crucial role in daily life, several scientists and researchers from centuries ago have studied to establish photo induced systems and utilized them. Long after the knowledge of thermal energy, photovoltaic energy, and photosynthesis in plants, two prominent scientists, Fujishima and Honda, have discovered the electrochemical photolysis of water with the Titanium dioxide electrode which was reported in "Nature by Analogy" with a natural photosynthesis in 1972 [21]. This discovery leads to the development of heterogeneous photocatalysis in various applications including air and water purification treatment and organic synthesis. Since then it has drawn the wide scientific interest of many academicians and commercial industries.

Over the past few decades, the extensive study focused on photocatalysis. Titanium dioxide photocatalysis has been promoted as a leading and emerging green technology for air and water purification systems because of its versatile nature being non-toxic environment friendly, stability to photocorrosion, low cost and potential to function under solar light better than any other artificial light source. It can be exploited for both harvesting solar energy and the destruction of organic and inorganic pollutants, even micro-organisms, in water and air by solar light irradiation.

Recently several researches have been focused on improving the operating efficiency of the photocatalytic process on both the mechanistic aspects and other operating parametric aspects including catalyst concentration load, irradiation time, relative humidity, reaction temperature and many more; however, rate limiting properties still remain elusive. Many

issues hindering its application on large scale production still exists. Several chemists and materials scientists focused mainly on the synthesis of more efficient materials and the investigation of degradation mechanism while engineers and computational scientists focused mainly on the development of appropriate models both mathematical and statistical, graphical representations to evaluate the intrinsic kinetics parameters and to build the prediction models that allow the scale up or re-design of efficient large-scale photocatalytic reactors.

The number of raw data points and raw data files collected by sensors during several experiments grows rapidly over a time. With a large number of raw data sets, a tool to handle such a large raw data set is a practical necessity both for visualization and data analysis along with the computing power. With an aim to build the prediction model of the photocatalytic characterization, scientific computing tools NumPy, SciPy, Pandas, and Matplotlib based on the python programming language are used. For graphical analysis and statistical significance, a custom tool was built using the wxPython package.

COPYRIGHT BY
BIJU BAJRACHARYA
2014

The University of Southern Mississippi

MODELING THAT LEADS TO
THE PREDICTION OF PHOTOCATALYTIC COATINGS CHARACTERIZATION

by

Biju Bajracharya

A Dissertation
Submitted to the Graduate School
of The University of Southern Mississippi
in Partial Fulfillment of the Requirements
for the Degree of Doctor of Philosophy

Approved:

Randy Buchanan

Committee Chair

Paige Buchanan

Amer Dawood

Zhaoxian Zhou

Raj B. Pandey

Dr. Maureen Ryan

Dean of the Graduate School

August 2014

ACKNOWLEDGMENTS

I wish to express my sincere gratitude and appreciation to Professor Randy Buchanan and Professor Paige Buchanan for their valuable supervision and assistance in the preparation of this manuscript. Your patience and guidance throughout this process was instrumental to its successful completion. I would like to extend my thanks to my committee members, Professor Amer Dawood, Professor Zhaoxian Zhou, and Professor Ras B. Pandey for reviewing my dissertation and providing their feedback, support, and suggestions.

I am very grateful to my colleague, Ms. LaCrissia Bridges for sharing her expertise on her field both conducting the experiments that are necessary for my work. I would also like to thank my colleagues at the University of Southern Mississippi for providing a wonderful academic experience and friendly environment during my doctoral degree program.

This is to thank all of those who have assisted me in this effort. Lastly, I would like to thank my family members, especially my wife Pramila, for their endless patience and support during my graduate studies. I am forever indebted to my advisor who is the source of all wisdom in this worldly life.

I am and remain in his awesome, brilliant shadow.

TABLE OF CONTENTS

ABSTRACT	iii
ACKNOWLEDGMENTS	iv
LIST OF TABLES	viii
LIST OF ILLUSTRATIONS	ix
LIST OF ABBREVIATIONS	xi
I Introduction	1
I.1 Introduction	1
I.2 Significance of the Dissertation	3
I.3 Problem Statement	3
I.4 Objectives of the Dissertation	4
I.5 Hypothesis of the Dissertation	5
I.6 Motivation	5
I.7 Organization of the Dissertation	5
II Review of Literature	7
II.1 Overview	7
II.2 Scientific Computing	7
II.3 Fundamentals of Photocatalysis	8
II.4 Photocatalysis	9
II.5 Effect of H ₂ O ₂	12
II.6 Effect of Gas Flow Rate	13
II.7 Effect of Relative Humidity	13
II.8 Modeling of Photocatalysis	15
II.9 Applications of TiO ₂	19
III Experimental Apparatus and Computational Tools	21
III.1 Overview	21
III.2 Photocatalytic Reactor Design	22
III.3 Photocatalytic Reactor Automation	23
III.4 Photoreactor Instrumentation Design	29
III.5 Sensors	30
III.6 Photoreactor Setup and Operational Procedure	32

III.7	Computational Tools	34
III.8	Programming	34
III.9	IDE: Spyder	35
III.10	SciPy	36
III.11	NumPy	36
III.12	Pandas	36
III.13	Matplotlib	36
III.14	wxPython	37
IV	Experimental and Computational Methods	38
IV.1	Overview	38
IV.2	Experimental Setup	38
IV.3	Calibration	38
IV.4	System Integration	39
IV.5	User Interface	40
IV.6	Preparation of Deliverables/Consumables	41
IV.7	Light Source	42
IV.8	Dispersion Preparation	42
IV.9	Coating Preparation and Activation	43
IV.10	Surface Decomposition of Chemical Analogue	45
IV.11	Preparation of Sprayer	45
IV.12	Computational Methods	46
IV.13	A Software GUI: Interactive Visual Analysis	46
IV.14	Importing Raw Data	49
IV.15	Raw Data View and Area under Curve	50
IV.16	Preprocessing of Raw Data	51
IV.17	Trimming the Raw Data	51
IV.18	Filtering Data	53
IV.19	Smoothing Data	54
IV.20	Plotting Preprocessed Data	56
IV.21	Computational Analysis Methods	59
IV.22	Analysis of CO ₂ Data	59
IV.23	Decomposing CO ₂ Curve	59
IV.24	Mathematical Model Fitting	63
IV.25	Model Selection for CO ₂ and VOC	66
V	Data Analysis	71
V.1	Overview	71
V.2	Data Analysis	71
V.3	Experiment Data Sets	73
V.4	Time Delay Adjustment	75
V.5	Base Line Detection and Adjustment	75

V.6	Estimation and Evaluation of the Model for Different Sprays Experiment	77
V.7	Constraints for the Estimates	78
V.8	CO ₂ Model for 2 Sprays	78
V.9	CO ₂ Model for 1 Spray at 50% Relative Humidity	80
V.10	CO ₂ Model for 2 Sprays at 30% Relative Humidity	81
V.11	CO ₂ Model for 2 Sprays at 70% Relative Humidity	82
V.12	VOC Modeling	83
V.13	Mathematical Model for the CO ₂ and VOC	86
V.14	Analysis of Mathematical Models	89
VI	Summary and Conclusion	93
VI.1	Conclusion	93
VI.2	Summary	93
VI.3	Contributions	94
VI.4	Limitations of the Research	95
VI.5	Future Research	95
 APPENDIX		
A	List of Sensors and its Specifications	96
 BIBLIOGRAPHY		118

LIST OF TABLES

Table

V.1	Number of Sprays and their Corresponding Mass	74
V.2	Initial Model and Coefficient of Determination for 5 Sprays at 50%RH	76
V.3	Initial Model and Coefficient of Determination for 5 Sprays at 50%RH	76
V.4	Estimation of X-scale Transformation for 2 Sprays at 50%RH	79
V.5	Estimation of X-scale Transformation for 1 Sprays at 50%RH	80
V.6	Estimation of Y-scale Transformation, Y-scale Transformation after Baseline and Time Delay Adjustment for 2 Sprays at 30%RH	81
V.7	Estimation of Y-scale Transformation, Y-scale Transformation after Baseline and Time Delay Adjustment for 2 Sprays at 70%RH	82
V.8	Time Delay Alignment Values and Baseline Values for VOC for 2 Sprays 30%RH	83
V.9	Time Delay Alignment Values and Baseline Values for VOC for 2 Sprays at 50%RH	84
V.10	Time Delay Alignment Values and Baseline Values for VOC for 2 Sprays at 70%RH	84
V.11	Estimation of Y-scale Transformation after Baseline and Time Delay Adjustment for 2 Sprays at 70% Relative Humidity	84
V.12	Estimation of Y-scale Transformation after Baseline and Time Delay Adjustment for 5 Sprays at 50% Relative Humidity	85
V.13	Estimation of Y-scale Transformation after Baseline and Time Delay Adjustment for 1 Sprays at 50% Relative Humidity	85
V.14	Ratio of CO ₂ and VOC calculated from Models	92

LIST OF ILLUSTRATIONS

Figure

II.1	Scientific Computing and Related Area [14]	8
II.2	Surface Generation of an Electron Hole Pair and Subsequent Mechanism of the Photocatalytic Process	11
II.3	Effect of Flow Rate on the Degradation of Acetone, Toluene, and P-xylene by TiO ₂ /UV Process [35]	14
II.4	Predicted vs. Experimental Degradation Rate Constant bases on (a) Equation II.9 and (b) Equation II.10 [8]	16
II.5	Experimental and Calculated Values for Removal Efficiencies of Carbofuran during the Photocatalytic Process [36]	18
II.6	Independent Variables and Levels of Factors used for Optimization [22]	18
II.7	Estimated Regression Coefficients of Percent Alachlor Removal at 60 min. [22]	19
II.8	The Actual and Predicted Plot of Percent Alachlor Removal at 60 minutes [22]	20
II.9	Applications of TiO ₂ [29]	20
III.1	General Schematic Diagram of Photocatalytic Reactor	21
III.2	Photocatalytic Reactor and the Light Source Unit (on top)	22
III.3	Front Panel GUI of Photoreactor	23
III.4	Chamber Assembly	24
III.5	Photochamber and its components	25
III.6	Photochamber Control Devices	27
III.7	Microcontroller Circuit Diagram	28
III.8	Data Acquisition System	29
III.9	USB DAQ and Sensor Array Arrangement	31
III.10	Instrumentation Sensors	31
III.11	Integrated Development Environment: Spyder	35
III.12A	Graphical User Interface(GUI)	37
IV.1	Experimental Setup	39
IV.2	A Overview of the System Architecture	40
IV.3	A LabVIEW User Interface for Data Acquisition	41
IV.4	Ocean Optics Spectra of High Pressure Mercury Lamp	43
IV.5	Novel Photoreactor Manufactured to conduct UV-conditioning of Samples while controlling Humidity, Temperature, and Light Exposure	44
IV.6	Sample Coating Q Panel	44
IV.7	Molecular Structure of Mustard Gas Chemical Agent Simulant	45
IV.8	Dis-assembled Sprayer	46
IV.9	Photocatalytic Data Analysis, Visualization and Modeling Software Platform .	47

IV.10 Experiments and Data Explorer	48
IV.11 Experimental Raw Data Import	49
IV.12 Area Plotting for 4 Hour Data	50
IV.13 Trimming Raw Data	52
IV.14 Filtering Raw/Trimmed Data	53
IV.15 Filtered Raw/Trimmed Data Import	54
IV.16 Smoothing Data	55
IV.17 CO ₂ Plotting	56
IV.18 VOC Plotting	57
IV.19 Humidity Plotting	58
IV.20 CO ₂ Curves in Photocatalytic Process	60
IV.21 CO ₂ Curves in Light with Photocatalyst	60
IV.22 CO ₂ Curves from Degradation Process	61
IV.23 CO ₂ Curves from Raw Data Sets	62
IV.24 Code Snippet to Calculate R ² Value	64
IV.25 Code Snippet of Curve Fitting for First Segment	64
IV.26 Mathematical Model of the Curves	65
IV.27 Connected Segments of the Modeled Curve	66
IV.28 Smoothly Transitioned Curve	68
IV.29 Mathematical Model of the Full Curve	69
IV.30 Raw VOC Data Curves	70
IV.31 Mathematical Model of the VOC Curve	70
 V.1 Data Modeling Process	 73
V.2 Code Snippet to Calculate the Least Square Error	74
V.3 Refined Model and Raw Experiments of 5 Sprays at 50%RH	76
V.4 Comparison of Model Raw Data of 2 Sprays at 50%RH	79
V.5 Refined Model and Raw Experiments of 2 Sprays at 50%RH	79
V.6 Comparison of Model Raw Data at 1 Sprays at 50% RH	80
V.7 Refined Model and Raw Experiments of 1 Sprays at 50%RH	81
V.8 Comparison of Model Raw Data for 2 Spray at 30 % Relative Humidity	82
V.9 Comparison of Model and Raw Data for 2 Sprays at 70% Relative Humidity	83
V.10 VOC Curves and VOC Model at 1,2 and 5 Sprays	85
V.11 CO ₂ and VOC Models at 1,2 and 3 Sprays at 50% RH; 2 Sprays at 30%,50% and 70% RH	89
V.12 Experimental CO ₂ Curves of 1, 2 and 3 Sprays at 50 %RH; Curves of 2 Sprays at 30%, 50% and 70%RH; Experimental VOC Curves of 5,2 and 1 Sprays	90
V.13 Estimation of Analytical Solution of Area Ratios of CO ₂ and VOC	91

LIST OF ABBREVIATIONS

AOP	-	Advanced Oxidation Process
CAD	-	Computer Aided Design
CC	-	Computational Chemistry
CEES	-	2-chloroethyl ethyl sulphide
CO₂	-	Carbon dioxide
DAQ	-	Data Acquisition
GA	-	General Average Approximation
GPIO	-	General Purpose Input and Output
gpm	-	Gallon per minute
GUI	-	Graphic User Interface
IDE	-	Integrated Development Environment
IO	-	Input/Output
mA	-	Milli Ampere
NI	-	National Instruments
PCB	-	Printed Circuit Board
PCD	-	Photocatalytic Degradation
PCO	-	Photocatalytic Oxidation
POSS	-	Polyhedral Oligomeric Silsesquioxane
ppm	-	Parts per million
psi	-	Pound per square inch
PWM	-	Pulse Width Modulation
RH	-	Relative Humidity
SBS	-	Sick Building Syndrome
spyder	-	Scientific PYthon Development EnviRonment
SSR	-	Solid State Relay Switch
TiO₂	-	Titanium dioxide
UV	-	Ultraviolet Light
VAC	-	AC Voltage
VDC	-	DC Voltage
VOC	-	Volatile Organic Compound

Chapter I

Introduction

I.1 Introduction

One of the greatest achievements in the history of science and engineering is the invention of a computer whose primary purpose is to solve problems in science and engineering by obtaining solutions to mathematical models that represent physical phenomena. The techniques used to obtain such solutions are part of a general area called scientific computing. The use of these techniques to elicit insight into scientific or engineering problems is called computational science [14]. Scientific computing is concerned with constructing mathematical models and quantitative analysis techniques and using computers to analyze and solve scientific problems [37]. Its objective is to gain an understanding of underlying physical phenomena, mainly through the analysis of mathematical models implemented on computers. With the aid of computer programs, these models are studied with various sets of input parameters which may require high performance computing or distributed computing platforms.

Today with a plethora of modeling software or schemes there is a challenge in finding the model that is most suitable and best fit for a specific problem. Mathematicians and numerical data analysts dealt with various numerical and analysis methods but had a hard time finding the suitable scientific problems to apply the methods. On the other hand, a scientist needs more time to delve into the numerical methods thoroughly. Computational scientist interest is to fill this gap by transferring numerical analysis to a scientific problem. This can be achieved by using appropriate analysis tools and visualization tools or developing a user application that aids both visualization and analysis.

Photocatalytic characteristics of semiconductor is one major interest of chemists, environmentalists, and material scientists. With the aid of numerical data analysis and visualization tools, scientists have success in predicting different variables in photocatalytic activities. With an immense number of variables associated with the photocatalysis, it became hard to analyze a single variable, and yet several researchers and scientists are gaining momentum in research.

In understanding the underlying behavior of each particular variable on the photocatalysis process, mathematical models are invaluable. As the number of conducted physical

experiments in the laboratory environment increases over years, it becomes more complex to analyze each experiment. These physical experiments are limited by the mechanical design of the equipment or the sensor's inability to function in certain specific conditions like high temperature, pressure, humidity, etc. In order to better understand the underlying phenomena that is limited by the physical conditions, it is very important to mathematically represent the experiment which has greater control over the experimental parameters. And while there is difficulty in creating the physically realistic scenarios, it is still very useful to analyze the experiment in each variable that can affect the experiment. To deal with the complexity of the experimental data sets, a suitable analysis and visualization tool or software will be required, which simplifies the application of numerical tools. In the meantime, it also attracts the interest of scientists to deal with the experiments.

The choice of appropriate tools that has all the necessary numerical methods and data types for the scientific data analysis is a great factor of interest for the computational scientists. However, the scripting languages, particularly Python, is gaining more popularity recently in the scientific community because of a plethora of python extension modules, its simplicity and greater number of analyzer, and computational scientists and researchers of similar interests who are dedicated to enhance the scientific libraries and modules. The high quality extension modules such as NumPy, SciPy, Matplotlib, Pandas and more efficiently written modules aid visualization, numerical analysis of huge data sets and mathematical approximation, simulation or prediction models.

The main objective of this dissertation is to explain the use of computational and customized package to visualize and analyze the experimental data, and to deduce the prediction model which will aid the understanding of underlying phenomena of the photocatalytic process.

I.2 Significance of the Dissertation

There are several raw data that are collected from photocatalytic experimental design. From these several experiments, it is necessary to extract some knowledge and direction which will help re-design, modify, and guide in the right direction of the research in the arena of photocatalysis science. Using scientific computational techniques, knowledge of underlying mechanisms that control the photocatalytic activity can be inferred. This will guide experimental research and mechanisms for controlling and regulating the experiments can be developed. One of the major tasks of this research is to build a mathematical model representing the experiments. This mathematical model leads to the prediction of conditions which are limited by several constraints like mechanical design, environmental issues, etc. Using such a model, experiments can be verified or falsified or revised before real experiments are conducted.

A mathematical model is required to be constructed that represents the photocatalytic process. To construct such a model, several experiments are required to be conducted; however, it is not possible to conduct all the experiments that include all the underlying mechanisms. To tackle and construct such a mathematical model, a computational method is required, which is a growing interest of many researchers.

I.3 Problem Statement

As scientific research progresses, it seeks to build its own devices as per the demand of the specific research interest. There has been a growing interest of many chemists, photochemists, material scientists, and environmental scientists in the process of photocatalytic characterization. Traditionally, the devices lack electronic controls and measurements. Today, use of electronics and raw sensors are common in the design of new devices. This is an interest in most of the research, which speeds up the research work.

In the course of photocatalytic characterization, the system incorporating automation of the system and raw sensors for instrumentation have been developed. Instrumentation sensors used in the device can produce several measurable outputs, which is the main interest of the fundamental task of the system. In an ideal situation, each sensor provides the response to the single physical phenomenon without any interaction with surrounding physical environments. Without the knowledge of known facts relating to the used or selected sensors in this research work, it is a major interest of analyzing the raw sensor data. These raw sensors provide continuous time series signals for the quantitative determination of the amount of multiple components of the physical phenomena.

Photoreactor is a newly designed and devised apparatus incorporating automation and instrumentation systems. It is designed to monitor the chemical activity, the photocatalytic process. The input signal to the device is the control signals to automate the reactor. The output of the system is the raw time series data, which contains the underlying photocatalytic activity undergone during the experiments conducted in the reactor. The output signal shapes are very much similar to the probability density function, which doesn't follow the periodic nature of the signals. With this nature of the output signal, it is not applicable for most of the traditional signal and data analysis. The estimation, optimization, and prediction modeling approach is based on the stochastic nature of the collected signal, which is used to extract the relevant information.

The underlying photocatalytic process produces carbon dioxide, CO_2 in the expense of a volatile organic compound. The VOC generates a peak of CO_2 and declines the signal as the VOC gets decomposed. Therefore, a fundamental approach of mathematical modeling of the underlying CO_2 and VOC components will be analyzed at multiple physical conditions, which will provide the modeling parameters. During construction of the model, several procedures need to be performed which analyze the sample, sensor response and data acquisition system and the photocatalytic process.

I.4 Objectives of the Dissertation

The main objective of this dissertation is

- to develop the Mathematical Model that leads to the prediction of of the Photocatalytic Coatings characterization.

The specific objective of this dissertation is

- to design and build a new experimental setup based on the instrumentation and automation design to obtain accurate and precise raw experimental data;
- to run a sequence of experiments with varying quantities of the specified simulants at varying humidity ranges;
- to observe assembly performance as a function of various system parameters;
- to continue to develop a model that relates system parameters to performance parameters;
- to build the customized data analysis and visualization tool using computational tools;
- to design data acquisition software using LabVIEW;

I.5 Hypothesis of the Dissertation

- when some fluids are introduced to the continuous flow stream, its measurement rises and reaches peaks and comes down unless there is another amount of fluid added or generated inside the system, which resembles our equipment setup for photocatalytic activity;
- the cooling fan with a constant speed keeps the temperature of the reactor constant;
- at same experimental conditions, the same quantity of simulant will give the same repeatable results;
- a mathematical model can be formulated and analyzed from the acquired experimental data sets.

I.6 Motivation

Scientific computing is a well studied field in modern computer science and engineering. With various computational tools available to perform the basic required operations, the choice of using existing tools in the public domain or building new tools are prudent activities that will lead to a completely new architecture and computational framework.

With increasing amounts of raw data being collected over a series of experiments, a visual and computational method can be applied to perform data mining or analysis to achieve a mathematical that can lead to prediction model.

I.7 Organization of the Dissertation

This dissertation is divided into five chapters.

Chapter I: Introduction

This chapter will be an introduction to the topic of the project covering the background, objectives, and hypothesis of the project. This chapter will give an overview to the readers to understand the significance of data analysis and a mathematical model, as well as its implementation and applications in the current scenario.

Chapter II: Literature Review

This chapter will give an overview on the literature of previous work done that is related to the mathematical model of the photocatalytic process. This chapter will help in understanding the comparative studies and analysis.

Chapter III: Experimental Apparatus and Computational Tools

This chapter will reflect the design of the desired experimental apparatus design and setup that will be used to conduct the photocatalytic activities under a controlled automated environment. This chapter will discuss the selection of scientific computing tools.

Chapter IV: Experimental and Computational Methods

This chapter will give the experimental setup and procedure to conduct the experiment. The second portion of this chapter gives the data collection methods, visual analysis, and computational analysis to formulate a prediction model.

Chapter V: Data Analysis and Evaluation of the Experimental Result

This chapter will explain the data analysis methods to validate the prediction model and evaluate the experiments. This will show information about the experiments that will be performed on the implemented systems using third party tools or comparative analysis methods. This chapter would show the details of the different experiments performed on the system.

Chapter VI: Conclusions and Future Work

This is the final chapter that will be composed of the conclusion and the future work.

Chapter II

Review of Literature

II.1 Overview

This chapter presents a comprehensive literature survey on scientific computing and application of computing tools in the scientific application of photocatalysis. Fundamentals of the photocatalytic process are presented in this chapter. The main processes involved in the photoinduced reaction are described. Catalysts used in photocatalytic oxidation reactions are presented, with special attention given to titanium dioxide. Operational parameters involved in photocatalytic degradation processes are discussed, namely catalyst loading, pollutant concentration, pH of the reaction media, presence of oxygen, temperature, and photon flow. Current mathematical methods to improve TiO_2 photocatalytic efficiency are discussed.

II.2 Scientific Computing

Scientific computing is the field of study "concerned with constructing mathematical models and quantitative analysis techniques and using computers to analyze and solve problems in science and engineering domains. Its approach is to gain understanding, mainly through the analysis of mathematical models implemented on computers" [37].

Computing often builds models of real world scenarios such as weather prediction, material science, structural biology, superconductivity, vehicle dynamics, air flow around planes, explosives, etc. With the aid of computer software, models are studied with various sets of input parameters. However, algorithms and mathematical methods used in these models may vary from one domain to another domain. These models may require massive amounts of calculations which are often executed on supercomputers or distributed with computing platforms.

Scientific computing draws on mathematics and computer science to develop the best ways to use computer systems to solve problems from science and engineering [14]. This is depicted schematically in Figure II.1.

In general, scientific computing is solving problems efficiently by harnessing the power of modern computers and exploiting the mathematical relations and theories. Being of a

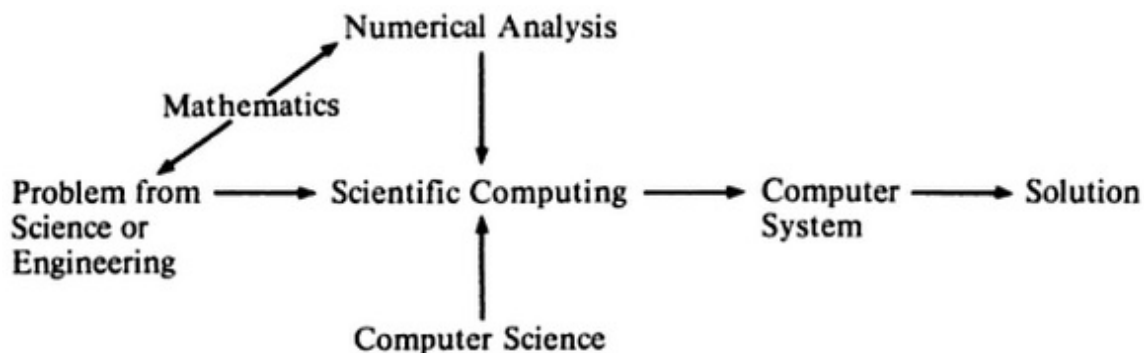


Figure II.1: Scientific Computing and Related Area [14]

multidisciplinary nature, it is used to solve the problems of various applications in science and engineering to give rise to mathematical models. From the raw data acquired from those applications, data analysis is done by implementing the modern numerical methods and high performance computing tools to produce efficient mathematical models. One of the topics of interest is the photocatalytic process. Models of a photocatalysis have evolved over the years and have been refined and integrated into the study of photocatalytic coatings characterization.

II.3 Fundamentals of Photocatalysis

Photocatalytic oxidation is a very rapidly expanding technology in indoor air treatment and waste-water treatment because of its superior characteristics over other costly conventional methods like activated carbon adsorption, chemical scrubbers, biofiltration, or thermal catalysis. Because of its inert nature, photostability, harmless bi-products, and cost effective solution to degradation of pollution, many researcher have widely investigated this phenomenon. Several research analyses has been conducted for improving the efficiency of photo-degradation processes considering physical or chemical factors.

There are several types of pollutants that present in indoor air such as nitrogen oxide (NO_x), carbon dioxide, carbon monoxide, volatile organic compound (VOC), dust particles, etc. These pollutants come from different sources such as domestic activities like cooking, construction materials, office equipment, wall paints, and other household products. One of the well known indoor pollutants is VOC. VOCs are widely used in (and produced by) both industrial and domestic activities. This extensive use results in their occurrence in aquatic, soil, and atmospheric environments. Many VOCs are toxic, and some are considered to be carcinogenic, mutagenic, or teratogenic [2]. These VOCs have a close relation with the

sick building syndrome (SBS), which is one of many terms used by occupants to describe symptoms of reduced comfort or health [34].

There are various conventional methods to remove these VOCs. Advanced oxidation processes (AOP) such as thermal oxidation destruction and photocatalytic oxidation (PCO) are promising technologies for air purification because the pollutants can be oxidised into H_2O and CO_2 . However, thermally catalytic oxidation requires high temperatures of 200-1200 °C for efficient operation, and are therefore expensive [34].

A lot of investigations conducted in photocatalytic oxidation of gaseous VOCs made over the past few years have made several photocatalyst systems. Several investigations are made to analyze the important factors that influence the catalytic activity. However, there are limited studies on the photodegradation of VOC pollutants at typical indoor levels [34]. Several factors, such as ambient operating conditions, photocatalyst design, and radiation intensity are considered to determine the rate of degradation.

II.4 Photocatalysis

Photocatalysis is the reaction induced by the action of light in the presence of a catalyst where the catalyst facilitates the chemical reactions without being consumed or transformed. More specifically, IUPAC defines photocatalysis as "change in the rate of a chemical reaction or its initiation under the action of ultraviolet, visible or infrared radiation in the presence of a substance? the photocatalyst? that absorbs light and is involved in the chemical transformation of the reaction partners" [28].

With the discovery of the electrochemical photolysis of water with Titanium dioxide (TiO_2) electrodes by Fujishima and Honda in 1972 [21], it has taken much attention from several scientists and researchers around the world. Since then, TiO_2 , also known as titania mediated photocatalysis, has been reported as a much promising route to destroy toxic and hazardous organic substances both in the air and water, which yields end product of water (H_2O), carbon dioxide (CO_2), and inorganic ions upon complete oxidation of the pollutants. However, there are several other semiconductor photocatalysts, but TiO_2 is more superior because of its high activity, large stability to light illumination, low price, and nontoxicity.

Heterogeneous photocatalysis is a catalysis that involves the acceleration of photoreaction in the presence of a semiconductor photocatalyst, which affects partial or total mineralization of a gas phase or liquid phase contaminate to benign substances [13]. As for classical heterogeneous catalysis, the overall process can be decomposed into five independent steps [17]:

- Diffusion of the reactants from the bulk phase to the surface of the catalyst;

- Adsorption of at least one of the reactants;
- Reaction in the adsorbed phase;
- Desorption of the products;
- Removal of the products from the interface region.

In conventional catalysis, the mode of catalyst is activated with thermal activation which is being replaced by photonic activation. This mode of activation is concerned in step three which includes several photoelectronic processes: absorption of photons by the solid catalyst; creation of electron/hole pairs which dissociate into photoelectrons and positive photo-holes; electron transfer reactions [17].

II.4.1 Basic Mechanisms of TiO₂ Photocatalysis

Photocatalytic activity has been reported to occur in the presence of oxygen, water, and light intensity. In addition to the crystalline forms of TiO₂, the photocatalytic efficiency of TiO₂ also varies widely with respect to illumination conditions, species, concentration, temperature, and humidity [15].

The basic chemical reaction mechanism is depicted in Figure II.2, which illustrates the chemical actions at the catalyst surface by an organic pollutant. When the catalyst is exposed to photons whose energy is equal to or greater than band gap energy (E_{bg}) (~3.2 eV or ~380nm), it absorbs the photons. This stimulates the electron transfer from the valence band (VB) causing them to move to the empty conduction band (CB) creating positive holes in the VB. The possible recombination of a highly reactive photoproduced electron hole (e⁻/h⁺) pair can produce heat and can reduce or can oxidize the species at the catalyst surface which could be either promoting or limiting factors for photocatalytic efficiency.

Generated electron hole (e⁻/h⁺) pairs, when reacted with the adsorbed water molecules, creates a highly reactive hydroxyl radical (·OH), which initiates the oxidation reactions. These powerful oxidative redox reactions will scavenge the surface of the material to degrade any organic material that may be present on the film. Under optimal reaction conditions, organic pollutants can be completely oxidized to form environmentally friendly products CO₂, H₂O, etc. The following equations describe a reaction's pathways using titanium dioxide (TiO₂) as the catalyst.



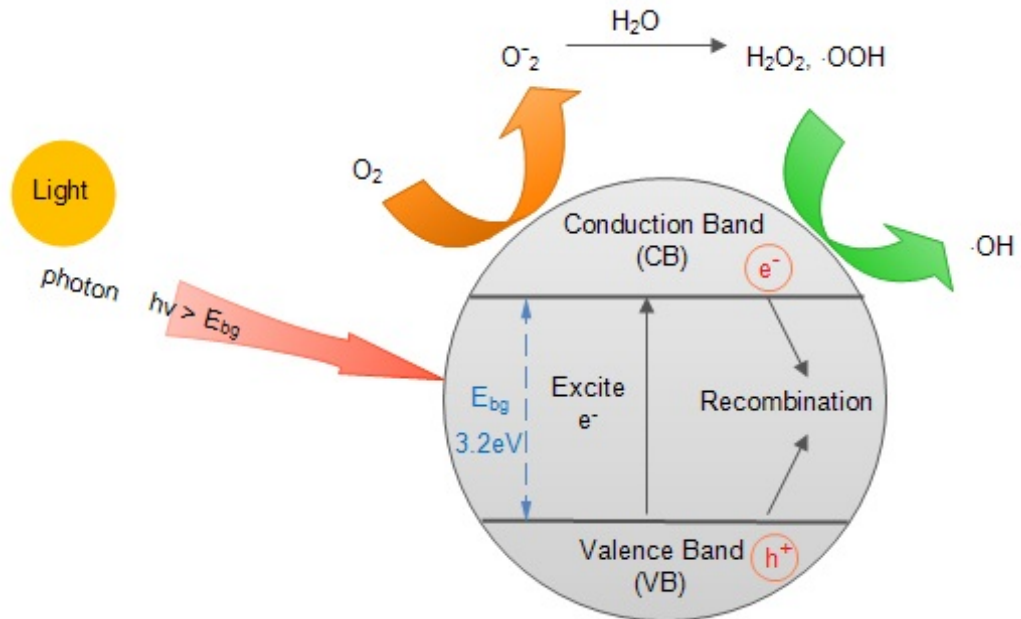
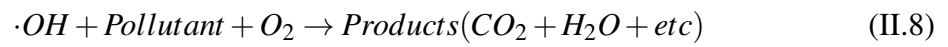
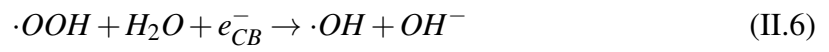
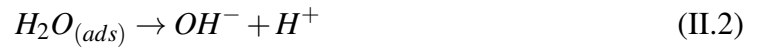


Figure II.2: Surface Generation of an Electron Hole Pair and Subsequent Mechanism of the Photocatalytic Process

Although several examinations yielded insight into the mechanism of the reaction of TiO_2 with organic substrates in solution, not as much information is available for this chemistry in the solid state. This project has been designed to examine the degradation of common organic compounds to study the rates of decontamination in a photocatalytic coating. Novel $\text{TiO}_2\text{--SiO}_2$ thin films were used to produce superhydrophilic surfaces, which promotes a self-cleaning attribute that facilitates environmental cleaning applications. Since dispersion stability has been correlated to several coating characteristics (i.e., surface coverage, adhesion, and uniform topology), the initial focus was on the development of a stable dispersion. A polyhedral oligomeric silsesquioxane derivative, trisilanol isobutyl, was chosen for the sterics provided to promote repulsion throughout the dispersion.

Many researchers have synthesized various photocatalysts to decompose different VOCs. The degradation of VOCs and therewith the performance of the photocatalytic reaction is governed by physicochemical as well as product-related parameters. There are several external influencing factors of the degradation process. They are as follows:

- i. Hydrogen Peroxide (H_2O_2)
- ii. UV-A Irradiance
- iii. concentration of water expressed by Relative Humidity
- iv. Light Intensity
- v. Wavelength
- vi. Reaction Temperature
- vii. pH
- viii. Contact Time and Surface Area

II.5 Effect of H_2O_2

Effect of hydrogen peroxide on photocatalytic degradation has been studied and found to have two main functions affecting it. Due to photo-generated conduction band electrons, promoting the charge separation, it forms hydroxyl radical ($\text{OH}\cdot$). The addition of H_2O_2 increases the concentration of the $\text{OH}\cdot$ radical since it inhibits the electron-hole recombination. From the experimental evaluation of the H_2O_2 on toluene/p-xylene degradation, is found that it follows a flow rate of 1L/min, initial concentration of 0.1 mol/m^3 , relative humidity of 35% and photocatalyst of pure TiO_2 [35].

Experiments were conducted to evaluate the effect of H_2O_2 on the toluene/p-xylene degradation. It was found that it follows flow rate of 1L/min, initial concentration of 0.1 mol/m^3 , relative humidity of 35%, and photocatalyst of pure TiO_2 . As the reactants and/or byproducts accumulated on the catalyst, and there was no new super-oxidation supplied, the catalyst deactivated and the degradation rate increased slowly after 2 hr. Hydroxyl radical were produced due to the presence of hydrogen peroxide. This decreased the recombination of electron hole pairs and consequently the final acetone degradation rate was up to 91.8% after 8 hr. Consumption of hydroxyl radicals likely played an important role in deactivation of the catalysts, and appropriate volume of hydrogen peroxide could enhance the degradation rate, while too much could decrease the degradation rate [35].

II.6 Effect of Gas Flow Rate

Gas flow rate is the important factor in photocatalytic activity. With higher gas flow rate, pollutant gets less residence time on the photocatalyst surface. At lower gas flow rate, pollutant gets higher residence time on the photocatalyst surface. With more time to interact with the photocatalyst, there will be more degradation activity. There has been several studies conducted over the effect of gas flow. Wenjung et. al studied on gas flow rate on ATP degradation and attempted to find the optimum gas flow rate. The effect of gas flow rate on ATP degradation at an initial concentration of 0.1 mol/m^3 and relative humidity of 35%, is as shown in Figure II.3. When the flow rate was increased from 3-9 L/min, degradation of toluene and acetone decreased. With a flow rate $> 3 \text{ L/min}$ the reactants have shorter residence time on the photocatalyst surface and consequently do not bind to the active sites. From his finding, the degradation rate of ATP at 1 L/min was the lowest. For p-xylene, the degradation rate was the highest when the flow rate was 7L/min. The highest degradation rates for acetone, toluene, and p-xylene were 77.7, 61.9 and 55% respectively [35]. The gas flow rate remarkable influences on the degradation rate.

II.7 Effect of Relative Humidity

The influence of the relative humidity depends to a large extent on the characteristics of contaminants. It has been observed that the surface OH groups and/or physisorbed H_2O , as well as the anion radicals, can play a significant role as key active species in the PO reactions of various VOCs. In the absence of water vapor, the photocatalytic degradation of some chemical compounds (eg. toluene, formaldehyde) is seriously retarded and the total mineralization to CO_2 does not occur. However, excessive water vapor on the catalyst surface will lead to the decrease of reaction rate because water molecules can occupy the

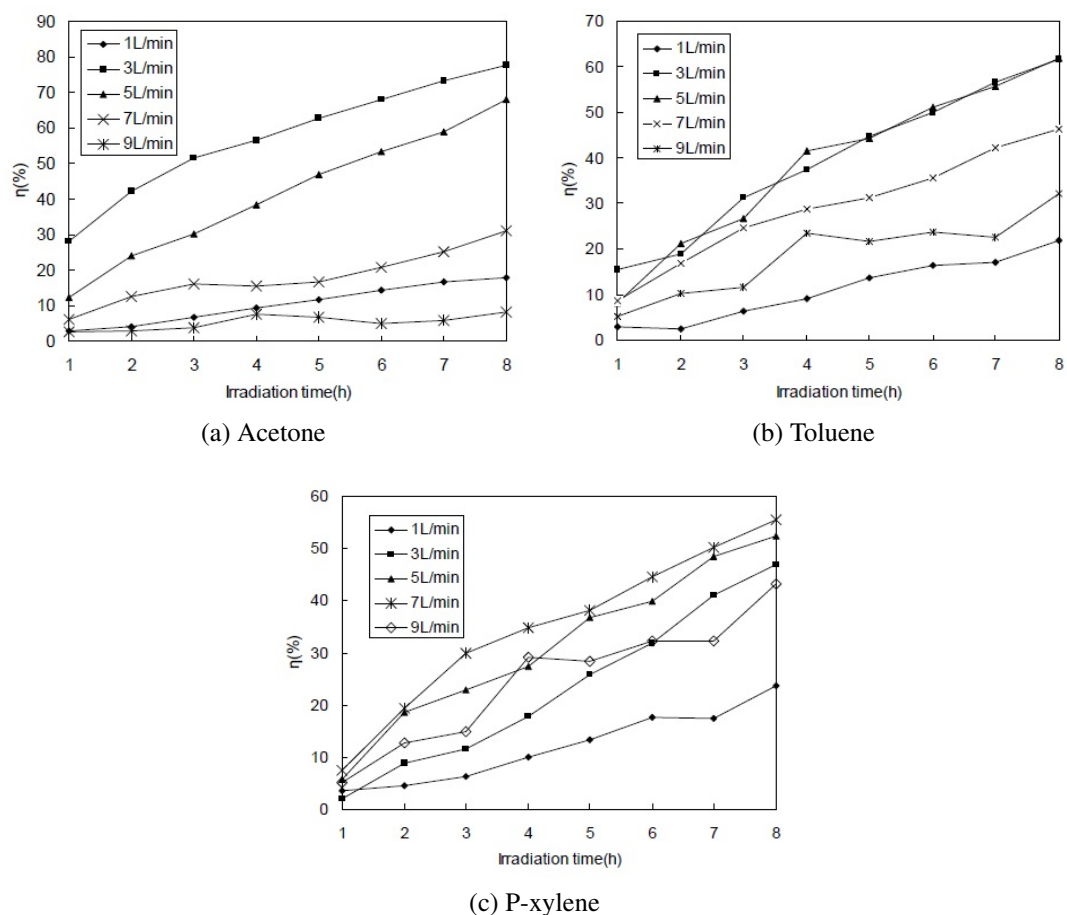


Figure II.3: Effect of Flow Rate on the Degradation of Acetone, Toluene, and P-xylene by TiO_2/UV Process [35]

active sites of the reactants on the surface and the hydrophilic effect at the surface prevails over the oxidizing effect. The hydrophilic effect at the surface prevails over the oxidizing effect when high values of relative humidity are applied.

TiO_2 surface carries weakly or strongly bound molecular water, as well as hydroxyl groups created by the dissociative chemisorption of water.

Obee and Brown investigated the effect of humidity on photoxidation rate of formaldehyde, toluene, and 1,3-butadiene on titania. The data showed that competitive adsorption between water trace contaminants had significant effect on the oxidation rate.

However, Joe et al. found that the humidity had little effect on photocatalytic oxidation of benzene, ethyl benzene, and o-, m-, p-xylenes, trichloroethylene and perchloroethylene the PCO destruction efficiencies were close to 100% for four different RH range from 18 to 78%. As and Lee compared the effect of humidity on photocatalysis oxidation of BTEX on TiO_2

and TiO₂/AC systems and the results indicated that TiO₂/Ac exhibited higher resistance to humidity effect. This negative effect of water vapor on TOL removal was in agreement with results obtained by other authors investigating photocatalytic TOL degradation by TiO₂/UV.

The practical evaluation by installation of the TiO₂/ac filter in an air cleaner was also conducted. The use of TiO₂/AC not only increased the target pollutant removal efficiency but also reduced the amount of intermediate exiting the system. The study showed that the enhancement effect of the TiO₂/Ac shown in the laboratory scale using the photoreactor was also achieved by installing it into an air cleaner available in the commercial market.

Except the factors, the volatile organic compound structure is also an important feature. O'Malley and Hodneett found that a primary factor in determining the reactivity of volatile organic compounds in oxidation reaction was the strength of the weakest C-H bond in the structure, which implicated that destruction of volatile organic compounds over oxidation catalysts proceeded by initial rupture of the weakest C-H bond in the compound, followed by further steps that may involve free radical chemistry. The research showed that the reactivity of VOCs with different functional groups for total oxidation varied as alcohols > aromatics > ketones > carboxylic acids > alkanes.

II.8 Modeling of Photocatalysis

Mathematical models are used in several occasions to analyze the photocatalytic degradations. These mathematical models are developed and verified by correlating them to the experimental data along with theoretical suppositions and hypothesis. With lots of parameters governing the complex photocatalytic process, a mathematical model is used to simplify the process, which is ultimately used to predict and optimize the parameters needed to control and enhance the photocatalytic process that allow the scale up or re-design of efficient large-scale photocatalytic reactors. Many researchers have used several varieties of mathematical models. The following section describes the mathematical models that are used in photocatalytic process.

II.8.1 Model Development

In a research study conducted by Lalman et al. [8], the photocatalytic degradation of phenolic compounds in the presence of titanium dioxide (TiO₂) nano-particles and UV light had investigated. A regression model was used to develop to relate the apparent degradation constant to the various factors. A full factorial design was used to examine the effect of particle size, temperature, and reactant type on the apparent degradation rate constant. The individual effect of TiO₂ particle size (5, 10 and 32 nm), temperature (23, 30 and 37°C),

and reactant type (phenol, o-cresol and m-cresol) on the apparent degradation rate constant was determined.

A second-order quadratic polynomial order selected by the Minitab (statistical software) was used to relate the coded factors and the response. After regression analysis using coded units, the regression model was built given by equation II.9 and II.10, which gives 97.33% of the variation in the degradation rate constant values. The predicted R^2 of 0.9362 is in reasonable agreement with the adjusted R^2 of 0.9615. The model was found to be predictive, which showed the model was reliable within the range of factors under consideration.

$$k = 0.10985 + 0.00833x_1 - 0.00266x_2 + 0.00189x_1^2 - 0.003994x_2^2 - 0.000158x_1x_2 + 0.001672z - 0.000200zx_1 + 0.000392zx_2 \quad (\text{II.9})$$

$$k' = 0.01111 + 0.00833x_1 - 0.00266x_2 - 0.00399x_2^2 + 0.01672z \quad (\text{II.10})$$

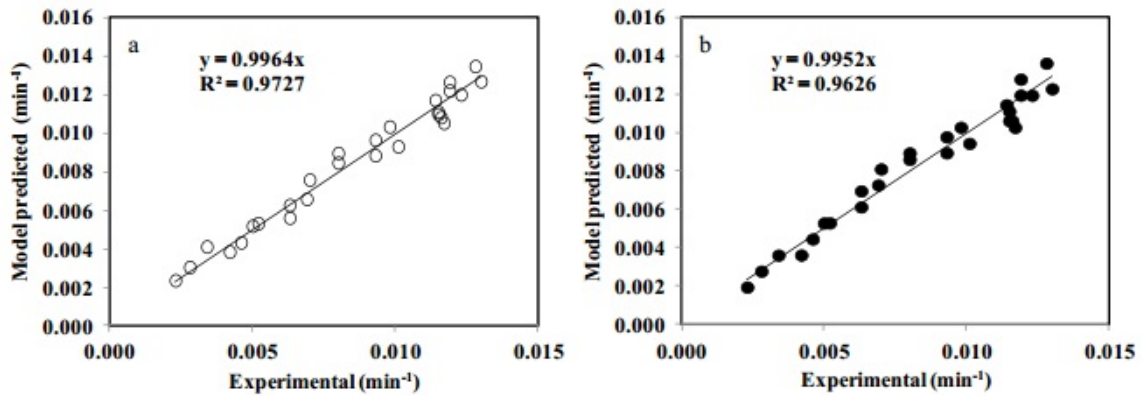


Figure II.4: Predicted vs. Experimental Degradation Rate Constant bases on (a) Equation II.9 and (b) Equation II.10 [8]

This model equation II.9 contains insignificant and significant terms. The modified model equation II.10 was developed by neglecting the insignificant terms in the quadratic equation (Equation II.9). The predicted values obtained from the two equations (Equations II.9 and II.10) are shown in Figure II.4. The comparison indicated no significant difference between the predicted response values for the two models (Figure II.4).

Using the D-optimal criterion, the maximum degradation rate were calculated. The D-optimal criterion selects design points from a list of candidate points, such that the variances of the model regression coefficients are minimized. By using the model, for largest

photocatalytic activity of the three compounds, the optimum TiO₂ particle size was obtained. The maximum degradation rate constant were obtained. These obtained optimum values of the factors can be adopted for further laboratory experiments and pilot-scale organic pollutants removal processes.

In the research study by Yang et al. [36], the photocatalytic degradation kinetics of carbofuran was optimized using a central composite design (CCD) based on response surface methodology (RSM). Three variables, TiO₂ concentration, initial pH value and the concentration of carbofuran, were selected to determine the dependence of degradation efficiencies on independent variables. Analysis of experimental data by using Design-Expert Software, these three variable were investigated in the multivariable experimental design where these variables were converted into dimensionless (x_1, x_2, x_3) with the coded values of $-\alpha, -1, 0, +1, +\alpha$.

From experimental results, a semiempirical expression in equation II.11, which consisted of 10 statistically significant coefficient was obtained and expressed as where Y is the response variable of the degradation efficiency of carbofuran. The x_1, x_2 and x_3 represent three experimental factors, respectively. The comparison of experimental values (Y_{exp}) against the responses predicted by the model (y_{cal}) for the degradation efficiencies of carbofuran with a good correlation ($R^2=0.98$) indicate that this model explains the experimental range very well. From Figure II.5, it can be concluded that model obtained is adequate to describe the relationship between the degradation efficiency and these three above mentioned parameters.

$$Y = 83.70 - 0.17x_1 - 72.4x_2 + 5.26x_3 - 2.29x_1x_2 + 2.66x_1x_3 + 0.41x_2x_3 - 1.59x_1^2 - 0.99x_2^2 - 1.06x_3^2 \quad (II.11)$$

In the research conducted by Wantala et al. [22], the extended photocatlytic conditions were studied as functions of catalyst loading, number of black light, and initial pH of solution using Response surface Methods (RSM) based on Box-Behnken Design (BBD). The effects of these three operating variables (X_1, X_2 and X_3) on the degradation efficiency of alachlor were examined. The independent variables and factor levels were listed in Figure II.6.

A quadratic-second degree polynomial regression was used to approximate a mathematical relationship of all three variables and could be expressed by the equation II.12.

$$y = \beta_0 + \sum_{i=1}^4 \beta_i X_i + \sum_{i=1}^4 \beta_i^2 X_i^2 + \sum_{i=1}^3 \sum_{j \neq i}^4 \beta_{ij} X_i X_j \pm \epsilon \quad (II.12)$$

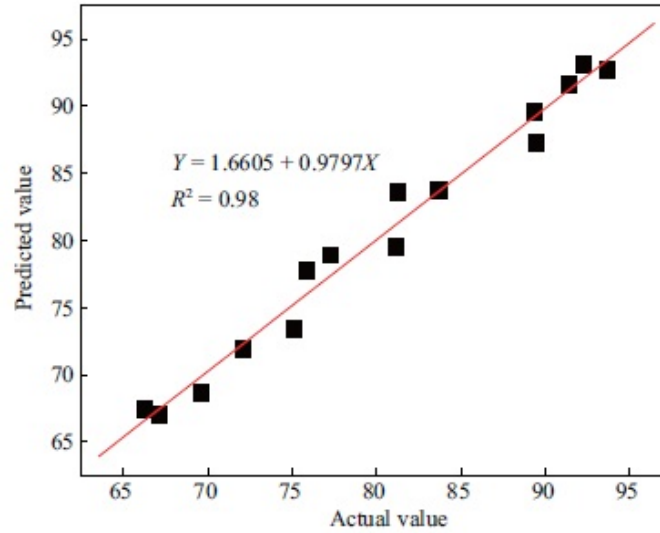


Figure II.5: Experimental and Calculated Values for Removal Efficiencies of Carbofuran during the Photocatalytic Process [36]

Variable	Level		
	Low (-)	Middle (0)	High (+)
1. Catalyst loading (g/L); X_1	1	2	3
2. Number of black lights; X_2	1	2	3
3. pH of solutions; X_3	4	6	8

Figure II.6: Independent Variables and Levels of Factors used for Optimization [22]

where Y is the response (% removal of alachlor), $\beta_0, \beta_i, \beta_i^2$ and β_{ij} are the constant coefficients, X is the coded independent variable, and ε is the experimental error.

RSM was utilized to verify the main and interactive effects of operating variables. The optimization design process based on BBD involves mainly four major steps explained by

- performing statistically designed experiments according to the experimental plan,
- proposing the mathematical model based on the experimental results and elaborate the result of analysis of variance (ANOVA),
- checking the adequacy of the model through diagnostic plots,

- predicting the response and confirm the model.

An approximate function of alachlor removal efficiency based on the experimental results was evaluated and given as Equation II.13 as given coefficient data in Figure II.7.

Term	Coef.	P-Value
Constant	70.05	0.000
Catalyst loading	18.64	0.000
No. of black lights	1.59	0.266
pH	0.40	0.774
Catalyst*Catalyst	-7.50	0.005
No. of black lights*No. of black lights	-1.95	0.679
pH*pH	-0.83	0.901
Catalyst*No. of black lights	-1.53	0.445
Catalyst*pH	2.07	0.305
No. of black lights*pH	-1.18	0.556

Figure II.7: Estimated Regression Coefficients of Percent Alachlor Removal at 60 min. [22]

$$Y = 70.046 + 18.636X_1 + 1.591X_2 + 0.404X_3 - 1.529X_1X_2 + 2.066X_1X_3 - 1.177X_2X_3 - 7.50X_1^2 - 1.947X_2^2 - 0.830X_3^2 \quad (\text{II.13})$$

where y is predicted alachlor degradation (%removal), X_1 , X_2 and X_3 are corresponding coded variables of catalyst loading, number of black, light, and pH of solution respectively. Figure II.8 shows relationship between predicted values calculated by equation II.10 evaluated from model and experimental values.

II.9 Applications of TiO₂

TiO₂ photocatalysis is widely used in a variety of applications and products in the environmental and energy fields, including self-cleaning surfaces, air and water purification systems, sterilization, hydrogen evolution, and photoelectrochemical conversion as shown in Figure II.9 [29].

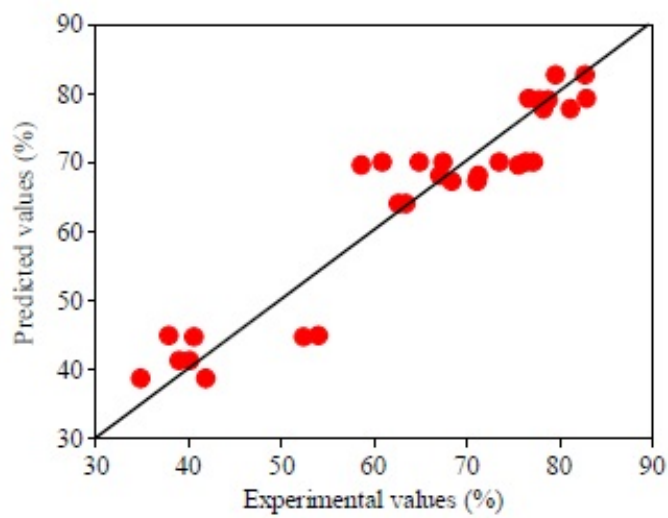


Figure II.8: The Actual and Predicted Plot of Percent Alachlor Removal at 60 minutes [22]

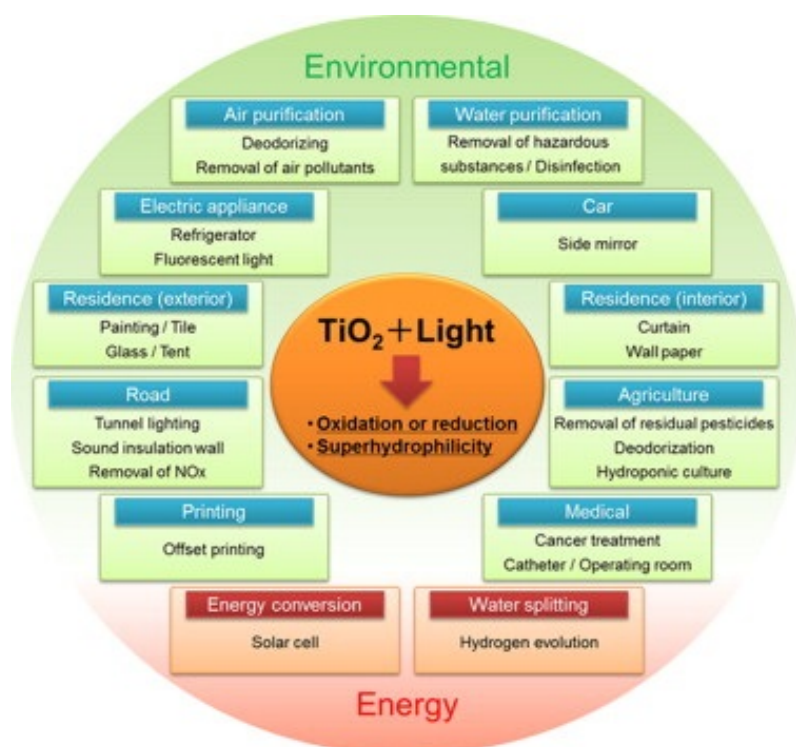


Figure II.9: Applications of TiO_2 [29]

Chapter III

Experimental Apparatus and Computational Tools

III.1 Overview

The main objective of this research was to design a photoreactor from an existing reactor to incorporate a fully integrated instrumentation system and to automate a reactor that enables higher precision, accuracy, and continuous measurement environment with only few human intervention. This chapter gives an overview of the reactor design, control devices, instrumentation devices, and operating procedures of the reactor. The second portion of this chapter describes the computational tools that are used to perform the data analysis and build the prediction model and selection of integrated development environment (IDE) platform.

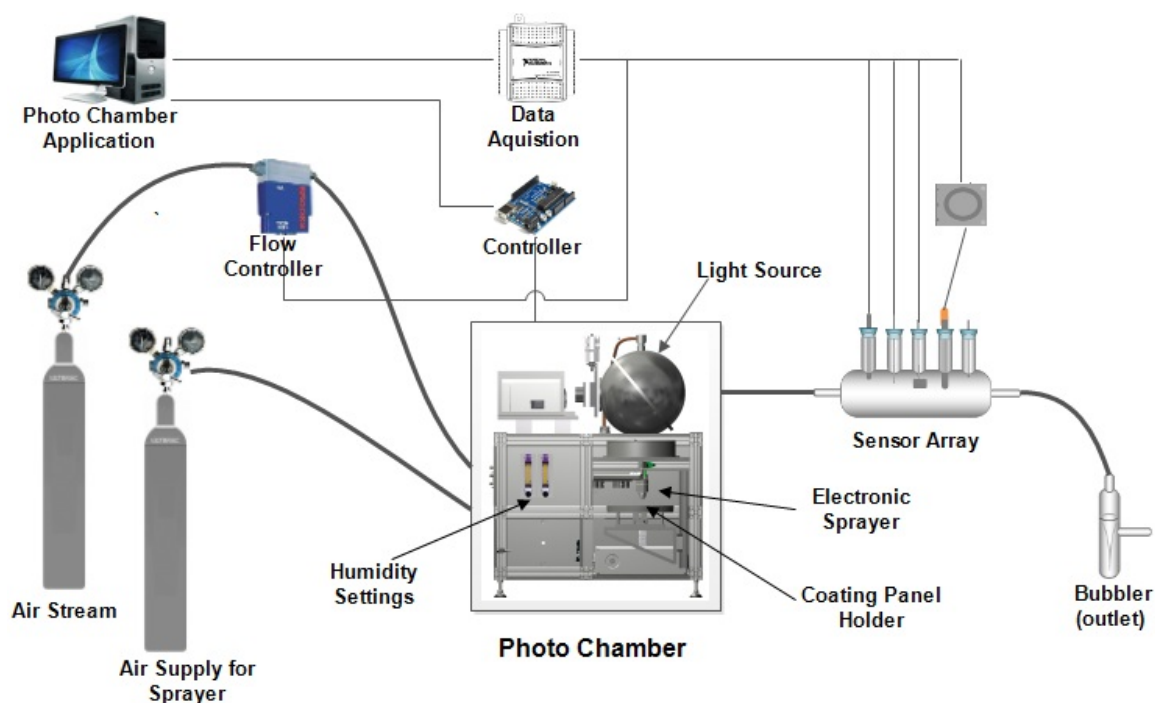


Figure III.1: General Schematic Diagram of Photocatalytic Reactor

III.2 Photocatalytic Reactor Design

A new photoreactor is designed to incorporate renovations to an existing photoreactor to provide a laboratory environment and automate the system. The photoreactor is fabricated with all the necessary circuitry, automation, and instrumentation components that are required to conduct a photocatalytic activity. A snapshot of three dimensional computer aided design (CAD) model designed and produced in Autodesk Inventor is shown in Figure III.2. The photoreactor consists of two main distinct compartments. First compartment consists of circuitry and controllers. Second compartment consists of a form of two sandwiched anodized steel chambers to increase durability and corrosion resistance where feeding of an organic compound (simulant) sprays over the sample panel coatings(catalyst) . The reactor enclosure is built with the framework of aluminum bars for structural support and the plastic panels painted to keep the light within the chamber and to make safe from outside environment. The light source sits on top of the reactor as shown in Figure III.2 from where light will be introduced inside the chamber.



Figure III.2: Photocatalytic Reactor and the Light Source Unit (on top)

III.3 Photocatalytic Reactor Automation

The second compartment of the reactor consists of a form of two sandwiched chambers as shown in CAD diagram III.4 (a). The top chamber includes a one piece anodized steel and a quartz top lid, which incorporates gas inlet and outlet connections as well as o-ring sealing of the quartz window. The lid is attached with screws as shown in Figure III.4(b). The quartz window provides exposure with the light source that sits on top of the reactor. The bottom chamber Figure III.4(c) acts like a tray designed to allow sample panel placement and sprays over the sample test panel. The system is automated by attaching a vertical actuator to move the bottom chamber down to insert the sample test panel. After insertion of the sample test panels in place, from the computer user interface Figure III.3, an operator starts the process by selecting a number of sprays after which the bottom chamber lifts up and sandwiched with the top chamber.

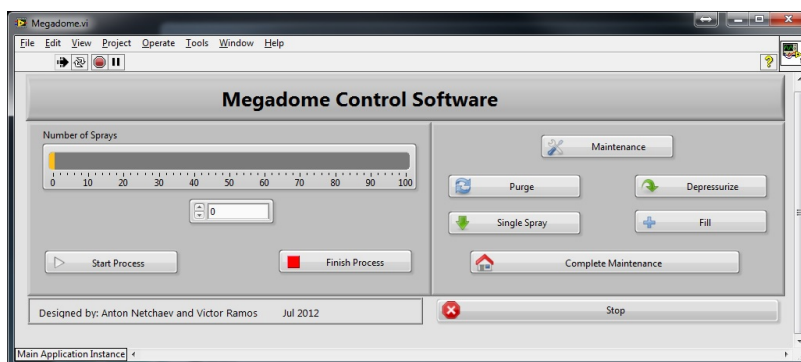
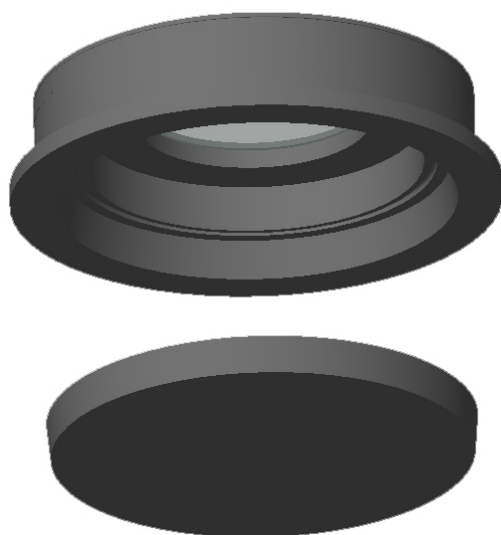
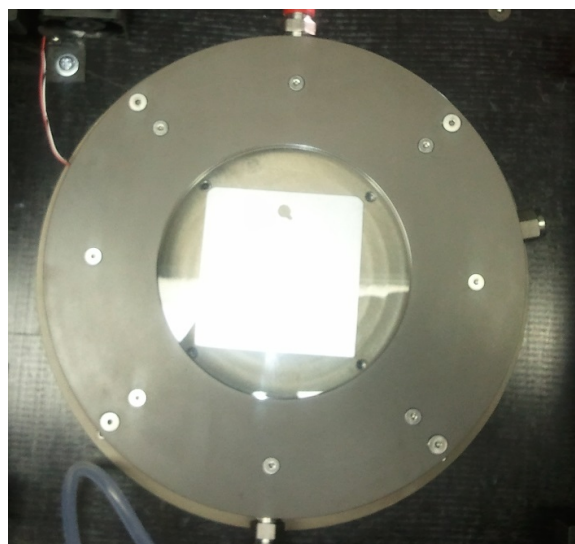


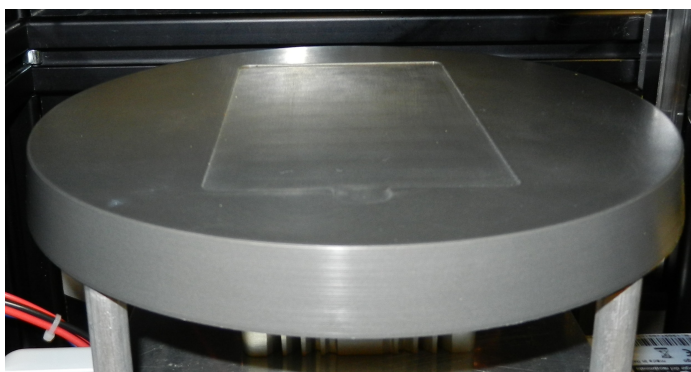
Figure III.3: Front Panel GUI of Photoreactor



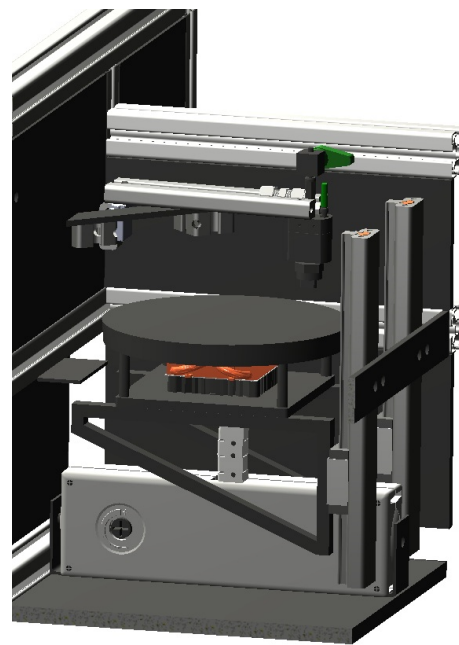
(a) Sandwiched Chamber CAD Model



(b) Top Chamber with Quartz Window



(c) Bottom Chamber (Sample Test Tray)



(d) Chamber with Actuator

Figure III.4: Chamber Assembly

The automation of the photoreactor is controlled by a Microcontroller (Figure III.6 (e)). This is the integration of several hardware components: ultrasonic sprayer, servo motor, vertical actuator, solid state relay, solenoid valve, h-bridge circuit, voltage regulator, and cooling fan. The purpose of the Microcontroller is to control the vertical lift actuator, sprayer, sprayer arm, solid state relays, cooling fan, and solenoid valve. It has current feedback from the servo motor and the ridge switch from the access door of the reactor that halt the process if the access door was accidentally opened or actuator become stuck and immovable by incorporating the hardware interrupt. The Wiring and circuit diagram of the Microcontroller is shown in the Figure III.7. The Microcontroller communicates with the reactor software, a graphical user interface written in LabVIEW (Figure III.3) via serial communication, which sends it to devices through general purpose input/output (GPIO) interface. Every time the reactor is turned on or recovered from power failure, startup function is executed to start/restart the reactor in initial condition.

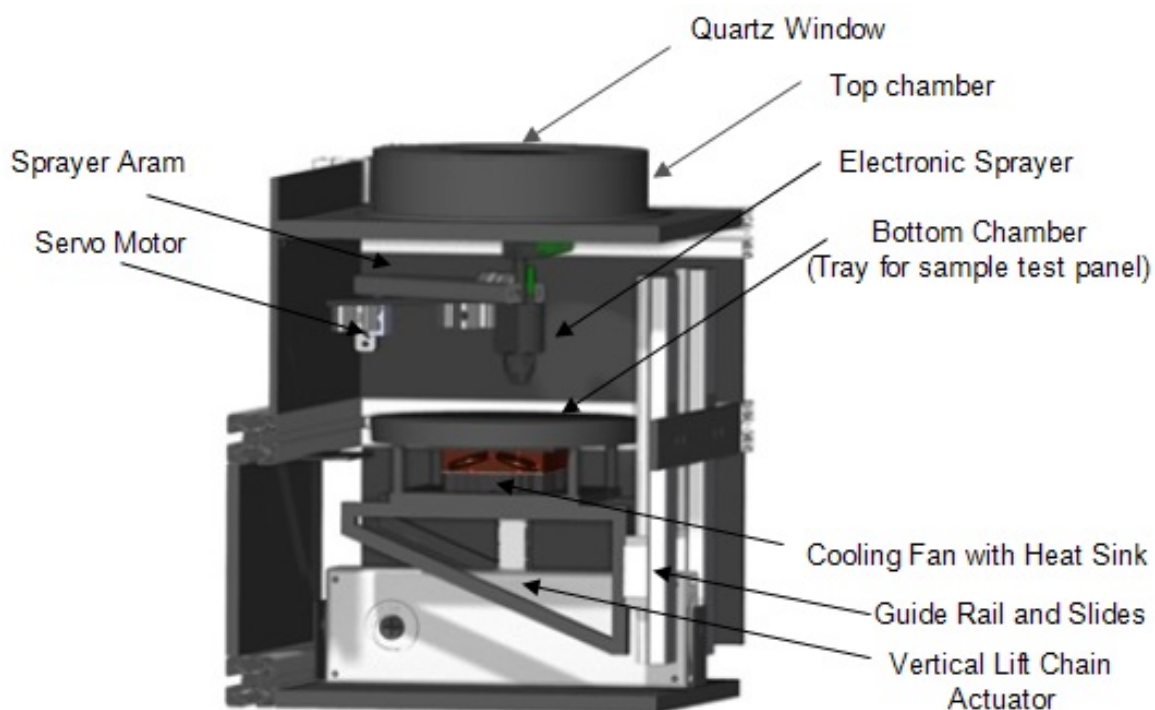


Figure III.5: Photochamber and its components

For the automation of the reactor several hardware components are used, shown in Figure III.6. They are solenoid valve, server motor, solid state relay switch, vertical chain actuator, Microcontroller, cooling fan, flow controller, h-bridge, sprayer, and swagelok value.

For accurate dispensing of the simulant over a target, the automatic electronic sprayer (Figure III.6 (i)) is used. It is powered with 24V DC and controlled by a pulse width modulation (PWM) of power signal which is controlled by a Microcontroller. It has a replaceable nozzle tip which can be selected according to type of spray pattern required. The sprayer is used to spray, de-pressurize, and purge the simulant. A single spray cycle is two 6 millisecond (ms) pulses, which are adjusted by varying pulse width of the power signal to the sprayer. The de-pressurization is done to relieve line pressure by opening a nozzle for 10 seconds before a filling process of the simulant. The purging is done by spraying 200 times (100 cycles) with the solenoid valve open to remove all the simulants present in the sprayer. The nozzle is capable of delivering 0.47 gpm (1.8 l/min) at 100 psi (7 bar). With a maximum spray rate of 10,000 cycles per minute (once every 6 ms) it is possible to achieve spray volumes $\approx 10\mu\text{L}$ per cycle.

The sprayer nozzle is attached to a spray arm. The other end of sprayer arm is attached to a servo motor which is at the corner of the chamber, as shown in Figure III.5. The servo motor is used to move the sprayer arm which has 90° of angular movement. The angular movement is controlled by a Microcontroller by sending signal pulses to the servo. It has 12 bit digital resolution at 347.2 oz-in of torque.

The vertical actuator moves up and down, and the sprayer arm moves right or left in angular motion. To accomplish this, polarity of the power signal needs to be reversed. An h-bridge (Figure III.6 (c)) is used to reverse the polarity. It is operated by 24v DC and can support up to 3A of continuous current. By utilizing the current feedback from the actuator motor to the Microcontroller, the actuator is turned off at a predetermined current value. The PWM signal source to the bridge is used to vary the speed of motor movement as well.

The bottom chamber (Figure III.4), a sample tray is raised by a 24VDC chain vertical lift actuator which provides a force of 300 Newtons, or about 67 lbs. The vertical lift actuator is moved along the steel guide rails and slides (Figure III.6). The bottom chamber is lifted up by this chain actuator and sandwiched with the top chamber forming a sealed chamber. After completion of the experiment, the actuator lowers down so that a new sample can be loaded on the bottom chamber.

A sample tray is heated during the progress of the experiment by the Xenon light source, which sits on top of a quartz glass window. A cooling fan with heat sink is provided by attaching it to the bottom of the sample tray to keep the temperature of the chamber constant. The cooling fan is operated by the Microcontroller via PWM signal to a solid-state relay

(SSR) switch. The fan is turned off during loading of the sample test and spraying by solid-state relay switch.

An in-line solenoid valve is used to supply the pressurized air to the sprayer. It is activated by the Microcontroller to control the flow of air which also isolates the sprayer from the line pressure of the air cylinder. Line pressure needs to be cut off during refilling of simulant into the sprayer. The quarter inch ported 3-way valve with pressure range of 1-125psia serves as the control value to limit or stop the pressurized air stream to the sprayer.



Figure III.6: Photochamber Control Devices

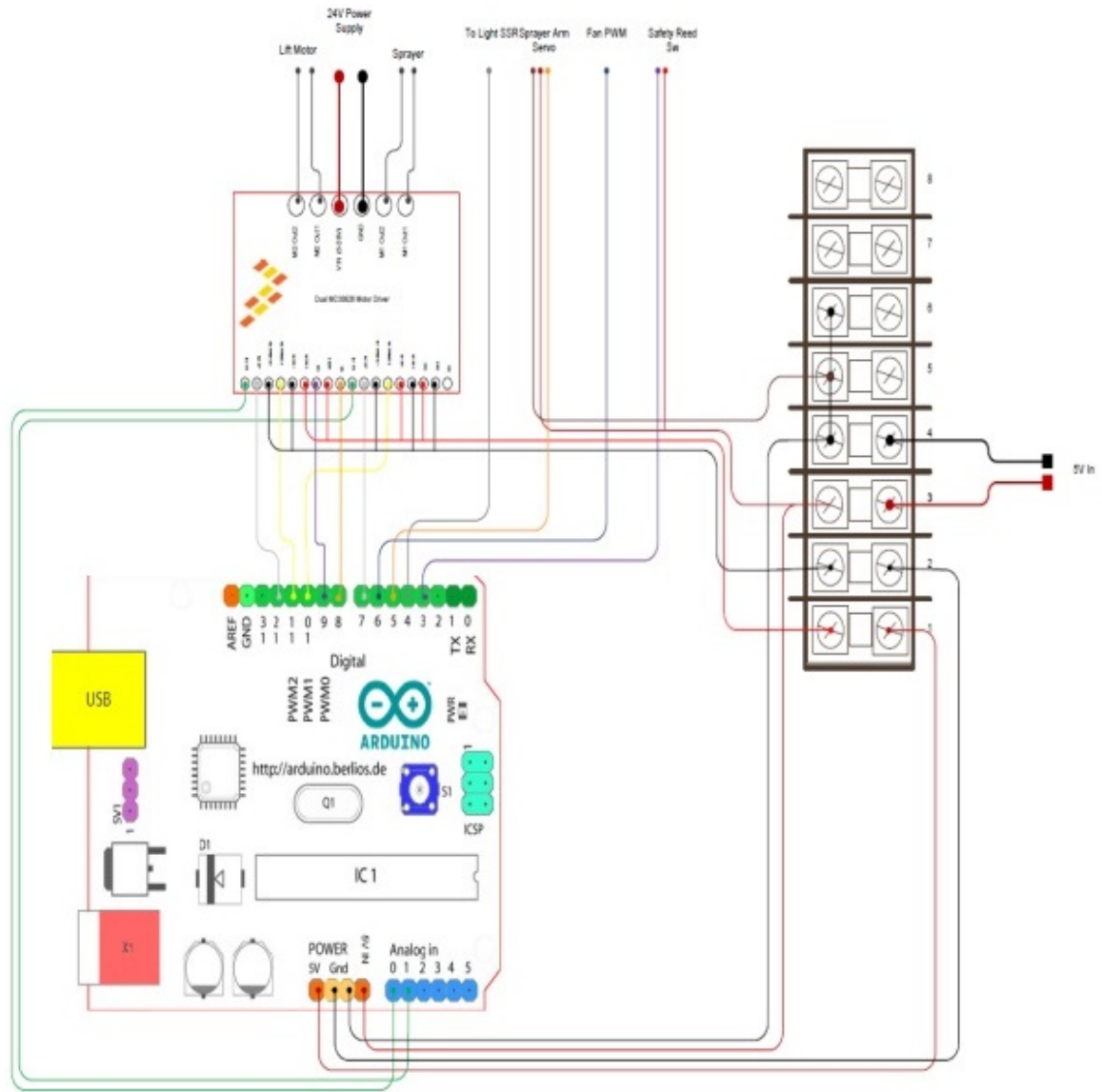


Figure III.7: Microcontroller Circuit Diagram

III.4 Photoreactor Instrumentation Design

Instrumentation was developed to accurately measure with higher precision sensors and integrated into the photoreactor. From automating the reactor, initiation of spraying over the sample test panel was achieved. This automation system protects the human from exposure to the harmful chemical agent, the simulant. By integrating instrumentation to the reactor, this allows the capture of sensor data continuously in making statistical and graphical data analysis.

After the sample test loading and spraying system are complete, no human intervention is required in the reactor. The instrumentation devices will collect the data and send to the computer via the National Instruments data acquisition device (NI DAQ) as shown in Figure III.8.

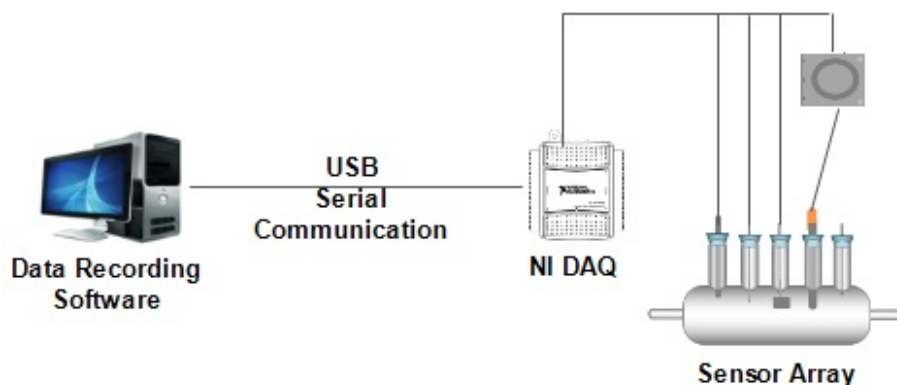


Figure III.8: Data Acquisition System

III.5 Sensors

III.5.1 Volatile Organic Compound Sensor

A high accuracy with a minimum detection of 50 ppb, piD-TECH plus Plug-in Photoionization Sensor was chosen for measuring the a Volatile Organic Compound (VOC). The sensor is build upon the principle of photoionization principle, which uses a 10.6 eV ultraviolet (UV) light lamp. The UV light causes ionization of the sample that is detected by the sensor instrument and reported as a concentration of the VOC. It has the sensing range of 0 to 2000ppm and response time of less than 3 seconds. With a capability to withstand the temperature of range -20°C to 40°C and relative humidity response to less than 0.2ppm @90%, it is an ideal VOC sensor required by our apparatus setup. Its operating voltage is 32.V to 10V with a power consumption of 64mW - 300mW. Its output signal is 0.05 - 2.5V, which can be detected by the data acquisition device and mapped to 0-2000ppm depending upon the VOC materials.

III.5.2 Carbon dioxide Sensor

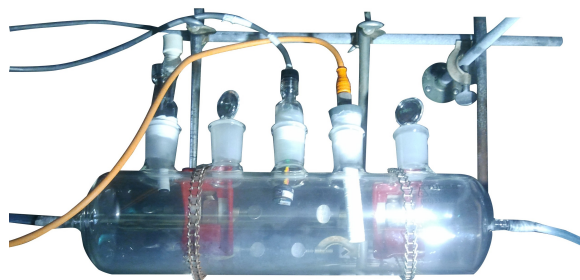
One of the harmless byproduct of the photocatalytic process is the carbon dioxide. An ISO9001 compliant, a highly accurate Vaisala CARBOCAP Carbon Dioxide Transmitter GMT222 CO_2 sensor was used to detect the level of carbon dioxide. The sensor is based on the single beam of infrared signal which is used to measure the amount of CO_2 . This sensor is capable of detecting 0 to 2000 ppm. Its nominal operating voltage is 24V AD/DC. It has a interchangeable probes which can be removed and reattached without needing to calibrate and adjust. It has analog outputs of 0-20mA, 4-20mA, and 0-10V with $\pm(1.5\%$ of range + 2% of reading) which is connected to the Data Acquisition Device. Its warm-up response time is 30 seconds. Its operating temperature range is from -20°C to 60°C , and it is rated to operate from 0 to 100% relative humidity.

III.5.3 Humidity Sensor

One of the byproducts of the photocatlytic process is water molecules, which will add humidity on the controlled chamber. It is also one of the limiting or promoting factors of the photocatalytic process which needs to be evaluated and analyzed during the experimental analysis. A capacitive humidity sensor, model HM1500LF, was used to measure the humidity in a photoreactor. This sensor is reliable, accurate, and designed for OEM application. The operating voltage requirement is 3 to 10VDC. With operating temperature range of -20°C to $+60^{\circ}\text{C}$, it can detect the humidity in the range of 0 - 100% with $\pm 3\%$ error.



(a) Ni USB DAQ



(b) Snapshot of Sensor Array

Figure III.9: USB DAQ and Sensor Array Arrangement

(a) VOC Sensor

(b) CO₂ Sensor

(c) Humidity Sensor

Figure III.10: Instrumentation Sensors

III.6 Photoreactor Setup and Operational Procedure

Connecting the air cylinder to the Reactor:

- i. Avoid sandals and wear steel toe shoes.
- ii. Wear safety eye glasses, lab coat, and industrial quality gloves.
- iii. Make sure the air cylinders are standing straight and tightened.
- iv. Make sure the regulator pressure control valve is relieved.
- v. Pressurize regulators slowly and ensure that valve outlets and regulators are pointed away from you or any personnel.
- vi. Make sure the relief valve is working by relieving pressure.
- vii. Before connecting air cylinders to the reactor, make sure the reactor electrical switch is turned off.
- viii. Connect the outlets from regulators to the sprayer inlet at the reactor.
- ix. Pressurize regulators slowly to 10psi that goes to sprayer inlet.
- x. Pressurize regulators slowly to 10psi that connects to flow controller.

Operating Reactor

- i. Make sure the reactor is plugged in to 110VAC power outlets.
- ii. Make sure the USB cable from Reactor and USB from DAQ controller are connected to the PC.
- iii. Make sure the power supply of 3.2-10VDC is connected to VOC Sensor.
- iv. Turn on the PC that has Reactor Software.
- v. Execute the Reactor Software.
- vi. Turn on the Reactor. A red LED light will turn on for a few seconds. Wait until the red LED light goes off.
- vii. Click De-pressurize on the software.

- viii. Click Fill on the software.
- ix. Open the Reactor Door.
- x. Open the swagelok valve in the sprayer.
- xi. Load the fill syringe with the desired amount of simulant.
- xii. Load the simulant on the sprayer by inserting the syringe into the sprayer and dispensing it.
- xiii. Close the swagelok valve.
- xiv. Insert the test panel coupon onto sample tray.
- xv. Close the reactor door.

Every time, after loading the simulant,

- i. Insert the blank panel and select 5 number of sprays and click "Start Process."
- ii. Click "Finish Process" and open the door.
- iii. Insert the test panel coupon onto the sample tray.
- iv. Click start process on the software with desired number of sprays.
- v. Open the Data acquisition software. Select the file name to store the sensor data.
- vi. Click "Finish Process" on reactor software.

Reactor Maintenance

- i. Fill the syringe with a cleaning agent.
- ii. Click Maintenance.
- iii. Open the access door.
- iv. Slide the container tray over and place a small beaker on it so it sits snugly over the end of the sprayer.
- v. Click Purge. Repeat until sprayer is empty.

- vi. Click Depressurize .
- vii. Open the green handle.
- viii. Insert and empty the syringe into the sprayer.
- ix. Remove the syringe and close the sprayer valve.
- x. Make sure the overflow container is in place and close the access door.
- xi. Click Purge. Repeat until sprayer is empty.
- xii. Open the access door and remove the overflow container from the enclosure.
- xiii. Click End Maintenance.

III.7 Computational Tools

There are numerous packages available for computational analysis of experimental data sets. These tool packages vary from open source to commercial products suited for small size to huge data sets both available for academic and commercial units. However, these software packages are suited for general systems or limited by a set of calculations on specific systems. For a photocatalytic researcher, the specialized software will be very useful given the scope to fit the raw data into a system to get the desired mathematical or prediction model. For a computational scientist, specialized programs are often needed to be made with specific results in mind in addition to some specific features.

In creating a prediction model from a set of raw experimental data, a custom tool will be very useful in preprocessing the raw data before analyzing it. A custom tool is therefore designed to pre-process the data and to simplify the analysis process to build the prediction model. This is achieved by utilizing the scientific computing tools available in the Python extended modules with which the user can create a specialized program for analysis.

III.8 Programming

Python is preferred for both building customized tools and data analysis. It is an object-oriented, interpreted, and interactive high-level programming language with scientific computing and optimization packages and GUI capabilities.

There are several Python-compatible libraries available based on the needs of various fields of software and hardware, which makes Python so compelling. Its compiler and many packages are open source and free that provides maximum flexibility. The most established

numerical computation packages, NumPy and SciPy are the fundamental package in Python for scientific computing and data analysis in Python, which are built together to provide many user-friendly and efficient numerical routines like integration, optimization, and more. In order to creating the user friendly GUI, wxPython is used. Matplotlib is used to create visualization of the data sets by creating interactive plots. For processing large data set, pandas is used.

III.9 IDE: Spyder

For the development environment platform, Scientific PYthon Development EnviRonment, Spyder is selected, which is a powerful interactive development environment for the Python language with advanced editing, interactive testing, debugging, and introspection features [?]. It is a free IDE tool with built in python shell. In addition to syntax highlighting the editor offers code completion, code analysis, function/class browser and horizontal/vertical splitting features. It also has a MATLAB-like workspace for browsing global variables and a document viewer that automatically show documentation for any function call made in a Python shell. Figure III.11 shows an image of the Spyder software.

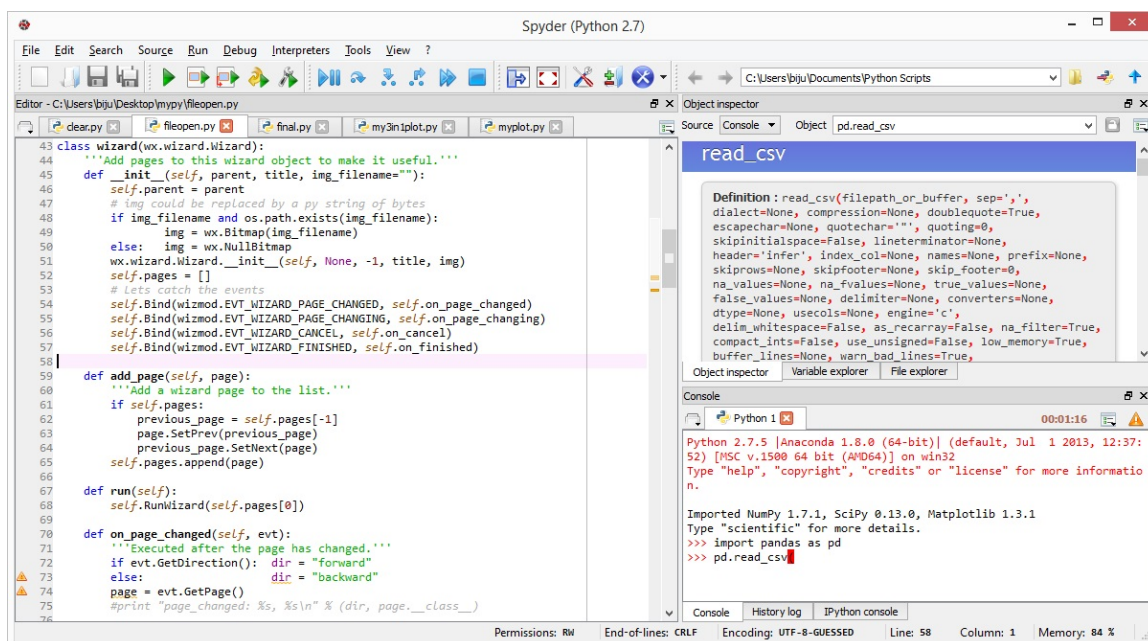


Figure III.11: Integrated Development Environment: Spyder

III.10 SciPy

SciPy is a module of scientific tools for the Python programming language. It provides a vast number of options for data analysis. The module has a highly Object Oriented (OO) approach to design, with classes being of a very fine level of granularity. For example, even the genes that make up a genotype are defined as being classes. As with libGE, this detailed and complex nature of the design results in a system that is very powerful, yet extremely difficult to come to grips with. Hence we should also bear this system in mind throughout the design stage of this project, so as to ensure that we are able to produce a framework that is simple and easy to understand.

III.11 NumPy

NumPy is a Python extension module which adds a powerful multidimensional array class ndarray to the Python language. NumPy also provides scientific computing capabilities such as basic linear algebra and Fourier transform support. NumPy is the de facto standard for scientific computing in Python and the successor of the other numerical Python packages Numarray and numeric.

III.12 Pandas

Pandas is an open-source Python package designed for data analysis which offers data structures and operations for managing and handling data in efficient way. Its feature is similar to sql which provides data slicing, indexing, grouping, merging, handling missing data etc. It has a feature to interact with well known data formats including csv, excel, sql databases, JSON, etc.

III.13 Matplotlib

The Python library, matplotlib is the most popular graphical library, which is very similar to gnuplot and a graphical interface similar to Matlab. It is a python 2D plotting library, which produces publication quality figures in a variety of hardcopy formats and interactive environments across platforms [?]. It is used in creating many interactive visualization like plots, histograms, power spectra, bar charts, errorcharts, scatterplots, etc.

III.14 wxPython

wxPython is a cross-platform GUI toolkit for the Python programming language. It allows Python programmers to create programs with a robust, highly functional graphical user interface, simply and easily. It is implemented as a Python extension module that wraps the popular wxWidgets cross platform GUI library, which is written in C++ [?].

The open source cross-platform, wxPython libraries, is the frameworks for windowing and visualization of an application. Graphical user interface (GUI) is developed using wx-Python to incorporate several computational functions, graphical analysis, and experimental data handling as shown in Figure III.12.

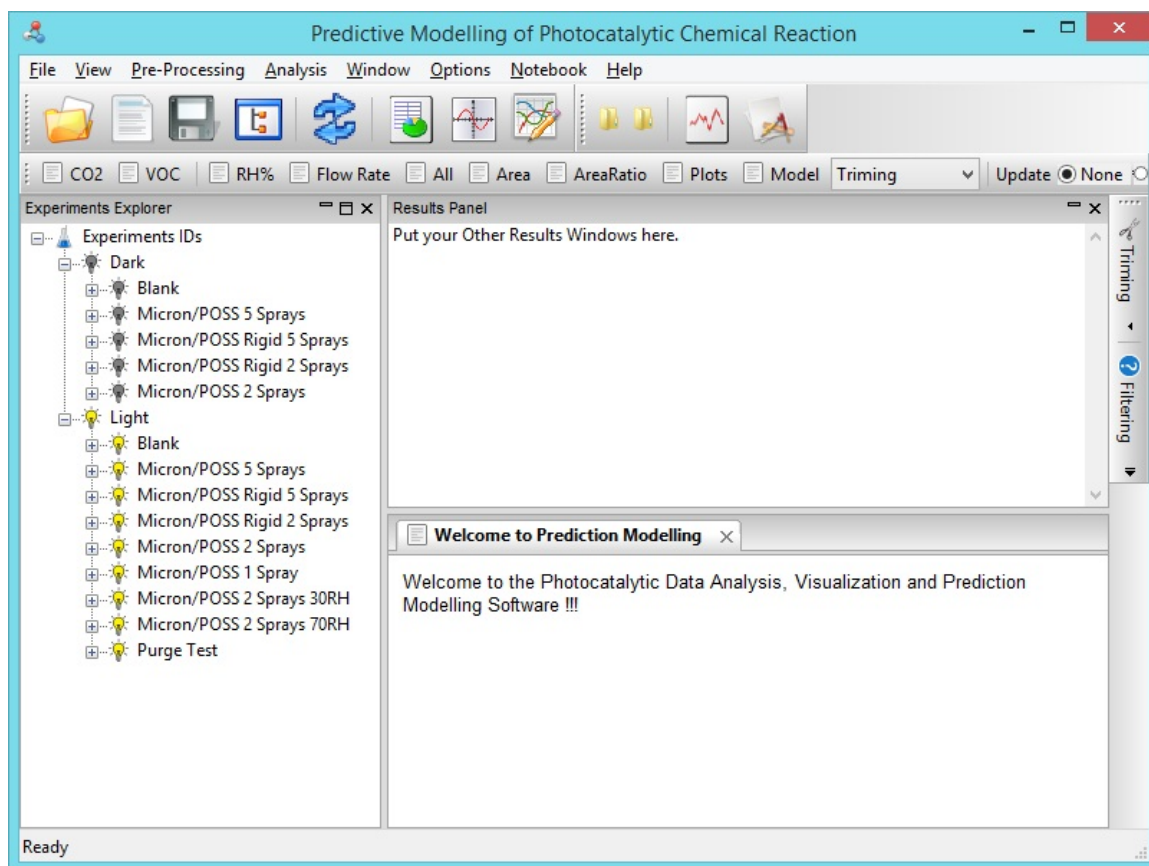


Figure III.12: A Graphical User Interface(GUI)

Chapter IV

Experimental and Computational Methods

IV.1 Overview

In this chapter, a detailed description of the experimental procedures adopted in this project is presented, to ensure the repeatability of the project. The first part gives all the preparation of the equipment and materials. This part describes the main steps taken to conduct the experiment. The second part gives the data analysis methods using visual analysis of data, computational tools, and building the customized tool to analyze the raw experimental data. The last part of this chapter explains the process of building the mathematical model of the experiments.

IV.2 Experimental Setup

Each experiment is a time series data consisting of four parameters: CO₂, VOC, relative humidity and air flow quantity, which are obtained through a series of experiments. Experiments are performed in two different conditions. At first, experiments were performed in dark conditions at three different simulant quantities at different humidities. These experimental sets give the baseline for analysis of the data where there is no photocatalytic activity. In the second condition, experiments are performed in light without the photocatalyst and then with the photocatalyst at three different simulant quantities at three different humidities. All these experiments are conducted in constant air flow stream of 100mL per second. These experimental sets are as depicted in the Figure IV.1.

IV.3 Calibration

Before conducting an experiment, the measuring devices need to be calibrated as specified by the product vendors. It is a process of establishing a fixed relationship between a known quantity and variables of a sensing device. So its purpose is to relate the known quantity to the measured attributes. In our experimental apparatus, the sensors that we used are already calibrated by the manufacturer which removes the burden of calibrating the devices again and again. However, over time, it needs to be calibrated again. To tackle this problem, through mathematical and statistical methods, calibration error can be minimized. Since in

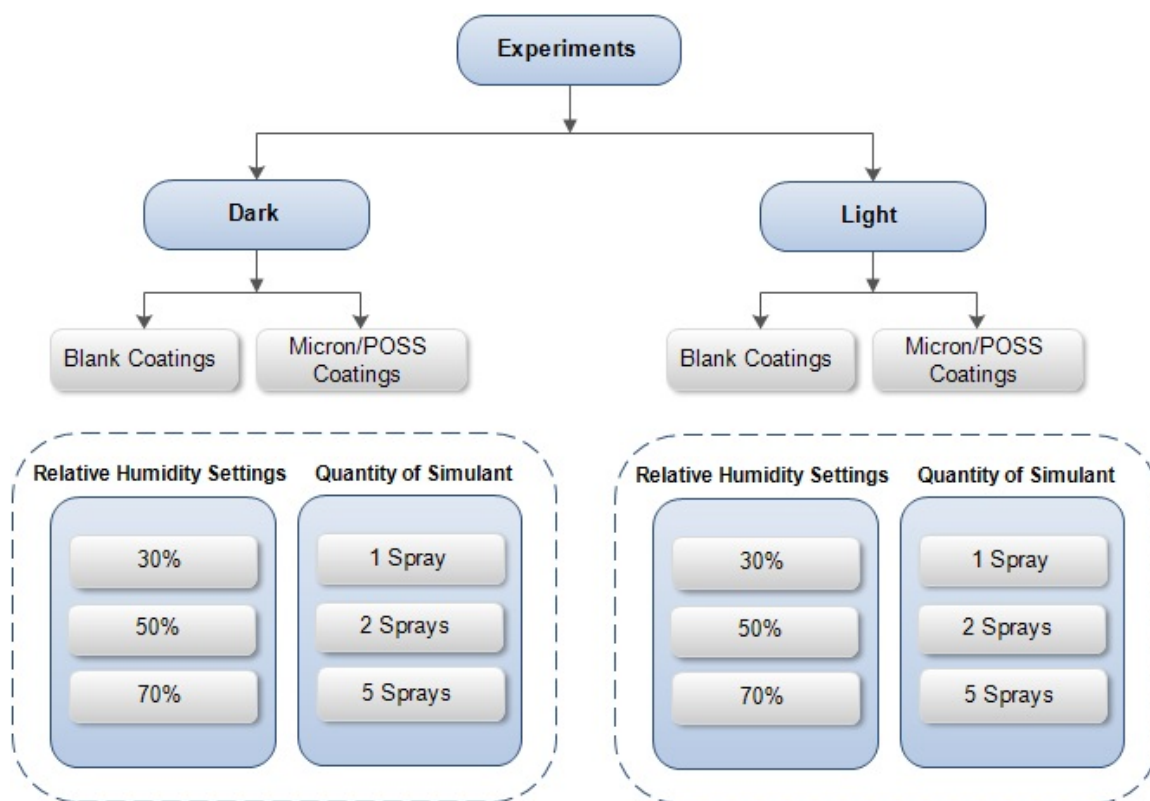


Figure IV.1: Experimental Setup

this dissertation, all the recorded data are used to do ratio analysis of the area generated by the curves of respective parameters, total area generated by the curve of each parameter are not affected by any offset error in the reading; however, there needs to be a method to derive a baseline of the curve. The method to detect the baseline of the curve is described in the next chapter.

IV.4 System Integration

To conduct a photocatalytic activity, there is a need to develop a complete system which automates the entire photocatalytic process including preparation of the consumable, deliverables, and the data analysis component. The program has implemented a hardware and software system that enables functional modules to be linked together to perform desired data analysis. The software for hardware control and computational analysis is categorized into two groups, on-line software and off-line software, which is depicted in Figure IV.2.

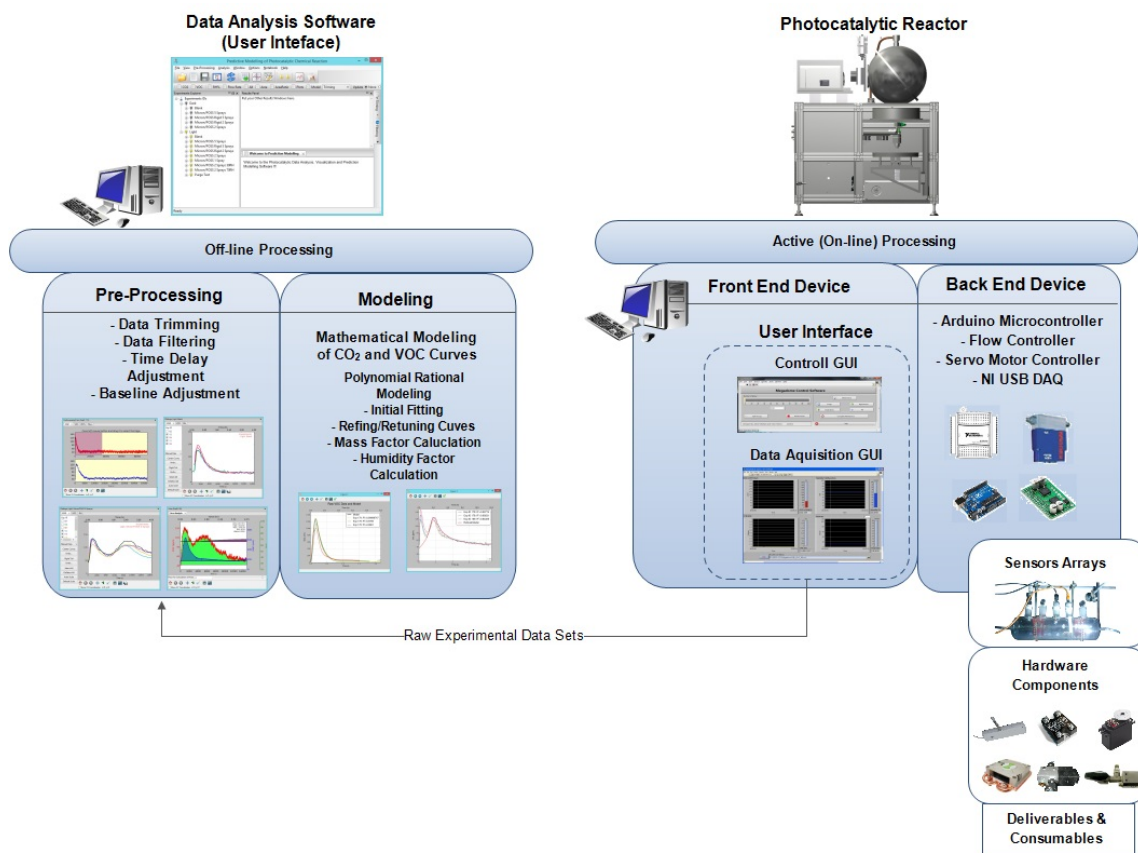


Figure IV.2: A Overview of the System Architecture

IV.5 User Interface

IV.5.1 On-line User Interface

All the associated process are initiated by preparation of the deliverables and consumables, which are then used for the photocatalytic process inside a controlled chamber via user control through a software interface. A user interface based on the LabVIEW system is used as a control software interface for the complete automation system of the process in the photoreactor. The communication between the software and hardware controller is executed via a USB serial communication link. The LabVIEW executable interface program is used for data acquisition (Figure IV.3), and device control LabVIEW executable (Figure III.3) will communicate to Arduino Controller via USB communication. This software is categorized as on-line software because it directly interacts with the hardware in action for operating the photocatalytic chamber.

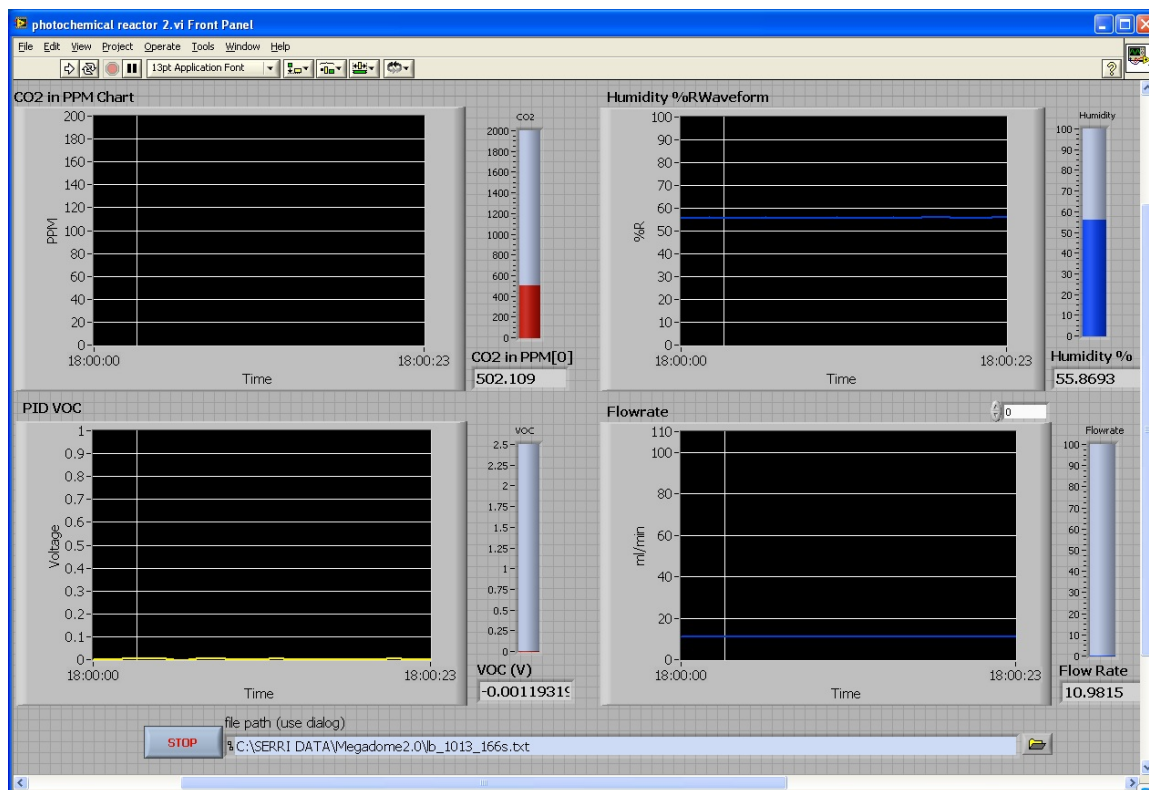


Figure IV.3: A LabVIEW User Interface for Data Acquisition

IV.5.2 Off-line User Interface

All of the graphical analysis used to interpret the model is used from the customized off-line tool, which is built in Python Programming environment, and wxPython is used to build for windows environment. Interactive user actions to make appropriate displays, selection of experiments, and handling the raw experiments are done via this off-line user interface. All the experiments have a uniquely identified experiment identification number (ExpID). The programming software environment is Python 2.7 64-bit version. Even though the Python 3.4 version is available, most of the libraries do not yet support the 64-bit libraries. Version 2.7 widely supported most of the tools built on the 64-bit system, which helps to remove unnecessary burden to deal with the different versions and 32-bit vs 64-bit issues.

IV.6 Preparation of Deliverables/Consumables

The photocatalytic process requires deliverables and consumables. The following section briefly describes the preparation of the deliverables. They are as follows:

- Preparation of Light Source

- Preparation of Dispersion
- Coating Preparation and Activation
- Surface Decomposition of Chemical Analogue
- Preparation of Sprayer
- Maintenance of the Sprayer

IV.7 Light Source

The synthesis or degradation of a simulant in the presence of the TiO_2 photocatalyst requires a light source. A light source with different wavelengths or intensities has a great impact on the degradation of the simulant. Several experiments concerning the synthesis of a simulant and a light source have been well documented via the published studies concerning its degradation by-products in the presence of TiO_2 photocatalysts. Although not performed under real-world scenarios, they provide a ready source of information [24].

During this project, the agent was applied to the substrate, a sample test q-panel via a spraying method. These coated sample test q-panels are pretreated with humidity and a UV light source. The high pressure mercury lamp was used with the provided intensity of ultraviolet radiation during the experiment as the light source as shown in Figure IV.4. To conduct a photocatalytic degradation, these coated panels are exposed to the simulant in the presence of light irradiation inside the reactor. Constant illumination of light is provided throughout the period of reaction. Over a period of reaction, volatile organic compounds along with CO_2 and water were produced. These products are measured using a designed sensor array, based on reported success of simple conductivity-based detectors [25]. Throughout all experiments, thermal and dark controls (coatings present in the reactor but shielded from irradiation) of experiments as well as catalytic controls (substrates with no photocatalytic coating) were performed as a reference.

IV.8 Dispersion Preparation

The TiO_2 and trisilanol isobutyl polyhedral oligomeric silsesquioxane (TSI-POSS) compositions were held constant at 10:1 wt/wt% in the following procedure.

- Using a Flacktek speed mixer, TiO_2 and TSI-POSS solids were combined and placed under high shear for 5 minutes.

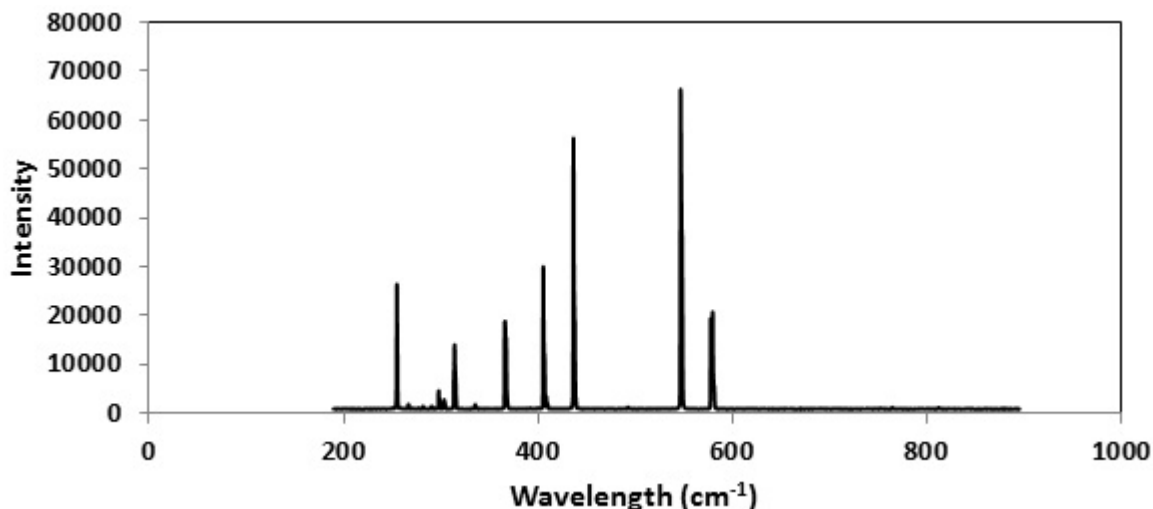


Figure IV.4: Ocean Optics Spectra of High Pressure Mercury Lamp

- Acetone was added to the solids to achieve a 5 wt % solids dispersion.
- Combining the speed mixer and a Fisher Scientific Model FS110 FS 20 sonicator, the dispersion was alternatively placed under high shear with glass beads followed by sonication in 5 minute increments each for three cycles.

IV.9 Coating Preparation and Activation

Photocatalysts used throughout the experiments were simple physical mixtures of metal and semiconductor nano-particles. The specific methods used to prepare these photocatalysts are described in the following sections. In general, all of the nano-particles were suspended in ethanol, then mixed to create composite suspensions. Using ethanol, the solvent was important. Water could not be used because its surface tension is too high, and it did not properly wet the substrates, which caused uneven drying and sometimes led to solids flaking off when submerged in water.

The dispersions were transferred to an Iwata Eclipse Gravity Feed Airbrush-CS-Size: 0.35mm/ Testors Blue Mini Airbrush with compressor. The substrates, aluminum Q-panels (3" x 6"), glass microscope slides (3 x 1 x 1.0mm), and silicon wafer chips, were sprayed with the dispersions in an interlaced spray-pattern at a distance of 30 cm. A horizontal pass plus one vertical pass over the substrate is considered one coat, and a total of 10 coats were applied. Coatings were dried between each coat in a Fisher Isotemp Oven at 50°C for 2 minutes. All coatings were stored in a desiccator at ~2% RH prior to use.

The 23.594"L x 17.719"W x 14.438"H photoreactor features a temperature controlled 20.625"L x 9.563"W x 1.531"H sample plate, 5 lamp holders, 30 CFM exhaust fan, and independent controls for the fan and lamps. Humidity is measured with an installed semiconductor-based 10-95% relative humidity range sensor. Temperature is measured via a thermocouple type K with a range of -200 to +1250 °C. The sample chamber is constructed of a 8.375" x 5.375" x 1" (7" x 4" x 0.8" internal) aluminum rectangular housing with an o-ring seal and pressure controlled latching. An inlet allows flow of desired pressurized air or gas and an outlet connection is provided for application to a bubbler container and/or a gas analysis system.

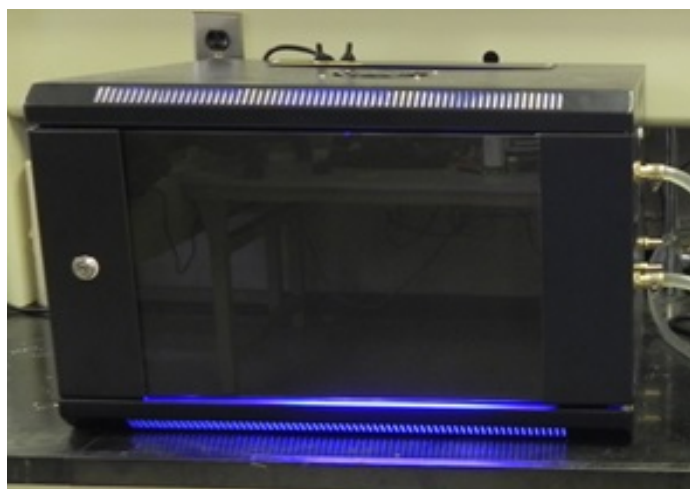


Figure IV.5: Novel Photoreactor Manufactured to conduct UV-conditioning of Samples while controlling Humidity, Temperature, and Light Exposure

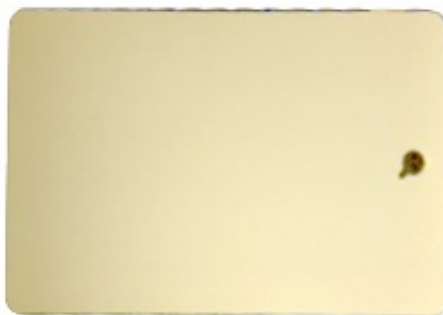


Figure IV.6: Sample Coating Q Panel

IV.10 Surface Decomposition of Chemical Analogue

The chemical agent that the team decided to analyze is 2-chloroethyl ethyl sulfide (half-mustard). Experiments with varying concentration and humidity have been performed with the simulant shown in Figure IV.7. This simulant was chosen due to the significant threat the agent poses and due to its ability to readily absorb into substrates, a characteristic of importance to this project. Furthermore, the agent is also inexpensive, readily available, and requires minimal special handling protocols.

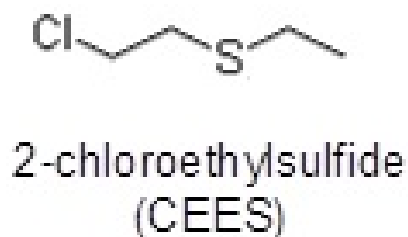


Figure IV.7: Molecular Structure of Mustard Gas Chemical Agent Simulant

IV.11 Preparation of Sprayer

The automatic sprayer nozzle provides accurate spray placement with desired spray pattern. One of the objectives in using the automatic sprayer is to save the expensive chemical by spraying only the required amount of it. Every time before starting the experiment, the sprayer needs to be cleaned; if not we need to proceed with the cleaning procedure.

The spraying reservoir is need to be filled with simulant by feeding syringe. Every time, after filling the simulant, it needs to spray at least five times, which can be done through given reactor software. This is required to build up the line pressure into the sprayer. Since the nozzle delivers at a rate of 0.47 gpm at 100 psi, the amount of spray will be different at different pressures. We need to measure the amount of spray a couple of times. If the measure is not consistent, we need to check the line pressure.

IV.11.1 Cleaning/Maintenance of the Sprayer

After completion of an experiment or when the photoreactor is not required after an experiment is finished, the sprayer needs to be cleaned to remove any residual simulant in the sprayer. This can be done by dis-assembling the sprayer. The dis-assembled sprayer is shown in the Figure IV.8. All the parts of the sprayer need to be cleaned with alcohol.



Figure IV.8: Dis-assembled Sprayer

IV.12 Computational Methods

Several sensors' raw data is collected over a series of experiments conducted over the years of the research period. This raw data needs to be analyzed either computationally or graphically. Graphical analysis can be conducted by leveraging human capabilities using interactive graphics. Computational methods are used to analyze the huge raw data sets, while the interactive visualization is used to get the deeper insight into the underlying hidden phenomena on the data sets. With only computational methods, data analysis may lead in the wrong direction and needs to be reanalyzed and redesigned all over again both theoretically and mathematically. To aid the computational analysis, an interactive visual analysis needs to be done, which provides the insight to the data analysis to choose the proper settings of computational tools and parameters.

The user interface is used to enable a user to interactively explore and configure the experiments, which will help for both visual processing and modeling operations that are needed for the analysis of photocatalysis. The whole analysis system consists of two systems:

- Interactive Visual Analysis
- Computational Analysis

IV.13 A Software GUI: Interactive Visual Analysis

The base layout of the main user interface is shown in Figure IV.9. The main window of the user interface is a collection of Plot Frames, Window Frames and Panels embedded into the single large window. The plot frames are graphical displays of a number of raw and pre-processed raw data. The windows have interactive mouse control of the zoom limits, and pane views. A scrolling table is used for viewing the raw data sets, which can be viewed,

modified, and saved, although it is not advised to modify the raw data sets manually.

For effective visual analysis, an appropriate visual tool is required. However, there is no perfect tool available that suits our needs. For analysis of raw data and managing it, a customized tool is required. This customized tool is built by using the Python programming languages and wxPython library to make a user friendly graphic user interface GUI as shown in Figure IV.9. From this user interface, users can manage and explore the experiments identified by the experiment IDs as shown in Figure IV.10. The raw data can also be explored, edited, and saved.

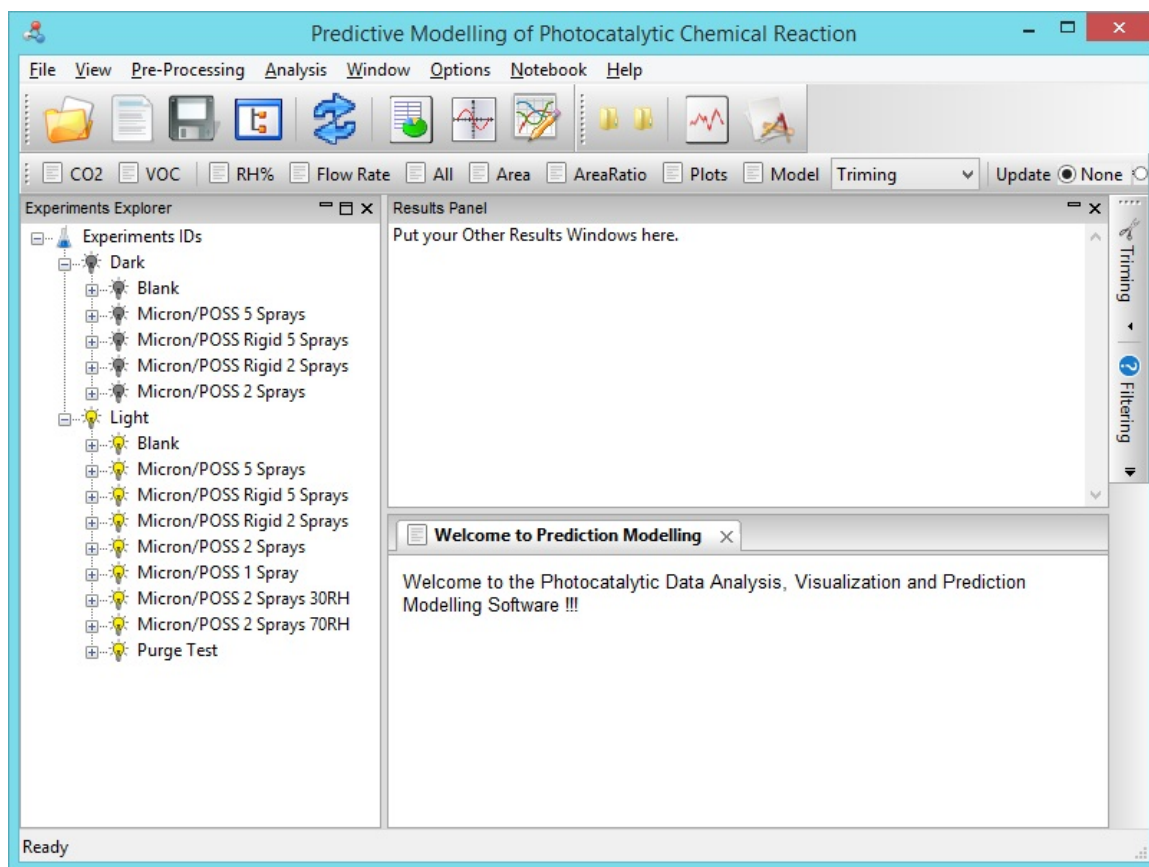


Figure IV.9: Photocatalytic Data Analysis, Visualization and Modeling Software Platform

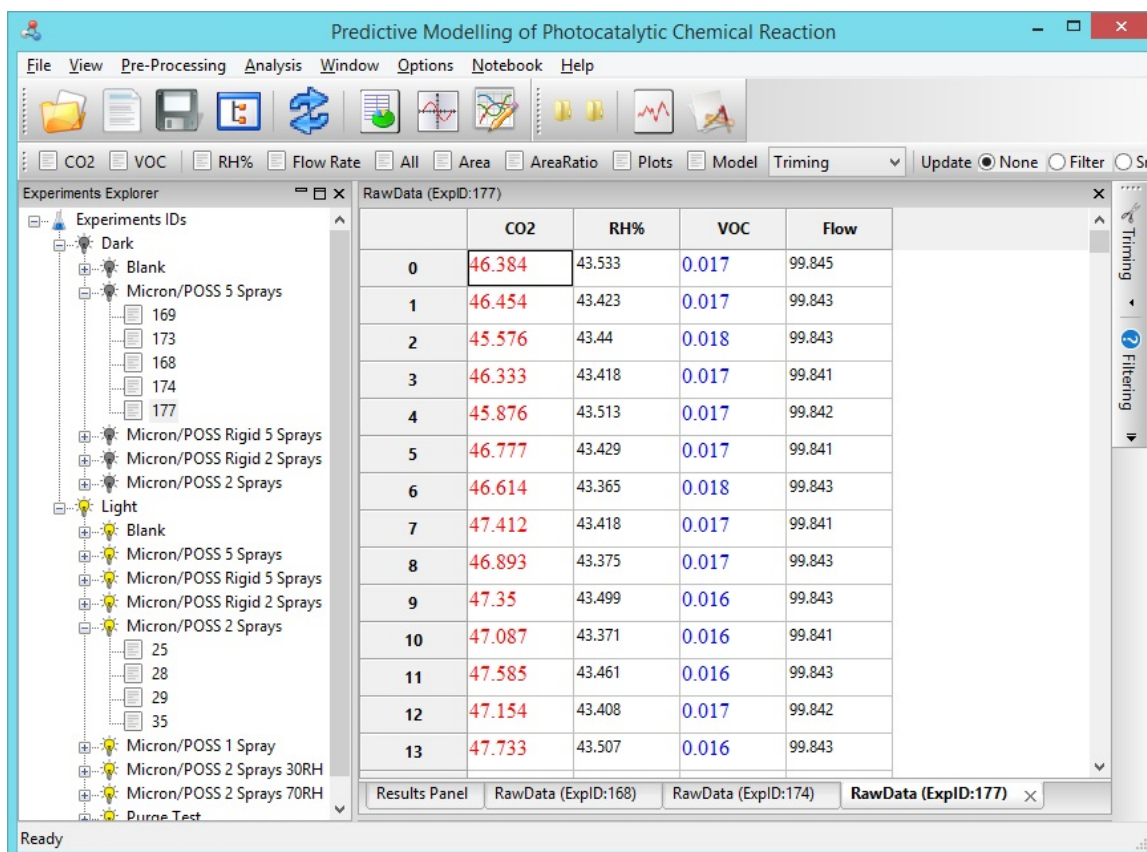
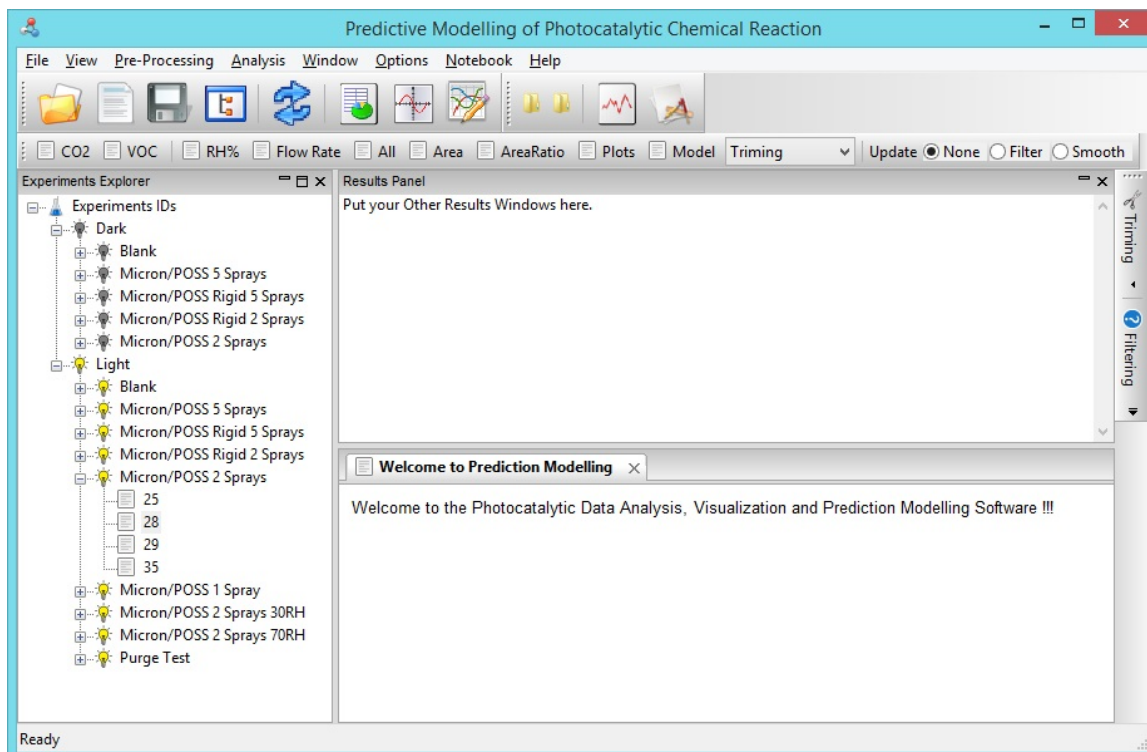


Figure IV.10: Experiments and Data Explorer

IV.14 Importing Raw Data

The raw data collected from the sensor array of the reactor in the txt format is imported as shown in Figure IV.11. The user interface allows browsing the file location and selecting the file to import. The second step allows selection of the experimental condition. In the third step, the user can either select the coatings type or give a new name for the coatings. Finally, unique experiment IDs need to be entered and the file is imported into the system.

(a) Select File

(b) Select Light Condition

(c) Select or Give Coatings

(d) Give Experimental ID

Figure IV.11: Experimental Raw Data Import

IV.15 Raw Data View and Area under Curve

By using the Python Matplotlib library, a canvas figure is built as shown in Figure IV.12. This is an interactive plot with three different y-axes, CO₂ in ppm, VOC in mV and relative humidity in %. Each y-axis represents the same color as the color of the corresponding curve. The area under the curve is based on the initial value of each component so that the total produced CO₂, VOC or humidity can be calculated. This plot has all the figures provided by the Matplotlib which can be zoomed in/out, moved around, and saved in any location provided by the standard Toolbar given at the bottom of the plot. The x-axis scales in the bottom of the plot are in seconds whereas the top x-axis scales are in hours. With appropriate selection of the slider value or from the text value, the area is calculated and displays in the top right corner of the plot.

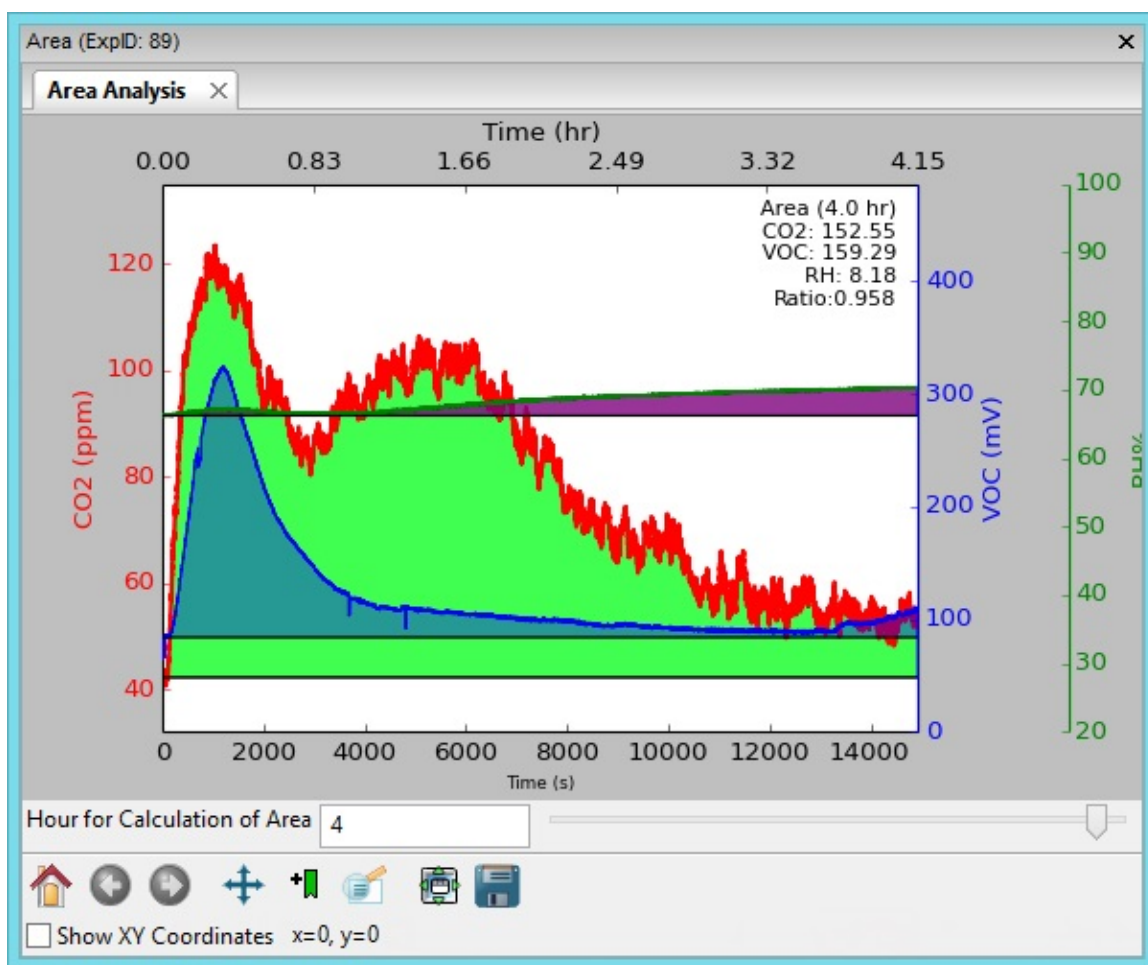


Figure IV.12: Area Plotting for 4 Hour Data

IV.16 Preprocessing of Raw Data

Preprocessing of the raw measured data enables a more robust operation of the subsequent data analysis. The preprocessing consists of removal of the noise and trimming of long recorded data. The baseline of the raw data is estimated to calculate the area under the curve taking weighted average of the initial response of the sensor. Some unusual noise is filtered to visualize the raw data more clearly on the screen. The following section explains in more detail the preprocessing of the raw data.

IV.17 Trimming the Raw Data

The raw experimental data is captured by the sensors and recorded by data acquisition software. Since the reactor and data acquisition software run unattended, this may record the data over an extended period. From visual inspection, we can easily identify from the plot shown in Figure IV.13, that CO₂ production has already finished and trailing values recorded are not necessary. These trailing data unnecessarily add the payload on the computing performance. So we can trim them by selecting the window from the top section of the plot. The bottom section of the plot will display the curve from selected window. After selecting the needed portion of the curve, this needs to be saved by clicking the save button available on the toolbar. During the experiment, four parameters are recorded, which are given in the tabbed pages and can be selected and perform interactive actions individually. Trimming the data will ease the processing unit.

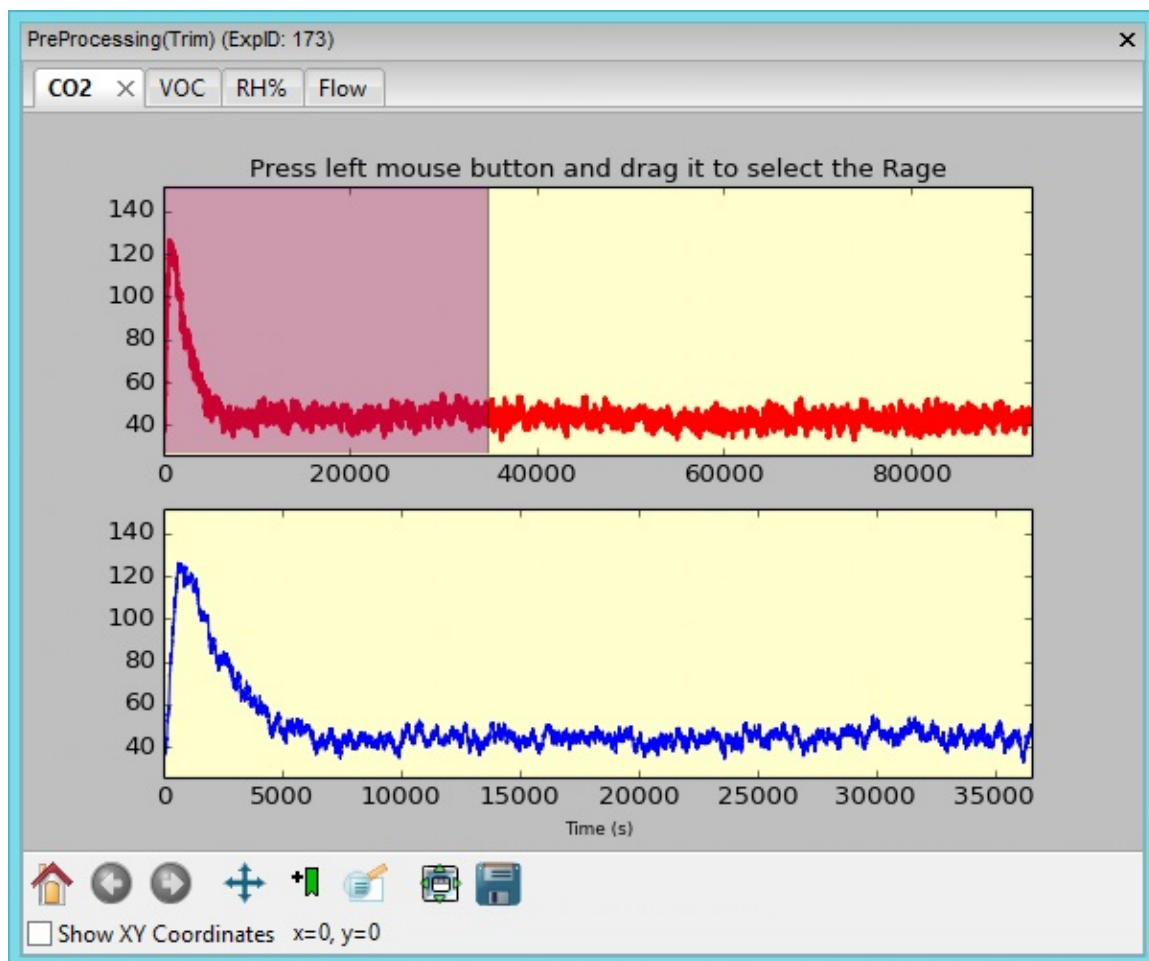


Figure IV.13: Trimming Raw Data

IV.18 Filtering Data

Raw experimental data occasionally collects the noise as shown in Figure IV.14. Noise is usual or normal in most of the experimental cases. Removing the noises eliminates the complexity of the mathematical pattern and also removes the extra burden to the processing unit. However, there are several filtering methods available for pretreatment of the data before analysis based on the nature of the noise presented in the data. In our experimental case, two methods are used, median filter and Wiener filter.

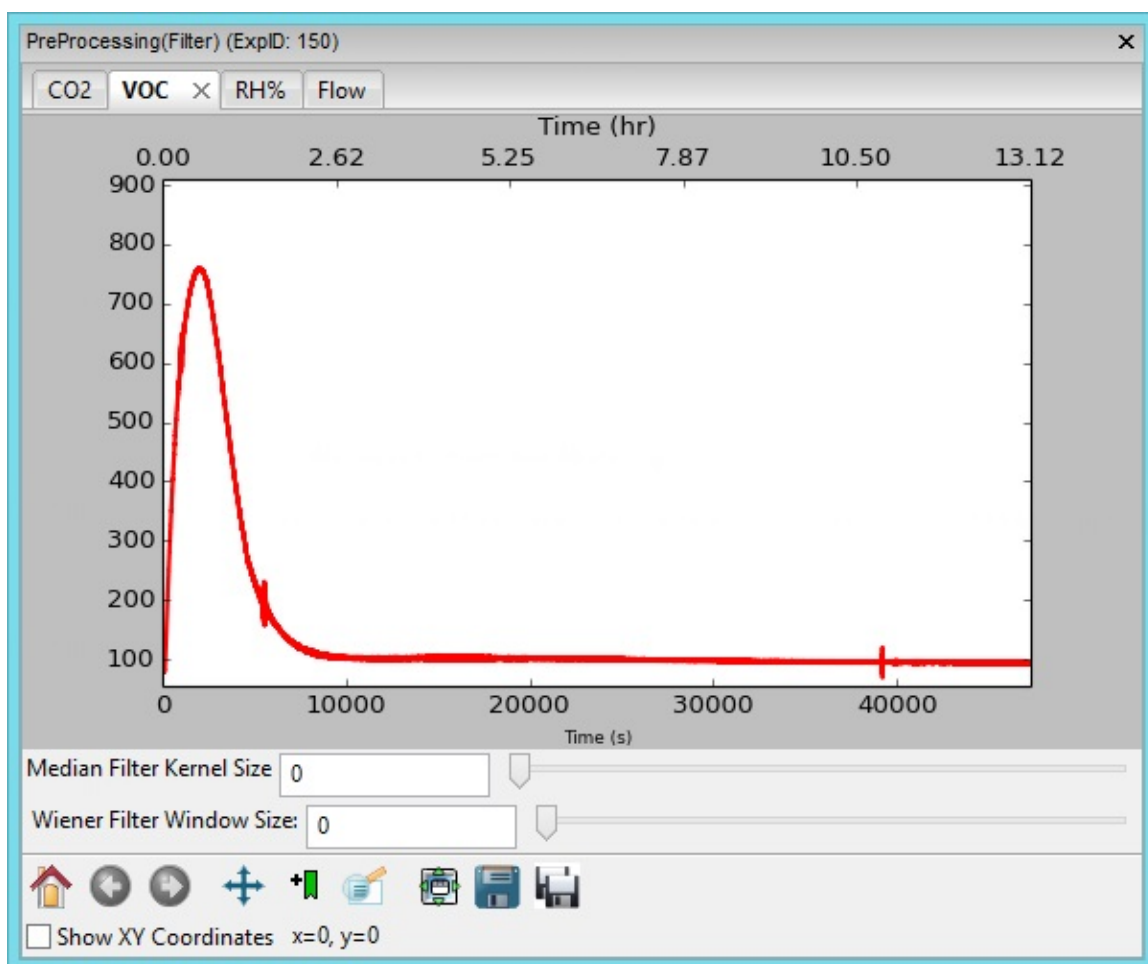


Figure IV.14: Filtering Raw/Trimmed Data

The median filter is a non-linear filtering method in signal processing and smoothing function. The median filter is based on the median values of neighboring data points specified in the kernel size. Another filtering method called the Wiener filter is also provided in the software, which is based on a linear time-invariant filter. A user can apply a median

filter, a wiener filter, or both, which is sufficient to remove the noises as shown in Figure IV.15. A filter can be applied to the raw data or trimmed data.

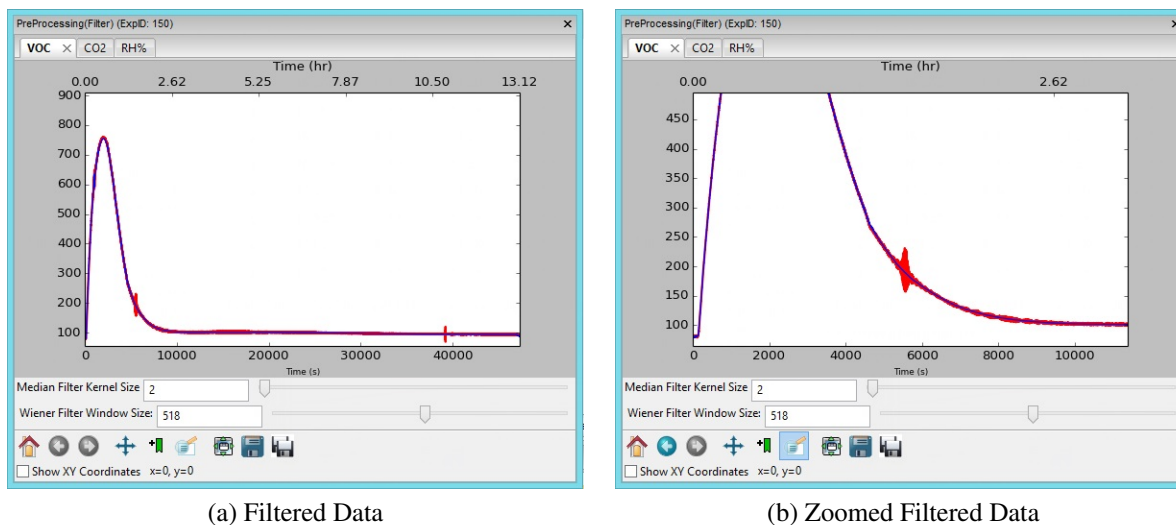


Figure IV.15: Filtered Raw/Trimmed Data Import

IV.19 Smoothing Data

The exponentially-weighted moving average can be applied to the raw data or trimmed data. Smoothing data removes the irregularities of the data by slowly decaying them to produce a smooth curve. It is used to remove the noise in time series by taking the average of neighboring points about the given value. Smoothing of data is shown in Figure IV.16.

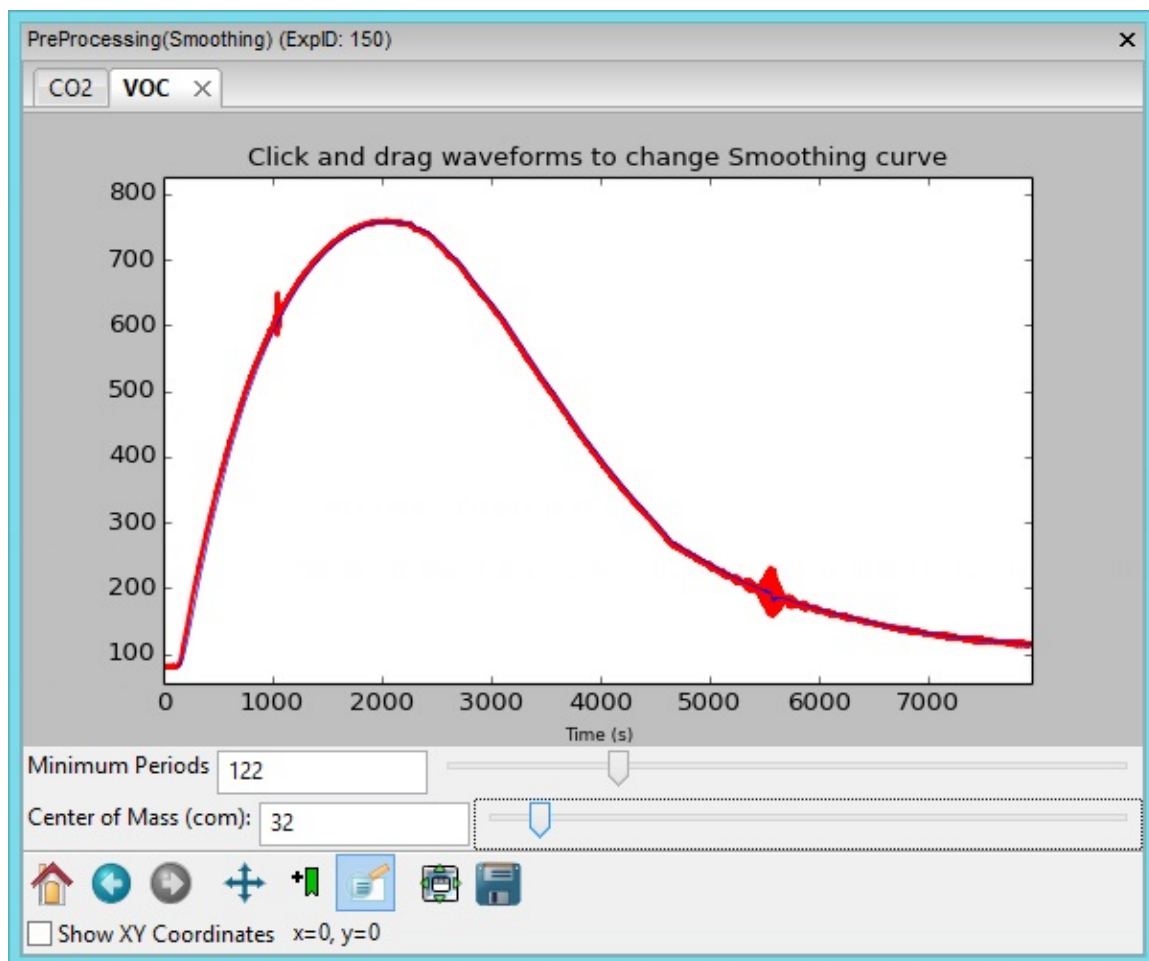


Figure IV.16: Smoothing Data

IV.20 Plotting Preprocessed Data

Preprocessed data is the data after noise removal, smoothed or trimmed data. After preprocessing, these data sets can be plotted as shown in Figure IV.17, IV.18, and IV.19. From this interactive plotting, each experiment can be selected by clicking the corresponding checkbox given in the left side of the plot. If the data recording software is executed after the start of the experiment, then the curve may not be aligned in the same location. This can be adjusted by clicking the "Center Curve." There may be some offset error on the experimental data. This means sensors need to be re-calibrated, otherwise, this can be adjusted programatically.

By default, curves are adjusted to 4 hour time window. By clicking on "Auto Scale," all the data points in the curves are automatically adjusted and made to fit in the visible plot.

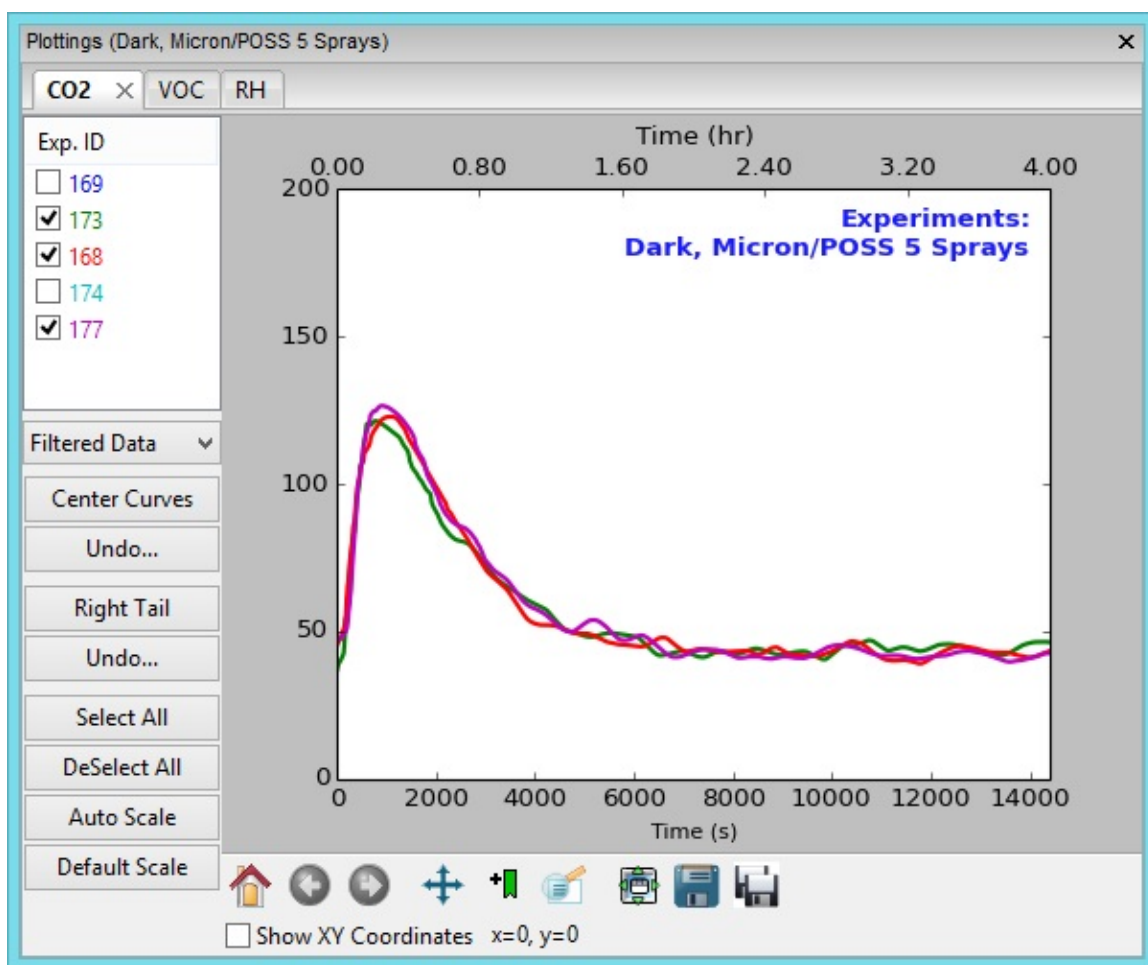


Figure IV.17: CO₂ Plotting

The selected experiment IDs are remembered. Selections are immediately saved on its program initialization file, so after restarting the program or accidental shutdown of the computer, it doesn't lose the selection. There are tabbed pages, which can be loaded by clicking on the ribbon bar on the main GUI. Data will be loaded only if they are visible or made visible by clicking from the menu or ribbon bar.

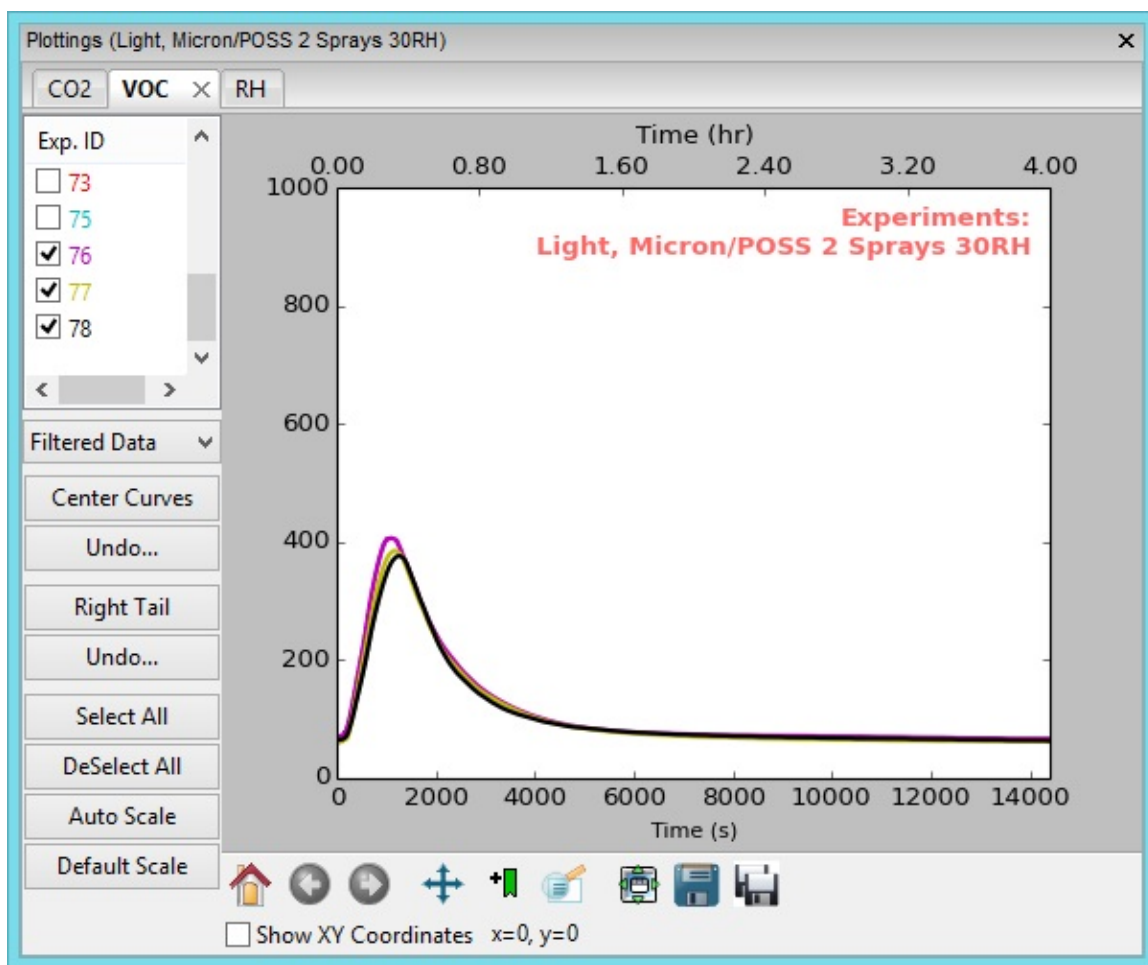


Figure IV.18: VOC Plotting

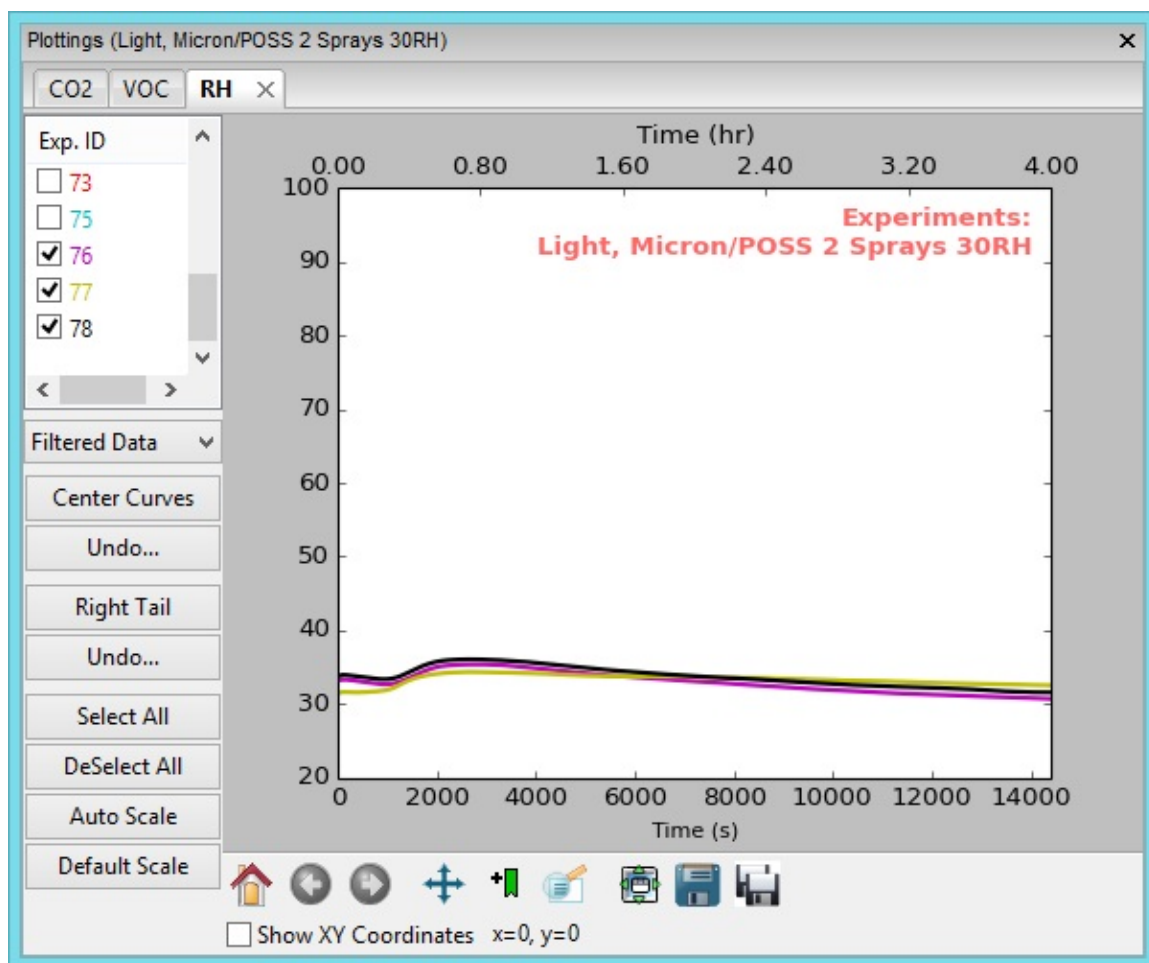


Figure IV.19: Humidity Plotting

IV.21 Computational Analysis Methods

Computational analysis is the process of building a mathematical model from the collected raw experimental data. In this section, the step by step process is explained to formulate the mathematical model. The data analysis and model are developed for CO₂ and VOC separately.

IV.22 Analysis of CO₂ Data

Several experiments' worth of data are collected. Since the purpose of the study is to analyze the photocatalytic activities, experiments are conducted in three different sets, presence of light, without light, and without any catalyst as shown in Figure IV.20. From these figures, it is clear that at the first peak of the curve, CO₂ is introduced into the reactor during spraying of the simulants, which lasts for a few seconds. During this opening of the chamber, there is a chance of CO₂ being present in the air to introduce inside the chamber. The amount of CO₂ may be different depending on the air movement near the chamber; however, they are consistent in most of our experiments.

In a continuous flow system, it is obvious to have a rise in the curve and a descend of the curve. Ultimately these curves comes down to a position where they started. There would be another rise of curve if additional amounts of CO₂ are introduced into the system. Since the chamber is closed, the second peak must have occurred from the degradation of the simulant inside the chamber, which also diminishes ultimately to a starting level of CO₂ depending on the degradation rates.

The first peak of the curve always appears due to the opening of the chamber, which can't be avoided due to design factors of the reactor. This can be removed by decomposing this composite curve into separate curves.

IV.23 Decomposing CO₂ Curve

Since the first peak of the curve occurred with the introduction of CO₂ into the chamber, it needs to be decomposed so that we can isolate this from the real CO₂ curve occurred by the degradation of the simulant. By visually analysing the curves as shown in Figure IV.22, it is possible to separate the curves. We can roughly estimate whether we can directly remove the first curve and use the second curve. For this, the area under the curve is calculated. By deducting the red area from the total curve and the green area is almost equal as shown in the following steps.

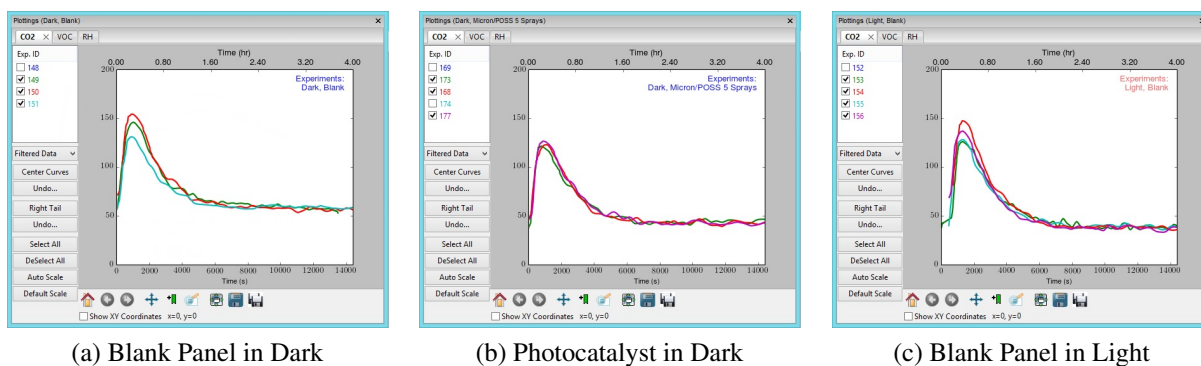


Figure IV.20: CO₂ Curves in Photocatalytic Process

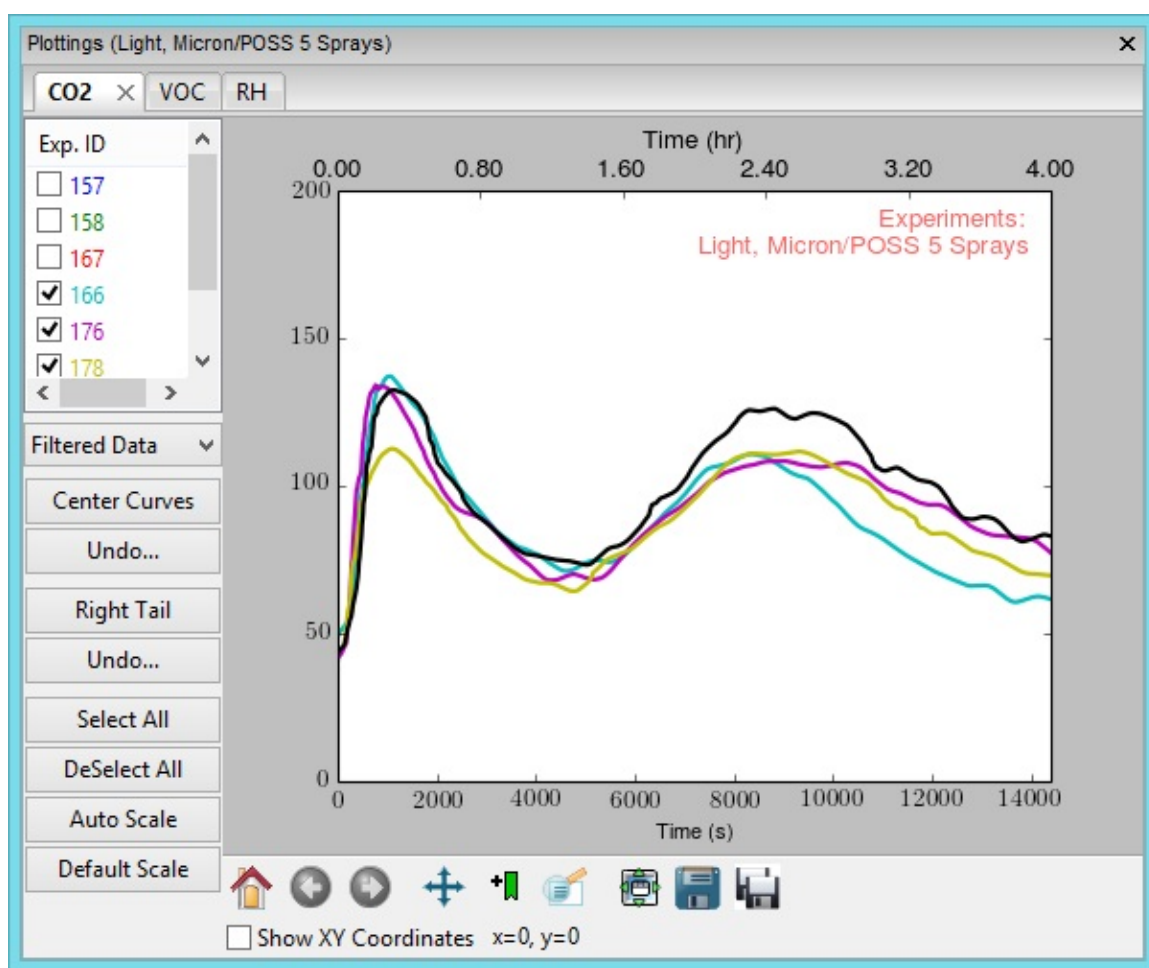


Figure IV.21: CO₂ Curves in Light with Photocatalyst

$$\text{Total Area under Curve} = 219.41 \quad (\text{IV.1})$$

$$\text{Red Shaded Area} = 72.63 \quad (\text{IV.2})$$

$$\text{Green Shaded Area} = 145.79 \quad (\text{IV.3})$$

$$\text{Total Area} - \text{Red Shaded Area} = 146.78 \quad (\text{IV.4})$$

$$\text{error} = 146.78 - 145.79 = 0.14 \quad (\text{IV.5})$$

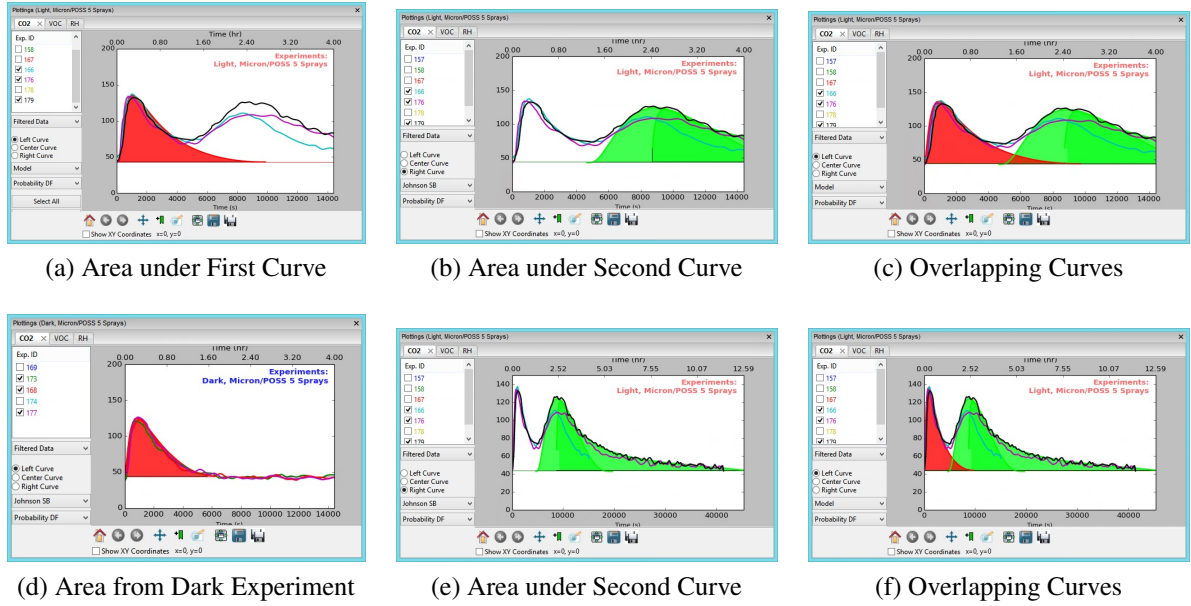
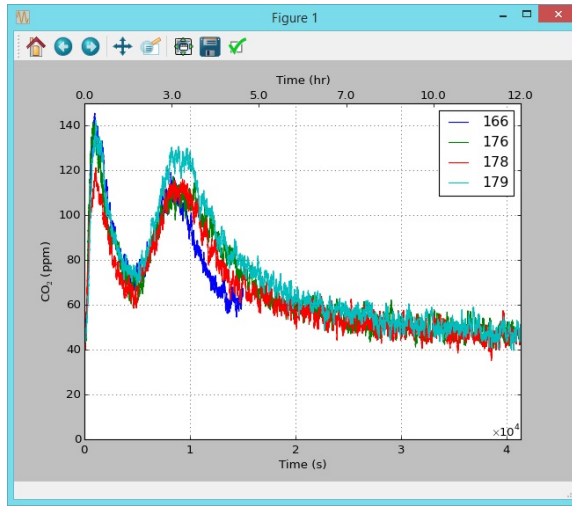


Figure IV.22: CO₂ Curves from Degradation Process

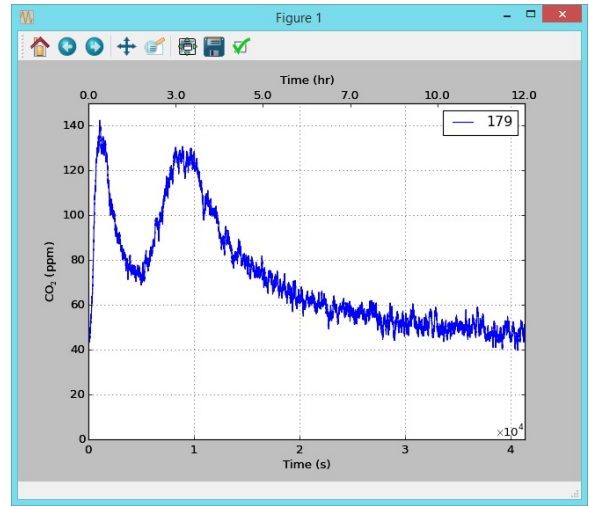
IV.23.1 Method of Decomposing the CO₂ Curves

It is roughly estimated in the above procedure to check if it is possible to directly get the second curve by removing the first curve from the point of intersection between the curves. The raw CO₂ data from multiple experiments set under the same conditions are visually inspected (Figure IV.23). The Raw Data of experiment ID 179 is selected for further analysis to decompose into two separate curves. Preprocessed curves, as shown in Figure IV.23, are

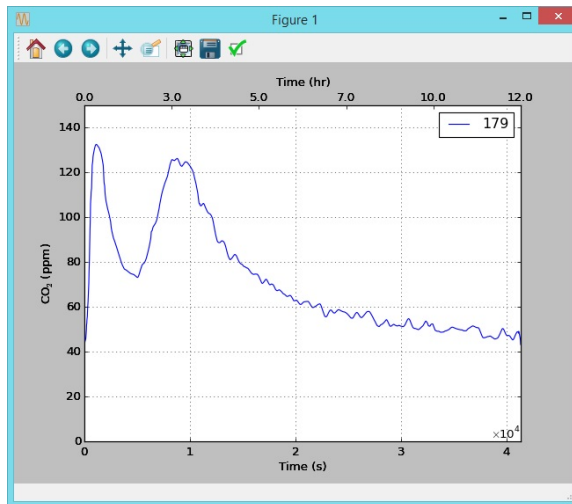
separated from the first curve from the point of intersection, which is the minimum point of the well formed by two peaks. This separated curve is then analyzed to form the model, which is described in further procedures below.



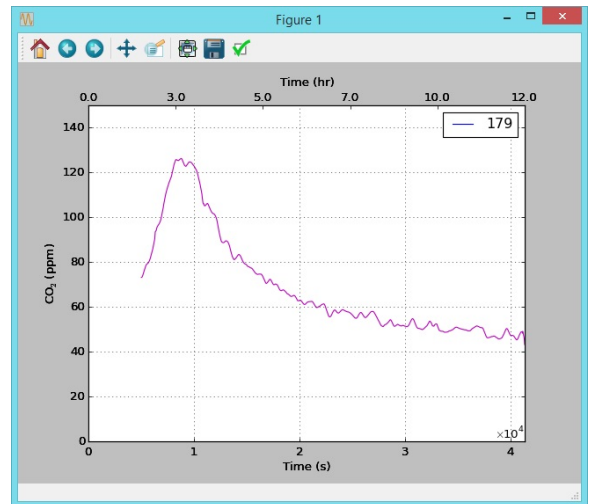
(a) Raw Data Sets



(b) Selected Raw Data



(c) Filtered Data



(d) Isolated Second Curve

Figure IV.23: CO₂ Curves from Raw Data Sets

IV.23.2 Segmenting the Curve

From Figure IV.23 (d), it is clear that the curve before reaching the peak is different from the curve that is declining after the peak. So the curve is further broken down into two segments to build the mathematical model.

IV.24 Mathematical Model Fitting

The mathematical model is constructed in two phases. In the first phase, the curve is separated into segments, and the model is fitted for each segment separately. Then from both model segments, they are connected again. This eliminates the initial high number of iterations in computing processes.

There are several types of model fitting methods. Among those, Multiple Linear Regression (MLR), polynomial regression, and nonlinear regression are popular. However, analysis of each separate model is not covered in this dissertation; instead, it focused on the final fitting model adapted to build the mathematical model of the photocatalytic system.

These curve fitting models are executed to find the optimal in a least squared-error. It is an iterative process that performs a nonlinear least squares fit of the model to the measured raw data. The baseline and interference are also observed in some of the experiments and are subtracted from the observed data to the fitting process if they exist. After the completion of each iteration of model fitting, a functional module tests the residual error to determine if any systematic error is present in the system. The residual error is the difference between the model and the new raw data. These errors indicate that the model being fitted requires next iterations if the model might generate a better fit. These iterations will continue until the preset threshold value of minimum error is obtained.

After it gives the tolerable residual error, the next step is to analyze the correlation between the raw measured data and fitted model data. The model fitting operation is repeated using the final results of the previous fit, which is discussed more in the next chapter. To find baseline and interferences, a python script is used, which is also discussed in more detail in the next chapter.

After this, minimizing the residual error and fitting are obtained. The next parameter to validate this estimated model is to analyze a single numeric variable called R-squared value (R^2 Value). R^2 value is calculated using a NumPy libraries.

IV.24.1 Modeling the First Segment of the Curve

First segment of the curve is modeled using the Linear/Quadratic Rational Model which is given by the equation:

$$y = f(x) = \frac{a + bx}{1 + cx + d(x^2)} \quad (\text{IV.6})$$

The Python script to calculate the R^2 -value is shown in Figure IV.24. This function returns the correlation coefficient matrix, P_{ij} and of the covariance matrix, C_i . The opti-

mization function call is as shown in Figure IV.25. This optimization fitting is based on the Levenberg-Marquardt algorithm through least square minimization of error. This algorithm determines the optimal parameters for each iteration step. This process converges much faster than the steepest descent method or robust Gaussian method.

$$P_{ij} = \frac{C_{ij}}{\sqrt{C_{ii} \times C_{jj}}} \quad (\text{IV.7})$$

```
import numpy as np
def CalculateR2(y, ycap):
    r2value = np.corrcoef(y, ycap)
    return r2value
```

Figure IV.24: Code Snippet to Calculate R² Value

```
1
2 from scipy.optimize import curve_fit
3 import numpy as np
4
5 #A Model function for First Segment of the Experimental Data
6 def modelfunc(x,a,b,c,d):
7     return (a*b+(c*(x**d)))/(b+(x*d))
8
9 def curvefitting(n):          # number of points for the Model
10    #Initialization of the Co-efficients and Model function
11    [a, b, c,d] = np.ones(4)
12    x = np.linspace(0, n-1, n)
13    y = modelfunc(x, a, b, c,d)
14
15    #Call to Curve Fitting Model
16    p, cov = curve_fit(modelfunc, x, y) #return optimal parameters, and estimated covariance
17    return [p,cov]
```

Figure IV.25: Code Snippet of Curve Fitting for First Segment

After optimization function call, it gives the co-efficients of the model:

$$a = 3.81028139470043E + 01 \quad (\text{IV.8})$$

$$b = -3.590162978441551E - 03 \quad (\text{IV.9})$$

$$c = -1.914079164031134E - 04 \quad (\text{IV.10})$$

$$d = 9.510001989619733E - 09 \quad (\text{IV.11})$$

$$(\text{IV.12})$$

Using this optimized model, the curve is produced, which is shown in Figure IV.26.

IV.24.2 Modeling the Second Segment of the Curve

The second segment of the curve follows the pattern of distribution curve. After analyzing several distribution curves, the Weibull distribution curve gives the best co-relation value.

$$y = f(x) = a - be^{-c(x^2)} \quad (\text{IV.13})$$

After optimizing the model, the co-efficients are found to be

$$a = 1.8195029015758E + 02 \quad (\text{IV.14})$$

$$b = 1.377567319779588E + 02 \quad (\text{IV.15})$$

$$c = 1.613955994354129E + 09 \quad (\text{IV.16})$$

$$d = -2.331313826647612E + 00 \quad (\text{IV.17})$$

$$(\text{IV.18})$$

after two separate segments are modeled. These two segments are connected again as shown in Figure IV.27.

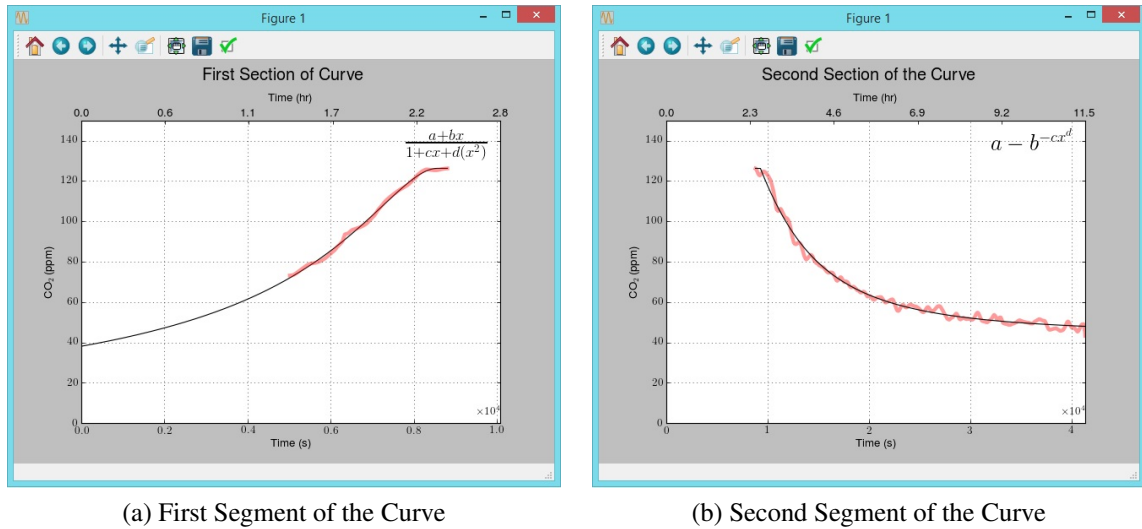


Figure IV.26: Mathematical Model of the Curves

Since the curves are connected, they are not smoothly transitioned. To smoothly connect the curve, the Wiener filter is applied, which gives the smooth transition of the curve at the connected sections of the curve.

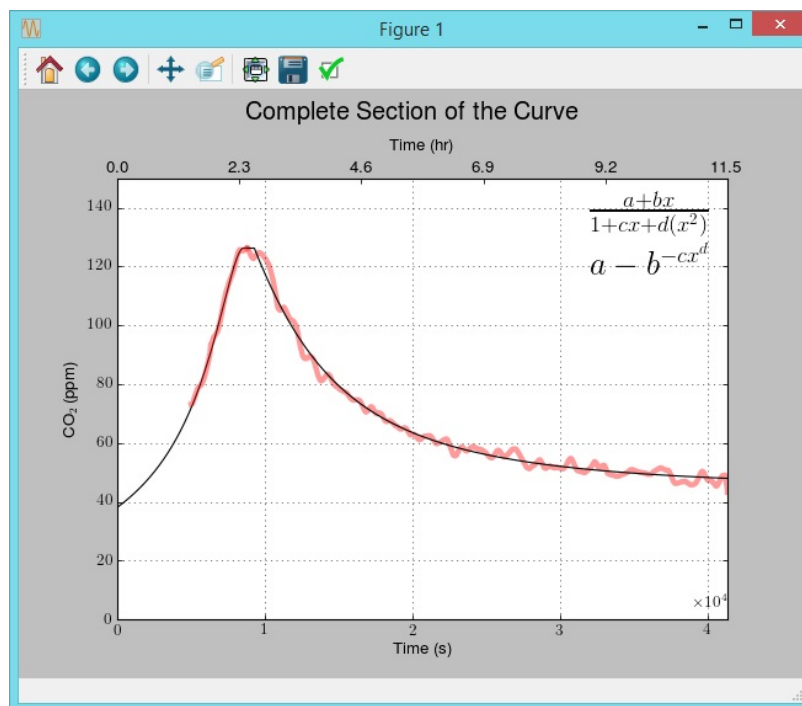


Figure IV.27: Connected Segments of the Modeled Curve

IV.25 Model Selection for CO₂ and VOC

Mathematical model fittings are used by using polynomial by polynomial rational model for both CO₂ and VOC data. However, there are other mathematical models; they are also tested. Among them chebyshev fittings for VOC and distribution curve fitting for CO₂ are evaluated. For the CO₂ curve, first rise of curve and fall of curve follows different distribution function. So among the best fitting curve, rational model is selected. A rational function model is a generalization of the polynomial model. Rational model has several features and flexibilities.

Some of the Advantage of Rational Model are[1]

- Rational function models have a moderately simple form.
- Rational function models are a closed family. As with polynomial models, this means that rational function models are not dependent on the underlying metric.
- Rational function models can take on an extremely wide range of shapes, accommodating a much wider range of shapes than does the polynomial family.

- Rational function models have better interpolatory properties than polynomial models. Rational functions are typically smoother and less oscillatory than polynomial models.
- Rational functions have excellent extrapolatory powers. Rational functions can typically be tailored to model the function not only within the domain of the data but also so as to be in agreement with theoretical/asymptotic behavior outside the domain of interest.
- Rational function models have excellent asymptotic properties. Rational functions can be either finite or infinite for finite values, or finite or infinite for infinite x values. Thus, rational functions can easily be incorporated into a rational function model.
- Rational function models can often be used to model complicated structure with a fairly low degree in both the numerator and denominator. This in turn means that fewer coefficients will be required compared to the polynomial model.
- Rational function models are moderately easy to handle computationally. Although they are nonlinear models, rational function models are a particularly easy nonlinear models to fit.

IV.25.1 CO₂ Model Fitting

From this completed two model based curve, a single model is formulated using the Polynomial by Polynomial Rational model.

$$y = f(x) = \frac{a + bx + cx^2 + dx^3 + ex^4 + fx^5}{1 + gx + hx^2 + ix^3 + jx^4 + kx^5 + lx^6} \quad (\text{IV.19})$$

$$a = 2.05556205e - 12$$

$$b = -4.02266307e + 05$$

$$c = 3.95210915e + 05$$

$$d = 1.46603897e + 04$$

$$e = -3.32822111e + 00$$

$$f = 2.38684721e - 04$$

$$g = -3.25407062e + 06$$

$$h = 4.01654265e + 06$$

$$i = -1.46558223e + 03$$

$$j = 2.39588044e - 01$$

$$k = -2.06460919e - 05$$

$$l = 7.98146285e - 10$$

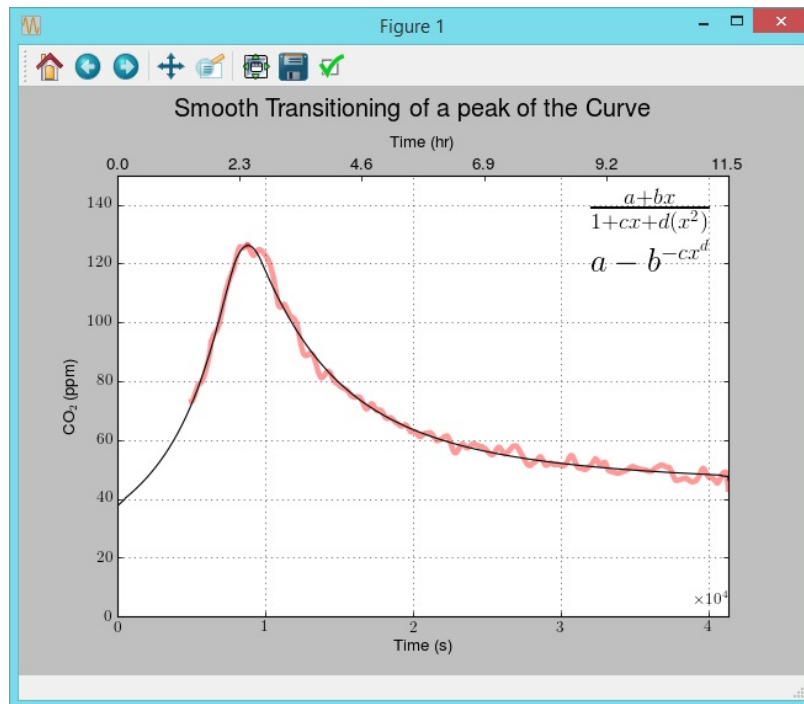


Figure IV.28: Smoothly Transitioned Curve

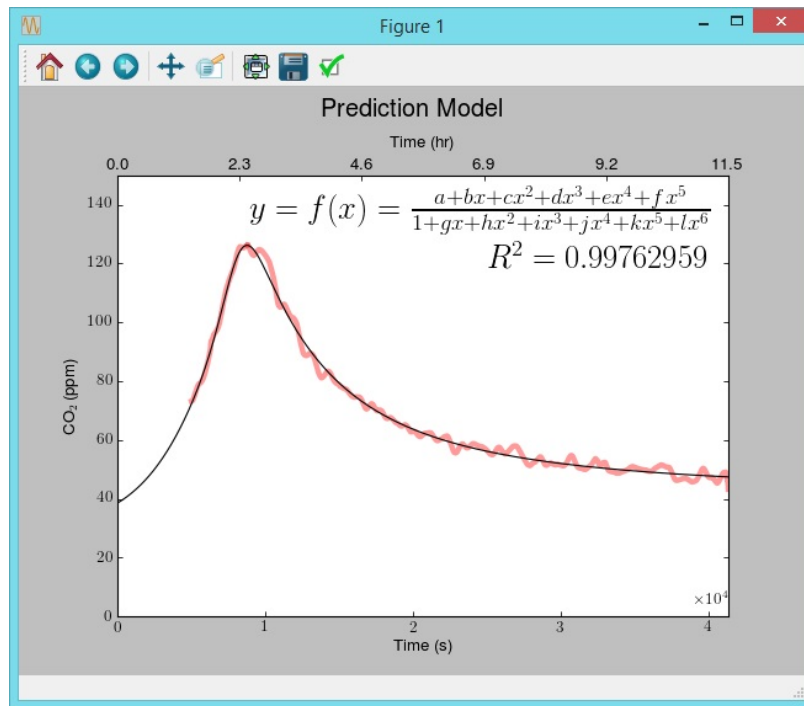
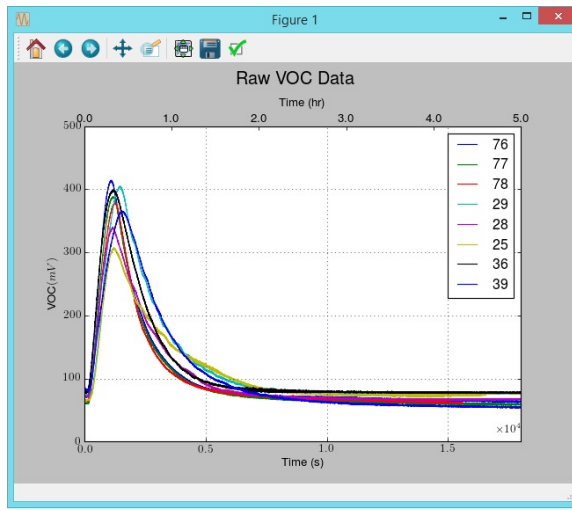


Figure IV.29: Mathematical Model of the Full Curve

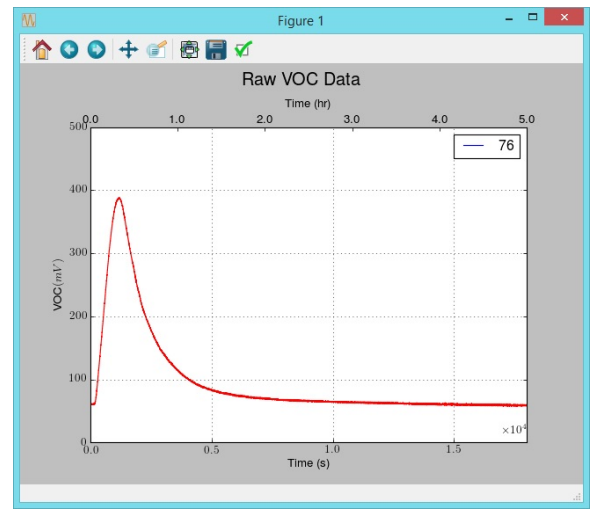
IV.25.2 VOC Model Fitting

VOC data is collected by the sensor array, which are recorded in the same raw file along with CO₂ data, relative humidity, and flow stream. VOC raw data are very smooth in comparison to CO₂ data. There were several experiments conducted at two sprays from the sensor under different humidity settings. Some of those VOC data are shown in the Figure IV.30. These VOC curves represent the total VOC amount introduced into the chamber by simulant.

VOC model curve is also obtained by using non-linear fitting method, polynomial by polynomial rational model as shown in the Figure V.10.



(a) VOC Experimental Data



(b) Selected VOC Curve for Modelling

Figure IV.30: Raw VOC Data Curves

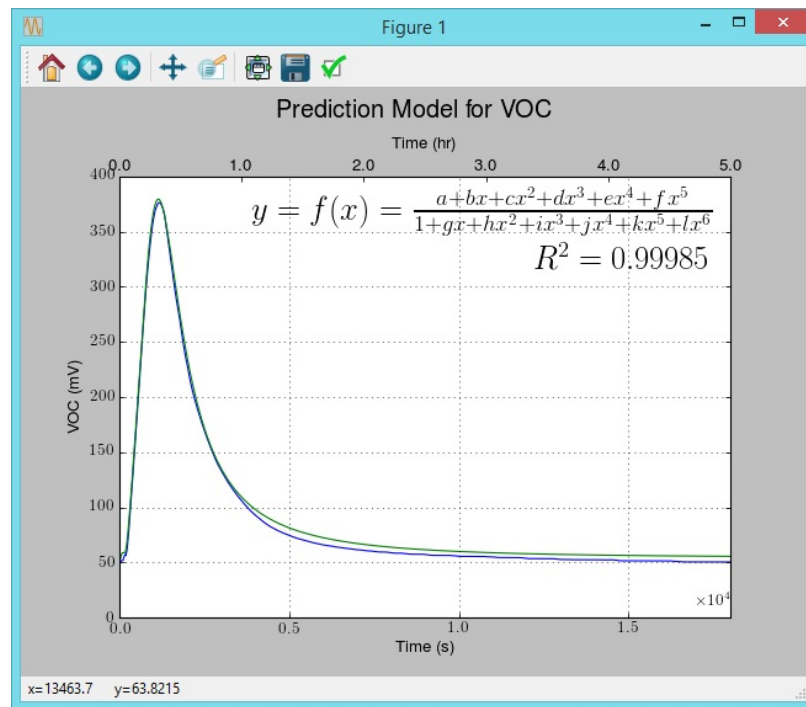


Figure IV.31: Mathematical Model of the VOC Curve

Chapter V

Data Analysis

V.1 Overview

This chapter discusses the various tools and techniques used to construct the mathematical model of the photocatalysis process that leads to prediction of photocatalytic characterization. It explains the use of scientific computing tools provided by SciPy and NumPy libraries for descriptive and exploratory analysis of data and for developing and extending techniques to build the mathematical model of the photocatalytic process.

V.2 Data Analysis

In the previous chapter, the several raw experimental data collections were performed. With the aid of graphical analysis, mathematical interpretation of data are presented for CO₂ and VOC individually. CO₂ data is decomposed into two sections. The raw data is collected over some pre-experiment without inducing the photocatalytic activity. The CO₂ and VOC data are collected. When photocatalytic activity is induced, the CO₂ curve is observed as second rise in the curve. By performing initial analysis of these two sections of the curve, these are decomposed into two portions. And an elaborate attempt is made to reconstruct the complete second portion of the curve into a mathematical model.

The mathematical model of the second portion of the curve needs to infer the validity of the underlying photocatalytic phenomena. To infer the validity of the experiments, the model is transferred into an experiment and comparative analysis performed. The validity of the model is estimated and the model is re-adjusted to fit the experimental sets. The experimental data underlying photocatalytic activity is sparse. For a large part of the model, an initial model is used, compared with other sets of experiments, and validated and adjusted.

To construct a mathematical model of high validity, several methods are used. One of the methods is to detect the offset values of CO₂ and VOC, which also removes the chance of calibration error of the sensor. A script is written to detect the offset of the experiment by moving it around to match with the mathematical model, which yields the lowest least square error value. The experimental data is electronically recorded into the computer system from an automated experimental apparatus. During the dispensing of the simulant

into the photochamber, it needs to open the chamber and electronically dispense the simulant and close again. This process is done in the computer process and there is a chance for delay of a few seconds delays in the user click event to execute the action of the chamber dispensing process. This results in either early recording of data or missing the data points. This problem is tackled with the software by aligning the curves so that the first curve declines from the same point. The advantages of this model are to the development of new experiments. These methods allow a faster refinement and correction of the model, while the choice of process implies a fundamental relevancy of the findings from this model. As the experimental data are sparse, they can be adjusted programatically so that they improves the model validity. This work aims at amplifying knowledge and understanding of the development of the process by critical evaluation of the visual analysis.

Mathematical models are the representation of the experimental data after pre-treatment of the raw experiments. Using appropriate methods and the right tools, almost every system can be modeled. The mathematical modeling is the formalization of the hypotheses and process of validating these hypothesis. The general data modeling process adopted in this research is as shown in Figure V.1. In the previous chapter, the initial mathematical model was constructed and estimated. The estimated model needs to be validated. Validation of the model is done by comparing the model with the experimental data. The comparison of the model is done by co-efficient of determination called r-squared value (R^2 Value).

V.2.1 Non-Linear Least Square Modeling

The non-linear least square method is adapted to obtain the best fitting of the curve between the model and raw measured data. It is a process of measurement of fitting the model and raw measured data by taking the sum of the squares of difference between the two signals. The squares of difference between the signal is then minimized using the optimization method. By using iterative changes of the values, the model parameters are obtained. The concept behind this is to obtain the single numeric descriptive variable from the two signal model and raw data, which can be mathematically expressed as below:

$$S = \sum_{i=1}^n \epsilon_i^2 \quad (V.1)$$

$$\epsilon_i = (Y_i - \hat{Y}_i) \quad (V.2)$$

Thus, the general method of least squares is a procedure which either explicitly determines or iteratively changes the values of the model parameters in order to minimize the sum of square residuals. In this application, the form of the model is nonlinear, so an iterative

method is required to determine the model parameters. The following sections will give additional detail on several key aspects of applying nonlinear least squares to the problem of fitting functions.

For statistical analysis, R^2 is used to explain how well the predicted values match with the experimental data. Its value lies between zero and one. One means an exact match and zero means there is no relation between predicted value and the experimental value. So the value closer to one is more desirable than the value further from one.

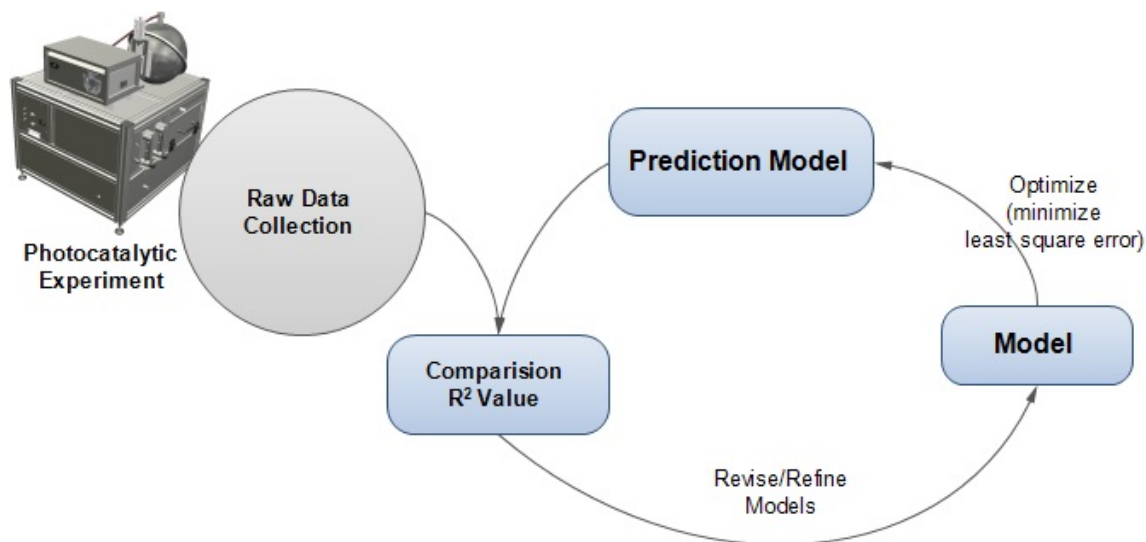


Figure V.1: Data Modeling Process

The model is compared with each experiment and the R^2 value is calculated. If R^2 is not satisfactory, the model is revised and re-modified until satisfactory results are obtained.

As the CO_2 curve is not linear, a non-linear regression model needs to be selected. Non-linear model fitting is a very common mathematical model; however, there are several non-linear models existed depending on the nature of the data that needs to be fitted. In most cases, the linear multiple regression or polynomial regression model is preferred.

V.3 Experiment Data Sets

There are several experimental data sets conducted in the main two different conditions: light and dark conditions. Experiments in dark conditions are used to set the baseline estimation and the sensor verifications. Then experiments in light conditions are conducted at three different concentrations. The concentration of the simulant is controlled by the sprayer. The mass of the simulant also depends on the in-line pressure supplied to the sprayer. Pressure

```

def modelfunc(x1,a, b, c,d,e,f,g,h,i,j,k,l):
    return (a+b*x1+c*(x1**2)+d*(x1**3)+e*(x1**4)+f*(x1**5))/(1+g*x1 +h*(x1**2)+i*(x1**3)+j*(x1**4)+k*(x1**5)+l*(x1**6))

def residualerror(xscale, yscale):
    #constraints for the Raw Data,checking if less than half hour data
    if len(dfco2)<1800:
        return
    peak1 =peakdet(dfco2,5)[0][0][0] # first peak of the CO2 Curve
    peak2 =peakdet(dfco2,5)[0][1][0] # second peak of the CO2 Curve
    miny = dfco2[peak1:peak2].min() # intersection point of the two Curves Y value
    intpoint = np.where(dfco2[peak1:peak2]==miny)[0][0] + peak1 # intersection point X value

    n = 50000 # number points selected for x axis
    ax = np.linspace(0,n-1,n*xscale)

    if (yscale<0): #constraint for z, it needs to be greater than 0
        return
    [a, b, c,d,e,f,g,h,i,j,k,l] = p #co-efficient from curve-fitting
    ay = modelfunc(ax, a, b, c,d,e,f,g,h,i,j,k,l) # predicted values of model
    ay = ay -ay[0] #bringing model down to 0 baseline
    xlen2 = len(ay)
    ay = ay * z # scaling factor of the curve peak for 0 baseline
    #Selecting the Length of Model same as the Raw Data
    xlen1 = len(dfco2) # size of the raw CO2 data
    xlen = np.array([xlen1,xlen2]).min()
    y1 = ay[:xlen]
    y1 = y1 - y1[0] #bringing down to 0 base line
    ycap = (dfco2[:xlen]-dfco2[1])
    ycap= ycap - ycap[0] #bringing down to 0 base line
    return sum((y1-ycap)**2)

```

Figure V.2: Code Snippet to Calculate the Least Square Error

of 20 psi is supplied to the sprayer in all the experiments. Based on this pressure setting, the mass is measured three times. The average value of the measurement is considered for the rest of the calculations.

Number of Sprays	Readings (Mass in mg)			Average (mg)
	1	2	3	
1	7.47	7.42	7.35	7.41
2	16.06	16.44	16.87	16.46
3	38.23	39.43	39.45	39.04

Table V.1: Number of Sprays and their Corresponding Mass

V.4 Time Delay Adjustment

Time delay adjustment (x-offset) is adjustment in the time scale. Time delay occurs when experiments are not recorded at the same exact time to make more comparisons between the experiments in the same experimental conditions. This section explains the time delay adjustment in five spray experiments. The same procedures are applicable for all experiments.

The set of experiments was conducted using five sprays at 50% Relative Humidity. The first set of experiments was compared with the mathematical model. Their R^2 value is listed in Table V.2. Based on this table, these experimental sets are closer to the model. There is some chance of time delay between the experiments when they are recorded by the software. This may cause some deviation within the model curve. This is adjusted by measuring time delay alignment (Table V.2). Based on the experiments conducted in the dark environment, the first peak of the curve of CO_2 occurs exactly at the same time. So they are aligned to the same time by adjusting these time delay alignment values. From Table V.2, the first peak occurs at almost the same time around 1100 seconds. Experiment 179 is started earlier than other experiments. So experiments 166 and 179 are shifted forward on the time scale by 72 and 11 seconds respectively, that they all start at the same exact time. However, time delay adjustment has little impact on the R^2 value of the model.

V.5 Base Line Detection and Adjustment

Base line is the measurement of the initial sensor reading. In the presence of noises in the signal, it is hard to estimate the base line value. For the calculation of area under the curve of the sensor data, it is required to have the base line value, which heavily impacts the area calculations. On other hand, it eliminates the y-scale or y-offset adjustment caused by calibration error in the sensors.

In preprocessing steps, the area under the curve of the experiments is roughly estimated. The base line is estimated by taking the weighted average of sensor readings until the curve ascends. Then this baseline value is used to calculate the area under the curve.

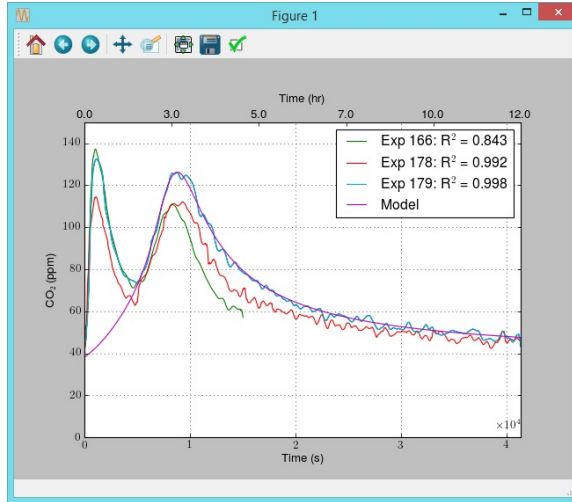
In Table V.3, baseline values are detected by moving the experimental data until it gives the least square of error with the model. From this table, these baseline values are slightly different. Although these differences about 11 are very small compared to the corresponding reading of 1100 on the scale, on a smaller scale it will have a bigger impact. Baseline detection is done to fine tune or refine the model curve to make it closer to the experimental curve. The curves after baseline adjustment are shown in Figure V.3.

Experiment ID	R ² Value	Time Delay Alignment
166	0.84270155	1057
178	0.99305581	1118
179	0.99762939	1129

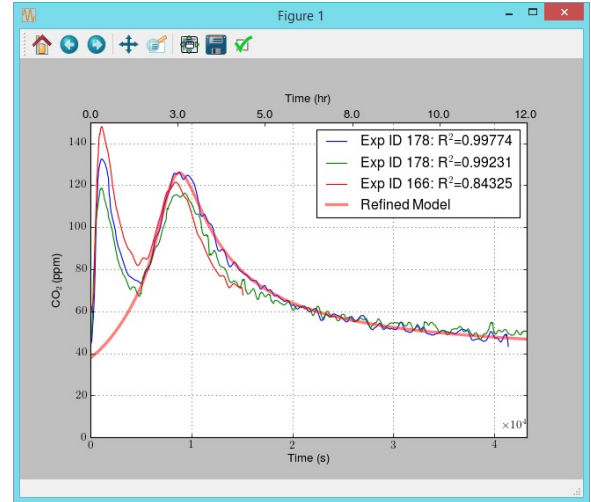
Table V.2: Initial Model and Coefficient of Determination for 5 Sprays at 50%RH

Experiment ID	R ² Value	Time Delay Alignment	Baseline Values	New R ² Value
166	0.8427016	1057	26.95434481	0.843246
178	0.9930558	1118	33.46858373	0.992307
179	0.9976294	1129	37.65347372	0.997734

Table V.3: Initial Model and Coefficient of Determination for 5 Sprays at 50%RH



(a) Initial Model and Raw Experiments of 5 Sprays at 50%RH



(b) Refined Model and Raw Experiments of 5 Sprays at 50%RH

Figure V.3: Refined Model and Raw Experiments of 5 Sprays at 50%RH

V.6 Estimation and Evaluation of the Model for Different Sprays Experiment

V.6.1 Initial Estimates

For any modeling methods, the most successful and precise estimation depends on the initial parameter values of the experiment. If initial estimates are heavily deviating from the real estimates, instead of converging to the solution, the optimization routine will diverge and execute the function loop infinitely. However, this can be controlled by defining the loop constraints by specifying the maximum number of iterations but still does not reach the solution. The only viable strategy to prevent this is to visually estimate the parameter and feed to the "Optimize" routine to get the closest possible value.

We generated the initial model from the 5-spray conditions. This model needs to be evaluated for 2-sprays and 1-spray for which experiments have been performed. So for different sprays, from visual inference, experiments are roughly detected as stretched in x direction and y direction. Here in this section, we analyze the curves of five sprays to the two sprays and one sprays by stretching the curves, which we called x value transformation and y value transformation.

The routine call can be optimized by minimizing the least square error by changing two factors, x-scale for x-axis transformation and y-scale for y-axis transformation. The model is analyzed with the experimental data of two sprays and one sprays. Before optimizing, the baseline of measured data is brought to zero reference. The base line values or y-offset values are detected by the baseline detection routine. There are several methods that exist, like the Fourier Series, Polynomial Fit, and Split Fit, for baseline detection. There are two approaches to detect the baseline estimation. One method can be accomplished by searching for the signal minimum within non-overlapping segments. These points are used to compute a linear least squares error. Here in this work, the baseline is detected by moving the y-values up and down until they yield least square error with the model. However, there is no role of baseline in the final ratio analysis of the CO₂ and VOC. So the effect of baseline detection error is eliminated. There is only some chance of baseline effect if there exists the effect of a chemical on the photocatalysis process, which would be another research interest. The objective of this procedure is to adjust the offset values to eliminate the calibration error of the sensors. This is done after the model is estimated and later based on these offset values, the model is redefined.

Owing to the fact the first peak of the time series measured data that occurs at the same exact time, the experiment is conducted. However, there is still a chance for a lag due to the user having to click the "Start Process" on the user interface. From Table V.4, there is a maximum difference of 88 seconds, about 1 minute. So in this process the first peak is

detected in the time scale and aligned with the other raw measured data.

However, there are several methods that exist to detect the peaks in time series. Here in this work, a peak is detected by using a sliding windows of certain width. In our experimental case, it is not tough to find the peaks. And window width in time scale is guessed from visual plotting. The maximum difference between the peaks is also specified and fed to the peak detection routine, which easily identifies the peaks in all the experimental data. Once the two peaks are detected, the minimum point is detected between the two peaks to find the intersection of two segments of the curves. From the intersection point of the raw data to total length the raw data is compared against the same length of the model.

V.7 Constraints for the Estimates

In several cases performing the modeling operation, it is required to add constraints to the model parameters. There are two types of constraints. One type of constraints is used during the optimization process. These constraints are devices for a model such that y-scale factor which cannot be zero because it needs to be zero only if there is no photocatalytic activity. The other constraints are in the final model because the photocatalytic reaction occur immediately after the exposure to simulant. The model still gives the predicted value over a very large time value in the time series, which needs to be rejected if they were below the baseline.

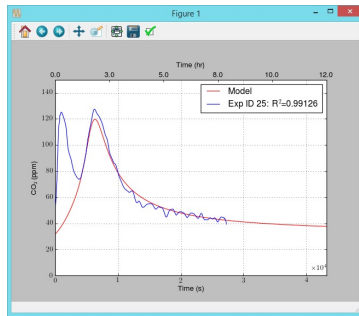
V.8 CO₂ Model for 2 Sprays

After the initial parameter is determined, the fitting of the model is done by a nonlinear least square minimization procedure. Based on the visual inference of the peak shapes, the x-axis transformation is applied. The x-axis transformation factor is calculated by minimizing the least square. After the x-axis transformation factor is applied to the model, the new R^2 values are calculated as shown in Table V.4. Based on this table, x-axis transformation is acceptable. In Figure V.4, each experiment was fitted to the model by optimizing the parameter. The x-axis transformation factor is taken by averaging the values from Table V.4. Since there exists a difference between baseline and time delay, and baseline equalization, time delay adjustments are applied. After these adjustments, the new R^2 value is calculated as shown in Figure V.5. The new R^2 value is slightly improved after these adjustments.

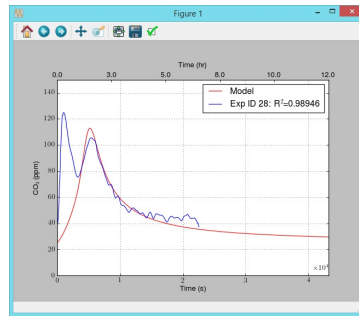
Experiment ID	R^2 Value	Time Delay Alignment	Baseline Values	x-axis Transformation Factor
---------------	-------------	----------------------	-----------------	------------------------------

25	0.99125841	968	31.5776	0.719748
29	0.98946178	1032	24.7386	0.593265
35	0.99355515	999	33.57413	0.747428

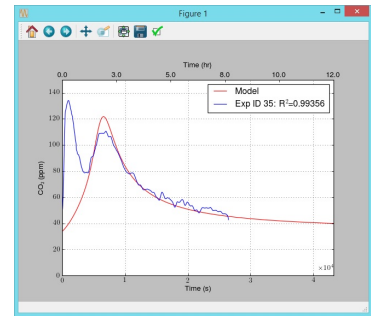
Table V.4: Estimation of X-scale Transformation for 2 Sprays at 50%RH



(a) ExpID 25 with Model

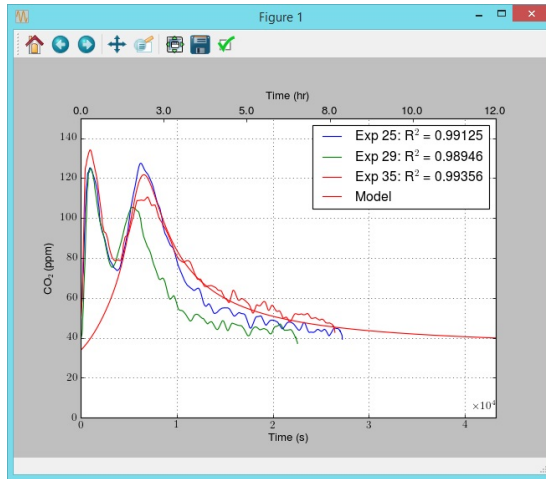


(b) ExpID 29 with Model

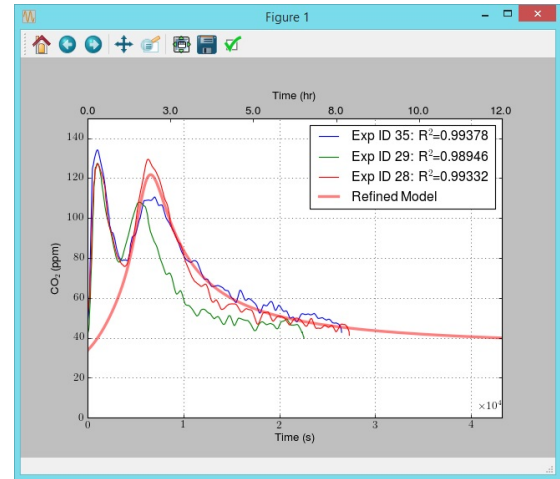


(c) ExpID 35 with Model

Figure V.4: Comparison of Model Raw Data of 2 Sprays at 50%RH



(a) Initial Model and Raw Experiments of 2 Sprays at 50%RH



(b) Refined Model and Raw Experiments of 2 Sprays at 50%RH

Figure V.5: Refined Model and Raw Experiments of 2 Sprays at 50%RH

V.9 CO₂ Model for 1 Spray at 50% Relative Humidity

The x-axis transformation is also applied for 1 spray. It is calculated by minimizing the least square. After the x-axis transformation factor is applied to the model, the new R^2 values are calculated as shown in Table V.5. Based on this table, the x-axis transformation is in acceptable range. In Figure V.4, each experiment was fitted to the model by optimizing the parameter. The x-axis transformation factor is taken by averaging the values from Table V.5. Since there exists a difference between baseline and time delay, and baseline equalization, time delay adjustments are applied. After these adjustments, the new R^2 value is calculated as shown in Figure V.7. The new R^2 value is slightly improved after these adjustments.

Experiment ID	R^2 Value	Time Delay Alignment	Baseline Values	x Transformation Scale
43	0.97619343	1057	42.4804	0.566912
59	0.94546228	1118	41.9357	0.472486
63	0.95746208	1129	48.9383	0.492714

Table V.5: Estimation of X-scale Transformation for 1 Sprays at 50%RH

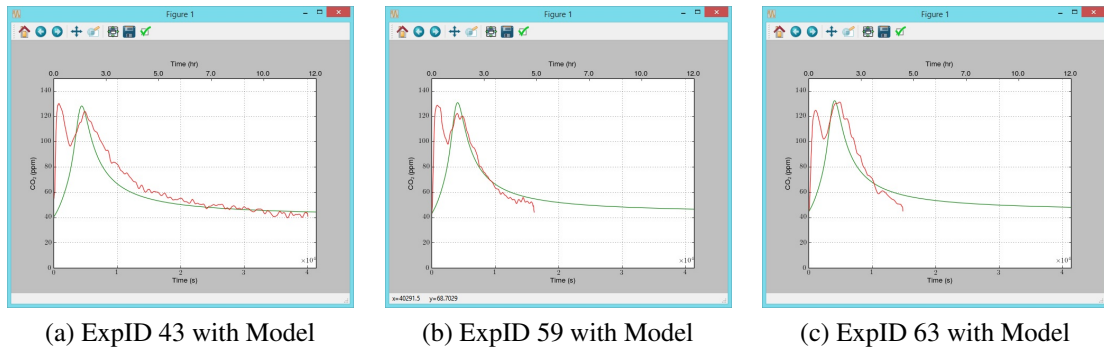
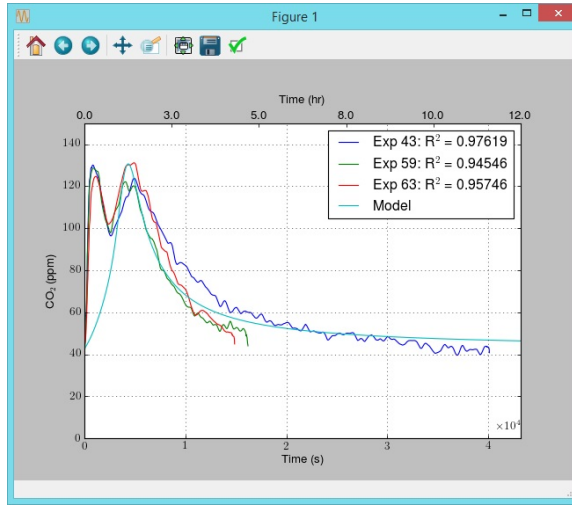
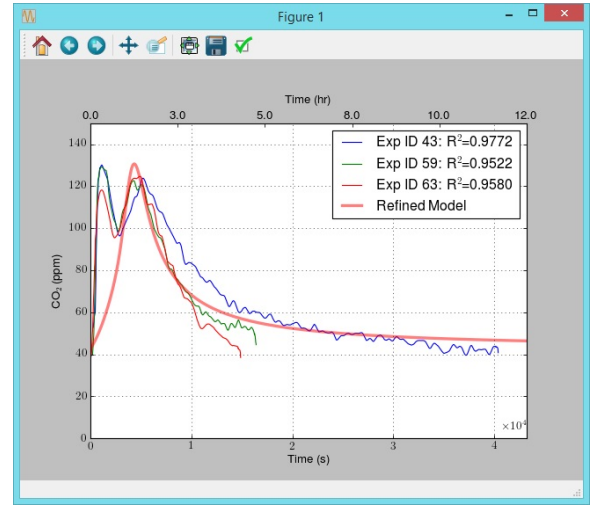


Figure V.6: Comparison of Model Raw Data at 1 Sprays at 50% RH



(a) Initial Model and Raw Experiments of 1 Sprays at 50%RH



(b) Refined Model and Raw Experiments of 1 Sprays at 50%RH

Figure V.7: Refined Model and Raw Experiments of 1 Sprays at 50%RH

V.10 CO₂ Model for 2 Sprays at 30% Relative Humidity

Relative humidity is changed from 30% to 50% in this set of experiments. By visual inference, it can be seen that the CO₂ curve peak rises more. So an attempt has been made to compare with the model by transforming the y-scale by optimizing the least square as in the previous section. From Table V.6, the model is very much closer to the experimental data as reflected by the R^2 value. Since there exists a difference between baseline and time delay, baseline equalization and time delay adjustment are applied. After these adjustments, the y-scale transformation factor is re-calculated, which is shown in Table V.6.

Experiment ID	R^2 Value	Baseline Vales	y-axis Transformation Factor	y Transformation Scale Adjusted
76	0.9743077828	43.0998	1.273079	1.26966
77	0.9473205255	56.5344	1.067848	1.11441
78	0.9359911815	33.0234	1.271378	1.22355

Table V.6: Estimation of Y-scale Transformation, Y-scale Transformation after Baseline and Time Delay Adjustment for 2 Sprays at 30%RH

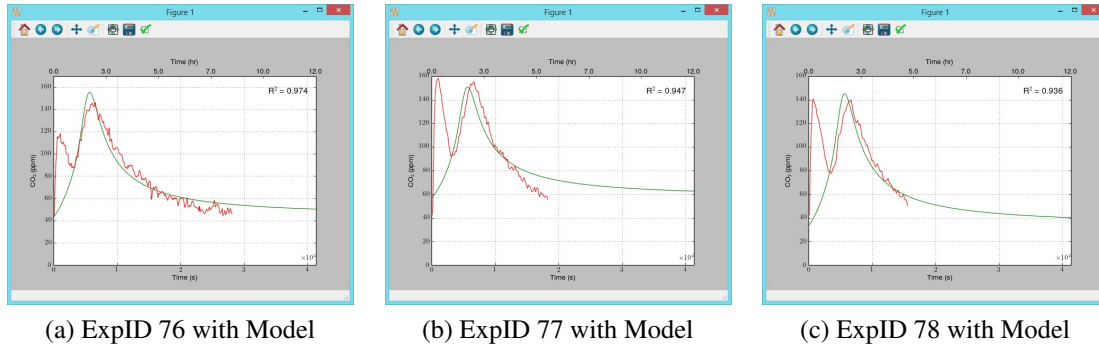


Figure V.8: Comparison of Model Raw Data for 2 Spray at 30 % Relative Humidity

V.11 CO₂ Model for 2 Sprays at 70% Relative Humidity

In this experiment set, relative humidity is changed to 70%. By visual inference, it is determined that the CO₂ curve peak rises less than at 50%. So y-scale transformation is made by optimizing the least square as in the previous sections. From Table V.7, the model is very much closer to the experimental data as reflected by the R² value. Since there is a slight difference between baseline and time delay, baseline equalization and time delay adjustments are applied. After these adjustments, the y-scale transformation factor is re-calculated, which is shown in Table V.7.

Experiment ID	R ² Value	Baseline Vales	y Transfor- mation Scale	y Transformation Scale Adjusted
84	0.9048243032	43.0753	0.753594	0.733
88	0.9387016491	47.1136	0.735	0.702
89	0.8773965590	42.7616	0.7	0.757

Table V.7: Estimation of Y-scale Transformation, Y-scale Transformation after Baseline and Time Delay Adjustment for 2 Sprays at 70%RH

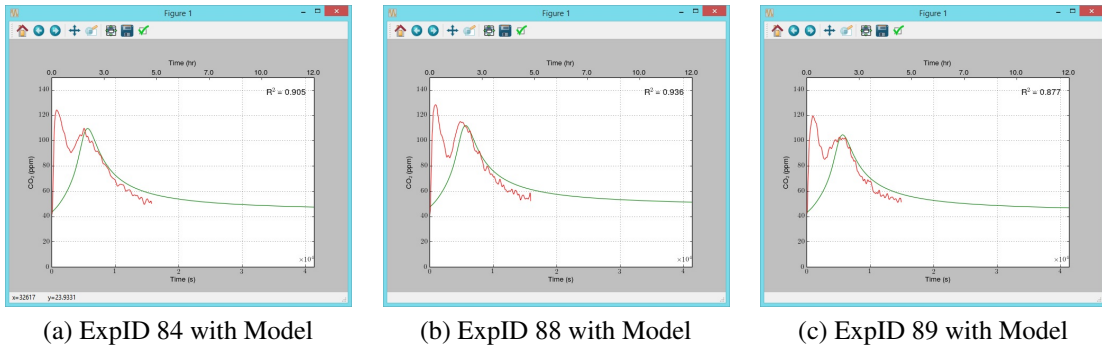


Figure V.9: Comparison of Model and Raw Data for 2 Sprays at 70% Relative Humidity

V.12 VOC Modeling

For VOC, the fitting of the model is also done by nonlinear least square minimization procedure. Based on the visual inference of the peak shapes, y-axis transformation is applied. The y-axis transformation factor is calculated by minimizing the least square. Since there are several experiments conducted at 2-sprays, 2-sprays is considered as the base model. The R^2 value of 2-sprays at 30%, 50%, and 70% are shown in Tables V.8, V.9, and V.10. Based on R^2 value, the experimental data is closer to the model. However, there are slight differences in baseline values and time delays. Time delay adjustment and baseline adjustment are applied to obtain the optimized y-scale transformation factor, and the model is refined based on these values. The y-axis transformation factor is calculated for 1 and 5 sprays are calculated. This y-axis transformation factor is shown in Table V.12 and V.13. By applying the y-scale transformation, VOC models for 1, 2, and 5 sprays are constructed and compared with the raw experimental data of VOC, which is shown in Figure V.10.

Experiment ID	R^2 Value	Time Delay Alignment	Baseline Values
76	0.999849866	1098	59.96704
77	0.997893528	1173	53.87878
78	0.997894251	1262	53.92456

Table V.8: Time Delay Alignment Values and Baseline Values for VOC for 2 Sprays 30%RH

Experiment ID	R² Value	Time Delay Alignment	Baseline Values
25	0.978879327	1098	45.22705
28	0.990561023	1173	29.57153
29	0.997894251	1262	45.45593

Table V.9: Time Delay Alignment Values and Baseline Values for VOC for 2 Sprays at 50%RH

Experiment ID	R² Value	Time Delay Alignment	Baseline Values
87	0.945753776	1098	44.08264
88	0.968051585	1173	45.3186
89	0.985602594	1262	59.41772

Table V.10: Time Delay Alignment Values and Baseline Values for VOC for 2 Sprays at 70%RH

Experiment ID	R² Value	Time Delay Alignment	Baseline Values	y Transformation Scale
87	0.954063854	1098	7.23267	0.84023437
88	0.990561023	1173	6.5918	0.83896484
89	0.997894251	1262	0.8697	1.03623047

Table V.11: Estimation of Y-scale Transformation after Baseline and Time Delay Adjustment for 2 Sprays at 70% Relative Humidity

Experiment ID	R² Value	Time Delay Alignment	Baseline Values	y Transformation Scale
----------------------	----------------------------	-----------------------------	------------------------	-------------------------------

166	0.984896100	1098	7.32422	3.89697266
178	0.901417813	1173	29.38843	4.49033203
179	0.968623172	1262	29.57153	5.10644531

Table V.12: Estimation of Y-scale Transformation after Baseline and Time Delay Adjustment for 5 Sprays at 50% Relative Humidity

Experiment ID	R² Value	Time Delay Alignment	Baseline Values	y Transformation Scale
59	0.995781489	1098	2.88391	0.39667969
63	0.973896761	1173	0.82397	0.44169922

Table V.13: Estimation of Y-scale Transformation after Baseline and Time Delay Adjustment for 1 Sprays at 50% Relative Humidity

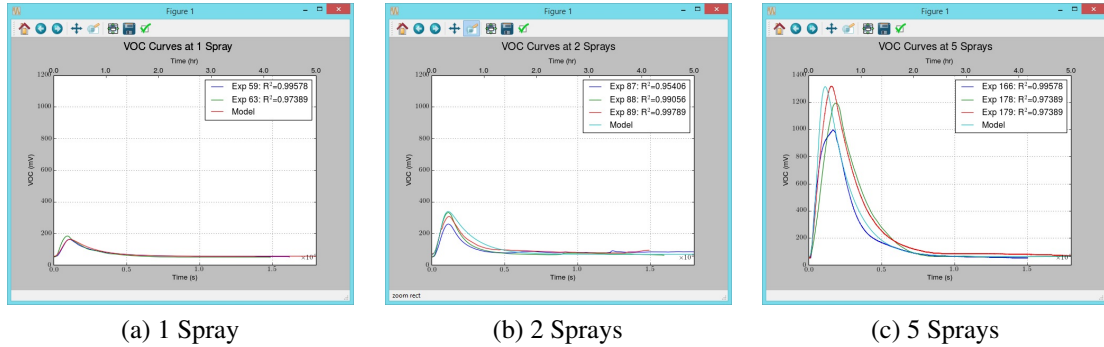


Figure V.10: VOC Curves and VOC Model at 1,2, and 5 Sprays

V.13 Mathematical Model for the CO₂ and VOC

After a series of procedures, a final mathematical model is constructed. The CO₂ model is given by Equation V.3 and the VOC model is given by Equation V.8. The co-efficients of function $f(x)$ are the optimized results of the preprocessing of CO₂ and VOC curves. The mass factors are calculated by the polynomial fitting of the three mass taken at one, two and five sprays (Table V.7). The humidity factors are also calculated from the polynomial fitting of the three humidity values, 30%, 50% and 70%. The mass factors for CO₂ and VOC are independently calculated so the mass factor for CO₂ can not be used in VOC. The co-efficients of each equation are given below. Using these mathematical models, all the experiments can be reproduced. New experiments can be predicted by these mathematical models.

CO₂ Model is given by

$$y = y_o + rhF \times f(x) \quad (V.3)$$

Where y is the CO₂ level in ppm.

y_o = Initial value of CO₂ Reading

t = time in seconds

mF = Mass Factor

rhF = Humidity Factor

$$f(x) = \frac{a + bx + cx^2 + dx^3 + ex^4 + fx^5}{1 + gx + hx^2 + ix^3 + jx^4 + kx^5 + lx^6} \quad (V.4)$$

Where

$a =$	2.05556205e-12	$g =$	-3.25407062e+06
$b =$	-4.02266307e+05	$h =$	4.01654265e+06
$c =$	3.95210915e+05	$i =$	-1.46558223e+03
$d =$	1.46603897e+04	$j =$	2.39588044e-01
$e =$	-3.32822111e+00	$k =$	-2.06460919e-05
$f =$	2.3868472e-04	$l =$	7.98146285e-10

$$x = t/mF \quad (V.5)$$

Where mF is given by

$$nsF = a + b.M + c.M^2 + d.M^3 \quad (V.6)$$

where M is the mass of Sprays

$$\begin{aligned} a &= 7.66566140e-05, \\ b &= -4.92632329e-03, \\ c &= 1.01104414e-01, \\ d &= 1.11022302e-15 \end{aligned}$$

Where rhF is given by

$$sF = a + b.RH + c.RH^2 + d.RH^3 \quad (V.7)$$

where RH is the Relative Humidity

$$\begin{aligned} a &= -2.44249065e-15, \\ b &= 8.95535714e-02, \\ c &= -2.04285714e-03, \\ d &= 1.30357143e-05 \end{aligned}$$

VOC Model is given by

$$y = y_o + mF \times f(x) \quad (V.8)$$

Where y is the VOC level in millivolts (mV).

y_o = Initial value of VOC Reading

t = time in seconds

mF = Mass Factor

$$f(x) = \frac{a + bx + cx^2 + dx^3 + ex^4 + fx^5}{1 + gx + hx^2 + ix^3 + jx^4 + kx^5 + lx^6} \quad (V.9)$$

Where

$$\begin{aligned} a &= -5.07250445e-03 & g &= 8.23852704e-04 \\ b &= 6.42181321e-05 & h &= 6.35657408e-05 \\ c &= -1.59232229e-06 & i &= -1.02822938e-07 \\ d &= 1.01064074e-08 & j &= 9.00980021e-11 \\ e &= 5.51012156e-13 & k &= -2.14447961e-14 \\ f &= -2.31932521e-16 & l &= 3.85182402e-18 \end{aligned}$$

$$f(x) = f(t) \quad (\text{V.10})$$

Where mF is given by

$$mF = a + b.M + c.M^2 + d.M^3 \quad (\text{V.11})$$

where M is the mass of Sprays

$$a = 3.55328306\text{e-}05,$$

$$b = 2.87836292\text{e-}04,$$

$$c = 4.98729100\text{e-}02,$$

$$d = 3.05311332\text{e-}16$$

V.14 Analysis of Mathematical Models

Mathematical models for both CO_2 and VOC are built in the previous sections. For graphical analysis, the experimental data curves are plotted as shown in Figure V.12. The results from the mathematical models are shown in Figure V.11. In these figures, curves are represented by the number of sprays instead of mass. This number of sprays can be mapped to the mass; however, the mathematical model takes the mass as an input. As in the mathematical model, the CO_2 curves are decomposed into two representing the first curve occurred during spray of simulant by the opening of the chamber, and the second curve occurred due to the photocatalytic activity inside the sealed chamber. So the CO_2 curve is the composite of two overlapping curves. They are represented as first CO_2 as shown in Figure V.12.

Area ratios are used to analyze the photocatalytic process. The area under the curve is calculated by using the trapezoid method. The two parameters of interest in this research work are relative humidity and mass of the simulant. So experiments are conducted at different relative humidity and different mass, keeping all other parameters constant. If these parameters are changed, the quantity of byproduct of the photocatalytic process, CO_2 , also changes. These changes are evaluated by the total area produced by the CO_2 and VOC from the baseline.

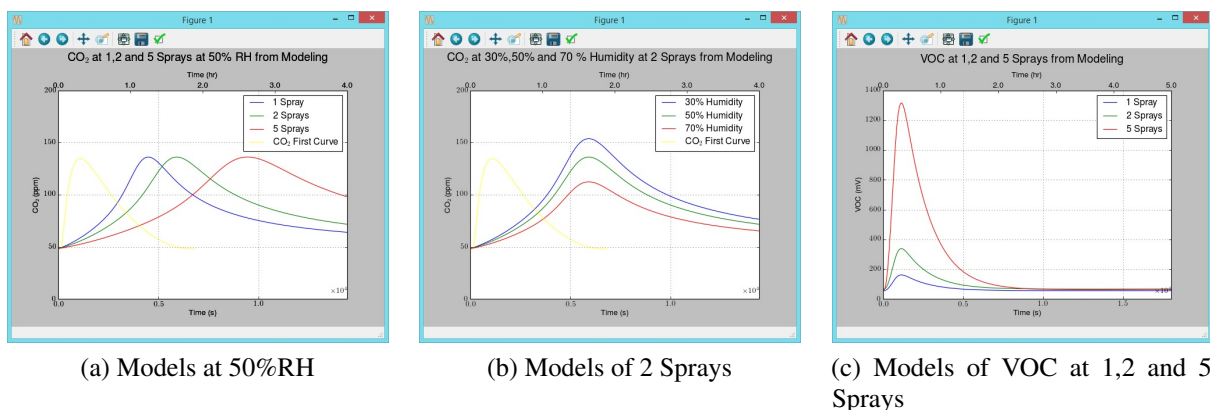


Figure V.11: CO_2 and VOC Models at 1,2 and 3 Sprays at 50% RH; 2 Sprays at 30%,50% and 70% RH

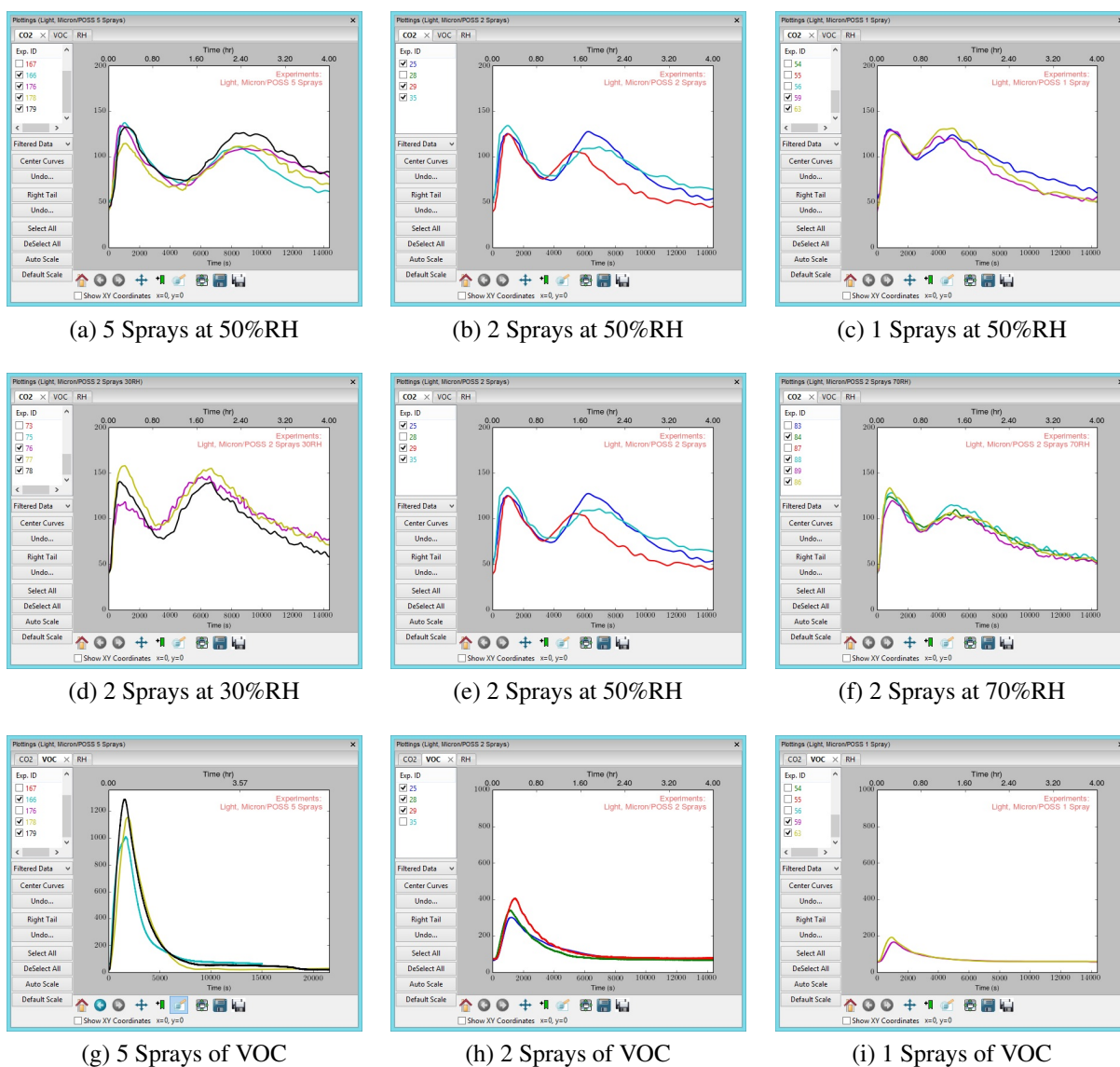
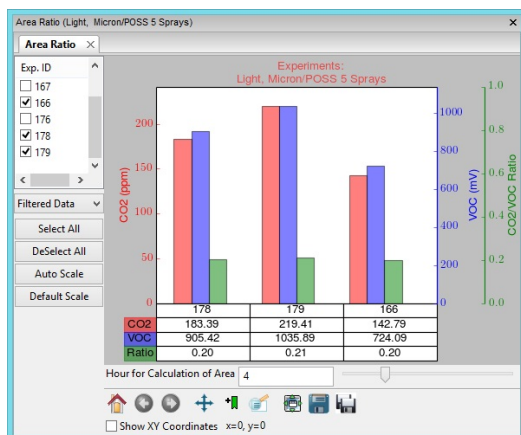
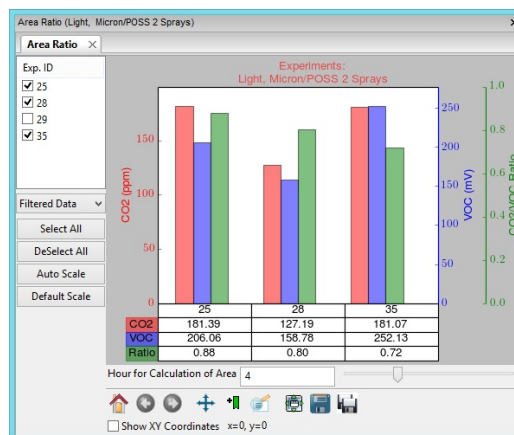


Figure V.12: Experimental CO₂ Curves of 1, 2 and 3 Sprays at 50 %RH; Curves of 2 Sprays at 30%, 50% and 70%RH; Experimental VOC Curves of 5,2 and 1 Sprays

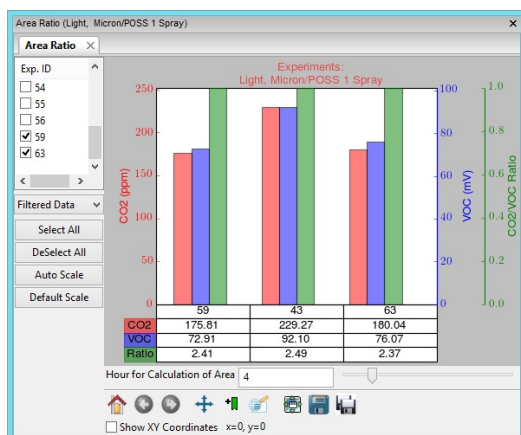
From the raw experimental data, area ratio is estimated, which is shown in Figure V.13. These area ratios are calculated by taking the area under the curve at four hours. From the mathematical modeling, total area under the curve is calculated. From this area, area ratio is calculated, which is shown in Table V.14. The results say an increase in humidity decreases the area ratio, which means a decrease in CO₂ production or less photocatalytic activity. Less humidity results in higher area ratio, meaning more CO₂ or more photocatalytic activities. If the simulant mass increases, the area ratio decreases. So the catalyst can degrade the lower



(a) Area Ratio of 5 Sprays at 50%RH



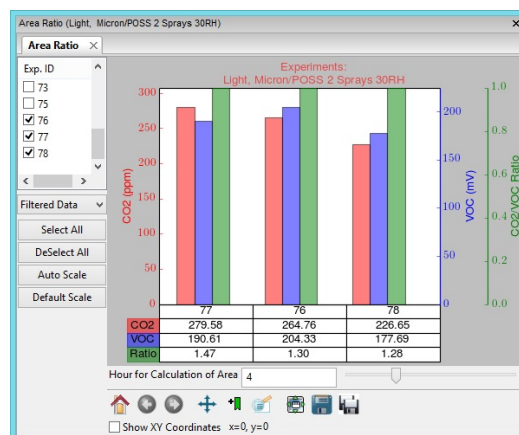
(b) Area Ratio of 2 Sprays at 50%RH



(c) Area Ratio of 1 Spray at 50%RH



(d) Area Ratio of 2 Sprays at 70%RH



(e) Area Ratio of 2 Sprays at 30%RH

Figure V.13: Estimation of Analytical Solution of Area Ratios of CO₂ and VOC

quantity of VOC at a higher rate and less humidity also increases the rate of reaction.

	5 Sprays @50% RH	2 Sprays @50% RH	1 Sprays @50% RH	2 Sprays @70% RH	2 Sprays @30% RH
CO₂	158.55	140.74	119.93	102.75	168.89
VOC	770.73	171.26	68.5	171.26	171.26
Ratio	0.21	0.82	1.75	0.60	0.99

Table V.14: Ratio of CO₂ and VOC calculated from Models

Chapter VI

Summary and Conclusion

VI.1 Conclusion

The overall purpose of this dissertation is to characterize the experimental photocatalytic data into the mathematical model. With the research outcome of this dissertation work, the mathematical model of the photocatalytic activity will add contributions to the field of computational, quantitative, graphical analysis, and photocatalytic activities. The mathematical model that leads to prediction and the raw measured data have demonstrated improved processing capabilities for different ranges of spray quantities of the simulant and different ranges of the relative humidity. Several significant software systems have been developed and tested. Finally, the effort of investigation of this research work has put forward a new approach to analyze the photocatalytic activities, which could build the foundation laid by this work area.

VI.2 Summary

The major purpose of this dissertation was to construct the best mathematical representation of the photocatalytic model that can reproduce all the raw measured data, and based on this raw measured data, to generate and to predict new data sets. The next purpose was to provide a better understanding of the interpretation of the mathematical model. All of the intermediate processing of the analysis that was required to build the final mathematical model are discussed in this dissertation.

A complete system of a fully integrated, automated and instrumented system into an existing photo reactor was designed to conduct several series of photocatalytic process. With various quantities of specific simulant of interest at different relative humidity settings, photocatalytic experiments were conducted. The system level control and communication software necessary for the automatic system of the photoreactor and recording the raw sensor data into a standard data files has been developed and implemented in a LabVIEW environment. This system uses industry standard communication, and serial USB communication protocols to communicate with the hardware system that are embedded in the photoreactor. These raw measured data files are then fed into the fully developed system,

a user interface based on Python programming languages with wxPython libraries. This software enables an off-line analysis of raw measured data including the necessary standard preprocessing procedures. The software provides all the required computational modules, data handling, and data management. By using this off-line analysis system, a mathematical model is generated, which will reproduce the experiments at various quantities of simulant and at different relative humidity systems.

A suite of preprocessing procedures has been implemented to facilitate an extraction of the information from the raw measured data. In the first step of preprocessing, data is trimmed, which is collected during an extended period of the experiment. In the next step, based on the noise level, a filter is applied to remove unusual noise. Based on the preprocessed raw data, a best fit initial mathematical model is constructed, which is refined and reprocessed to construct the final mathematical model. A baseline is estimated by using a baseline detection method and then the y-scale (weight) parameter and x-scale are optimized using non-linear least square error minimization, which are used to mathematical the various quantities of the simulant and the relative humidity settings.

The mathematical model is then evaluated with the ratio analysis done by using analytical methods for the conducted experiments. With an aim to reproduce all of the conducted experiments, they were conducted and validated with the new series of experiments.

VI.3 Contributions

Several contributions are made to the field of application of computational tools and methods applied to photocatalytic characterization by this research. It is a kind of first continuous measurement of parameter of interest (quantity of simulant, relative humidity) in photocatalytic activity. It is an approach to characterize the photocatalytic process using a ratio of CO₂ and VOC. In addition, it uses polynomial by polynomial rational modeling to represent experiments and effect of the parameter of interest. With this approach, an entire data set is modeled and refined by decomposing CO₂ introduced by the opening of the chamber and by the photocatalytic process. The mathematical model contributes to the different settings of quantity and relative humidity. The computational methods used in this research resulted in the most effective approach to modeling the nonlinear curves.

In the course of this research work, several software modules were generated, which can operate as standalone or be made executable. The major software components are the control and communication software written in LabVIEW, the off-line tool for data handling, preprocessing, computations, graphical user interface, GUI written in platform independent programming language Python. This software provides a convenient interactive

user interface and portability.

VI.4 Limitations of the Research

However, the existing experimental setup is designed to perform best at a given setup, it has certain limitations as well, which are listed below.

- i. Due to the toxicity of the simulant, experiments are not conducted at a higher amount.
- ii. Since the experiments are conducted in very harsh conditions, sensors were not able to withstand these situations.
- iii. Since the VOC sensors are verified for a certain family of VOC content, its readings cannot be directly mapped to ppm values.
- iv. All the experiments are conducted at constant air flow stream and light source.

VI.5 Future Research

Several potential new research issues have become apparent in the process of this dissertation work, both for computational scientists and photochemists. In this dissertation work, parameters of interest are quantity of the simulant and relative humidity. But there are several other parameters that can be considered like initial simulant, concentration, temperature, air flow streams, and light source, which requires refining the mathematical model that leads to prediction model.

Some of the experiments can only be identified by experiments not using this mathematical model. For example, the model can predict beyond 100% humidity but this is false. We don't know at which point photocatalytic process begins different pattern like at 90%, 99%, etc. This can be performed on this designed experimental setup, using the designed software and same deliverables and consumables.

Appendix A

List of Sensors and its Specifications

piD-TECH™

Plug-In Photoionization Sensor

Baseline - **MOCON**, Inc.™

SENSOR

The "piD-TECH™" Plug-In Photoionization Sensor is designed to be installed in portable and stationary gas monitors that accept City Technology™ - 4P cells. It provides complete photoionization detection capability in a package that has the same dimensional and electrical profile as these cells.

This gives many gas monitors new and powerful detection capability that was previously unavailable. It opens up an incredible variety of environmental and safety applications in industrial, commercial and residential markets.

The piD-TECH™ sensor is offered in two models. They are virtually insensitive to humidity changes, providing unparalleled performance in a variety of applications.



The piD-TECH™ Black Label has a linear dynamic range of 0.1ppm to 2,000ppm.

The piD-TECH™ Silver Label has a linear dynamic range of <0.01ppm to 20ppm.

The sensor is based on a photoionization detector (PID). The sample gas is exposed to an ultraviolet light from a lamp. The light emitted by the lamp ionizes the targeted gases in the sample so they can be detected by the instrument and reported as a concentration. Chemicals such as VOCs with an ionization potential <10.6 eV will be detected by photoionization. Contact Baseline for a comprehensive ionization potential list.

Applications

- Industrial hygiene & safety monitoring
- Soil contamination and remediation
- Hazmat sites and spills
- Low concentration leak detection
- EPA Method 21 and emissions monitoring
- Arson investigation

Features

- City Technology™ - 4P cell platform compatible
- Complete Sensor including:
 - Detector Cell
 - Photoionization Detector Lamp
 - Lamp Driver
 - Amplifier
 - Sample Filter
- Lamp energy = 10.6 eV
- Intrinsically Safe

Baseline, the reference point from which all things are measured.

Information in Baseline - MOCON, Inc. Product Literature is accurate at the time of release. However, product specifications and availability, promotions, prices, relationships, contact numbers and other specific information may change over time. Visit <http://www.baselineindustries.com> for additional information and the latest product literature.

piD-TECH® *plus* Photoionization Sensor Data Sheet

Performance Characteristics

Target Gases: VOCs and other gases with Ionization Potential ≤ 10.6 eV

Lamp Energy: 10.6 eV

Linear Range: 0 - 2000 ppm Isobutylene, Accuracy at 2000ppm is %20 with calibration point at 100ppm.

Minimum Detectable Quantity: 0.1 ppm Isobutylene

T₉₀ Response Time: ≤ 20 seconds (diffusion mode)

Temperature Range: -20 °C to 40 °C (Maximum temperature is 60 °C).

Temperature Dependence: Maximum deviation from the average temperature dependence curve is less than %20.

Relative Humidity Range: 0 to 90% non-condensing

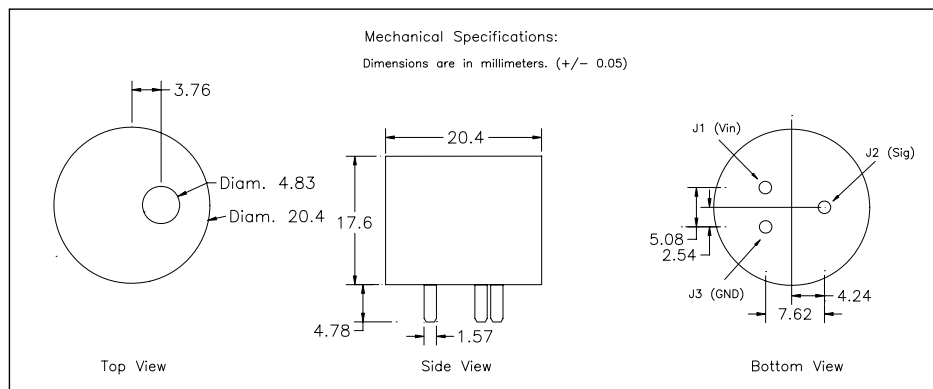
Humidity Response: < 1ppm @ 90% r.h., 25 °C, with zero gas applied.

Humidity Effect: Reduction of response to Isobutylene @ 90% r.h. < 15% of response @ 0% r.h.

Onboard Filter: To remove liquids/ particles

Operating Life: > 1 year

Storage Life: > 2 year



Baseline-MOCON, Inc.

19661 HWY 36
Lyons, CO 80540
PH 303-823-6661

piD-TECH® *plus*
- Data Sheet

DWG No. 7400-0105-011

Rev. C

Part No. ZPP6018001

Sheet 1 of 2

Electrical Characteristics

Supply Voltage(J1): 3.2V – 10V

Current: 20mA - 30mA

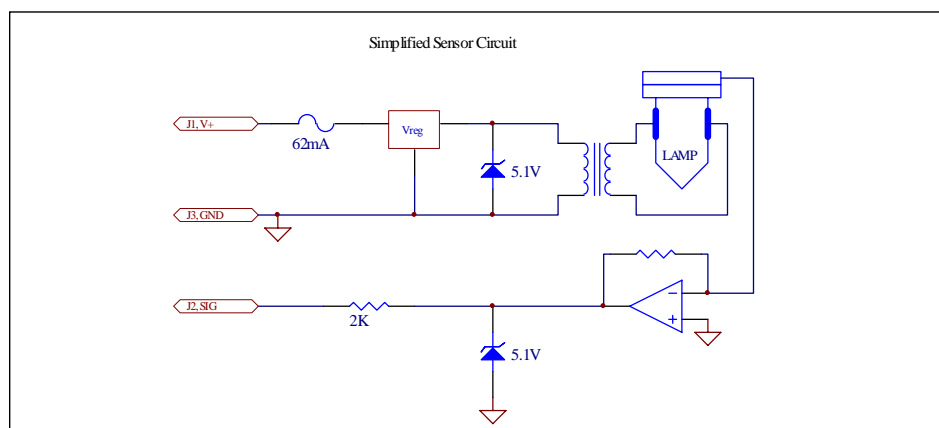
Power Consumption: 64mW - 300mW, Dependent on supply voltage.

Output Signal(J2): 0.05V - 2V (Maximum Voltage = 2.85V)

0ppm: 0.05V – 0.06V

100ppm (Isobutylene): 0.09V – 0.167V (.4mV/ppm - 1.07mV/ppm)

2000ppm (Isobutylene): 0.68V – 2V, (Based on non-linearity of –10% @ 2000ppm)



Conditions for safe use:

- The sensor shall be installed inside of a suitable enclosure in accordance with the end product standards.
- The sensor is to be powered from an intrinsically safe circuit in the end product.
- Refer to control drawing (7400-0108-011) for entity parameters and additional information.

Baseline-MOCON, Inc.

19661 HWY 36
Lyons, CO 80540
PH 303-823-6661

piD-TECH® *plus*
- Data Sheet

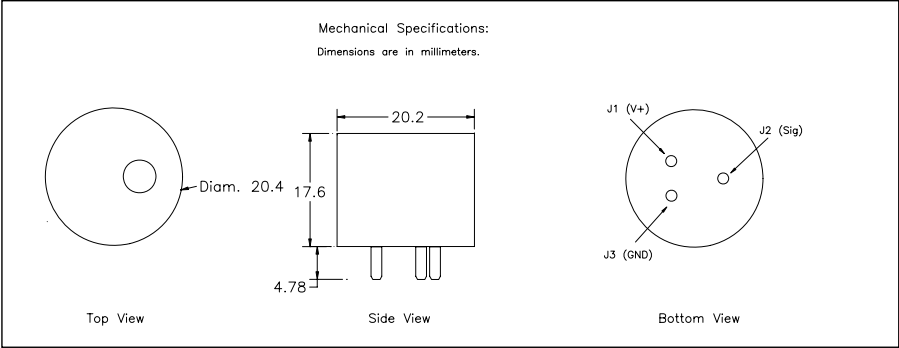
DWG No. 7400-0105-011

Rev. C

Part No. ZPP6018001

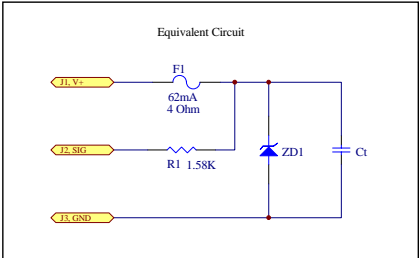
Sheet 2 of 2

Mechanical Details:




Entity Parameters:

	Pins J1,J2,J3	Comments
Vmax, Ui	10V	
Imax, li	-	The current is limited by an internal fuse.
Pi	-	Power is limited to .581W by an internal fuse, resistor and zener diodes.
Ci	0uF	
Li	0H	



Manufacturer and Applicant: Baseline-MOCON, Inc., Lyons, Colorado 80540, USA

Label Information:

0539  II 2 G EEx ia IIC
DEMKO 06 ATEX 0547796U
Ex ia IIC IECEX UL 06.0011U
Class I, Division 1, Groups A,B,C,D
Tamb = -20°C to +60°C

Note 1:
No changes permitted
without reference to
notified body.

Baseline-MOCON, Inc.		19661 HWY 36 Lyons CO 80540 PH 303-823-6661	
PiD-TECH - Control Drawing	DWG No. 7400-0108-011		Rev. B
	BMI No. ZPP60180 **		
	Date: 07/15/06	Sheet 1 of 1	



TECHNICAL DATA



RELATIVE HUMIDITY MODULE

HM 1500

Based on the rugged HS1101 capacitive humidity sensor, HM1500 is a dedicated humidity transducer designed for OEM applications where a reliable and accurate measurement is needed. Direct interface with a micro-controller is made possible with the module's linear voltage output.

MAIN FEATURES

- Small size
- Not affected by water immersion
- Full interchangeability
- High reliability and long term stability
- Typical 1 to 4 Volt DC output for 0 to 100 % RH at 5 V DC supply
- Calibrated within ± 2 % RH @ 55 % RH
- Very low temperature dependence
- Ratiometric to voltage supply within the specified range
- Suitable for 3 to 7 Volts supply voltage



HUMIDITY SENSOR SPECIFIC FEATURES

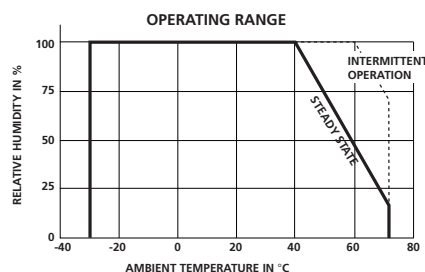
- Instantaneous de-saturation after long periods in saturation phase.
- Patented solid polymer structure.
- High resistance to chemicals.
- Fast response time.



MAXIMUM RATINGS

Ratings	Symbol	Value	Unit
Storage Temperature	T _{stg}	-30 to 70	°C
Supply Voltage (Peak)	V _s	7	Vdc
Humidity Operating Range	RH	0 to 100	% RH
Temperature Operating Range	T _a	-30 to 60	°C

Peak conditions : less than 10% of the operational time.



CHARACTERISTICS

(T_a = 23°C, V_s = 5Vdc, R_L > 1MΩ otherwise stated)

Characteristics	Symbol	Min.	Typ.	Max.	Unit.
Humidity measuring range	RH	1		99	% RH
Relative Humidity accuracy (10 to 95 % RH)	RH		± 3	± 5	% RH
Voltage supply	V _s	4.75	5.00	5.25	V
Nominal output @ RH = 55 %	V _{out}	2.42	2.48	2.54	V
Current consumption	I _c		0.4	0.8	mA
Temperature coefficient (10 to 50 °C)	T _{cc}		+ 0.1		% RH/°C
Averaged Sensitivity from 33% to 75% RH	$\Delta mV / \% RH$		+ 25		mV / % RH
Sink current capability (R _L = 15 kΩ)	I _s			300	μA
Recovery time after 150 hours of condensation	t		10		s
Humidity Hysteresis			± 1.5		% RH
Long term stability			0.5		% RH/yr
Response time (33 to 76 % RH, static, @ 63 %)	τ		10		s
Output impedance	Z		70		Ω

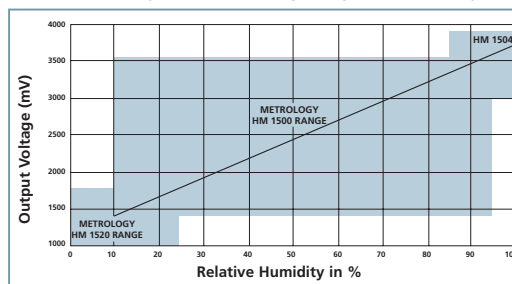


TECHNICAL DATA

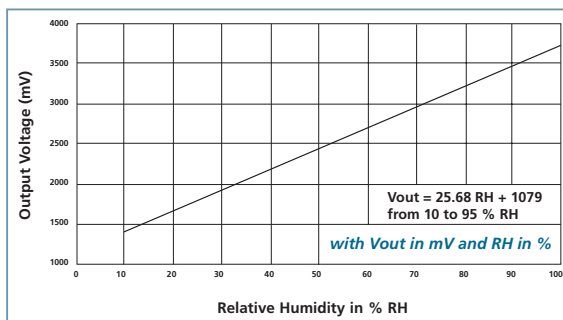
MEASUREMENT CONDITIONS

- HM1500 is specified for accurate measurements within 10 to 95% RH.
- Excursion out of this range (< 10% or > 95% RH, including condensation) does not affect the reliability of HM1500 characteristics.
- Dedicated HM15XX Product are available for extreme RH conditions (as HM1520 for low dewpoints). Consult HUMIREL for further information.

HM 1500 Typical Measuring Ranges in Humidity



HM1500 MODELLED LINEAR VOLTAGE OUTPUT (Vs = 5V)



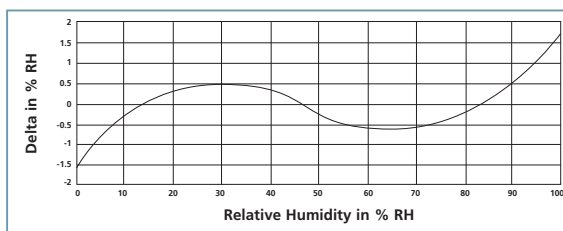
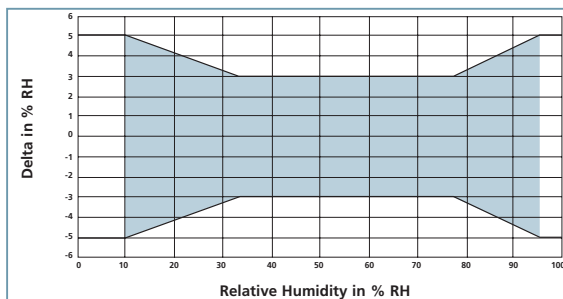
REFERENCE OUTPUT VALUES

RH (%)	$V_{out}(mV)$	RH (%)	$V_{out}(mV)$
10	1325	55	2480
15	1465	60	2605
20	1600	65	2730
25	1735	70	2860
30	1860	75	2990
35	1990	80	3125
40	2110	85	3260
45	2235	90	3405
50	2360	95	3555

Reversed Polynomial Equation

$$V_{out} = 9E^{-4}RH^3 - 1.3E^{-1}RH^2 + 30.815RH + 1030$$

ERROR BUDGET AT 23°C



HM1500 ERROR LIMITS

Temperature coefficient compensation

$$RH_{Cor}\% = RH\%_{Read} * (1 - (Ta - 23) * 2.4E^{-3})$$

Non linearity and temperature compensation

$$RH\% = \frac{-1.919E^{-9}V_{out}^3 + 1.335E^{-5}V_{out}^2 + 9.607E^{-3}V_{out} - 21.75}{1 + (Ta - 23) * 2.4E^{-3}}$$

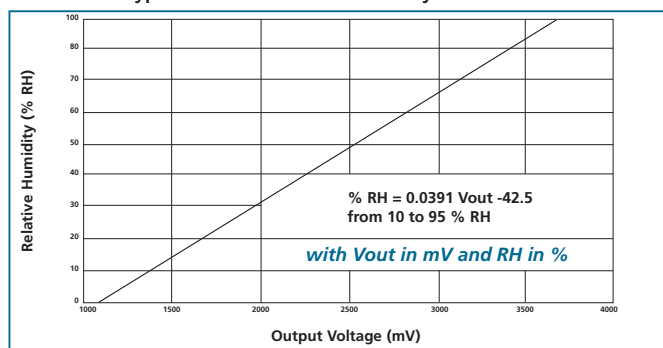
All equations V_{out} in mV, RH in %, Ta in °C.

LINEARITY ERROR OF HM1500 MODULE

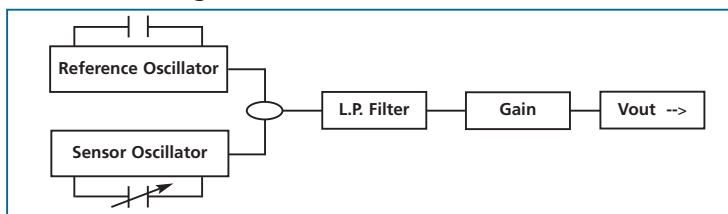


HUMIDITY MEASUREMENT USING HM1500

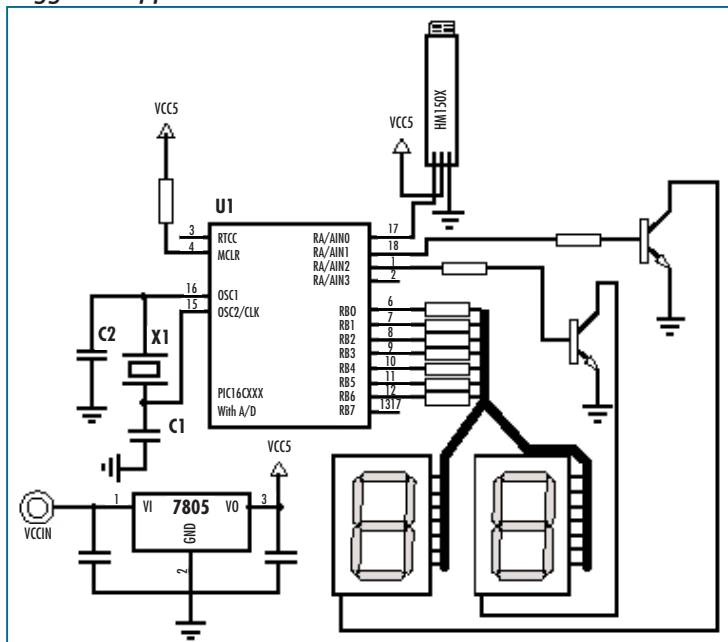
Typical HM 1500 relative Humidity measurement



Internal block diagram of HM1500

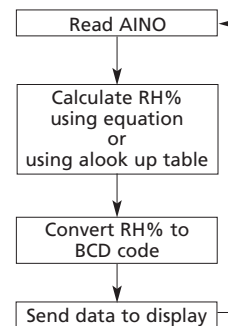


Suggested applications for HM1500



Steps of 1% RH are achievable by using 8-bit A/D.

If more resolution is required a 10-bit A/D needs to be used and a third display will be added, giving steps of 0.2% RH





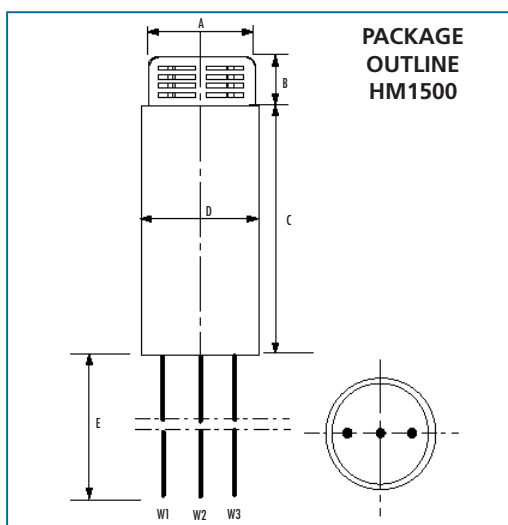
TECHNICAL 4 DATA

● RESISTANCE TO PHYSICAL AND CHEMICAL STRESSES

- HM1500 has passed through qualification processes of HUMIREL including vibration, shock, storage, high temperature and humidity, ESD.
- Additional tests under harsh chemical conditions demonstrate good operation in presence of salt atmosphere, SO₂ (0.5%), H₂S (0.5%), O₃, NO_x, NO, CO, CO₂, Softener, Soap, Toluene, acids (H₂SO₄, HNO₃, HCl), HMDs, Insecticide, Cigarette smoke, a non exhaustive list.
- HM1500 is not light sensitive.

● SPECIFIC PRECAUTIONS

- HM1500 is not protected against reversed polarity - Check carefully when connecting the device.
- If you wish to use HM1500 in a chemical atmosphere not listed above, consult us.



Dim	Min (mm)	Max (mm)
A	9.70	10.20
B	5.00	5.50
C	52	54
D	11.2	11.6
E*	200	250

* specific length available on request

Wire	Color	Function
W1	White	GROUND
W2	Blue	SUPPLY VOLTAGE
W3	Yellow	OUTPUT VOLTAGE

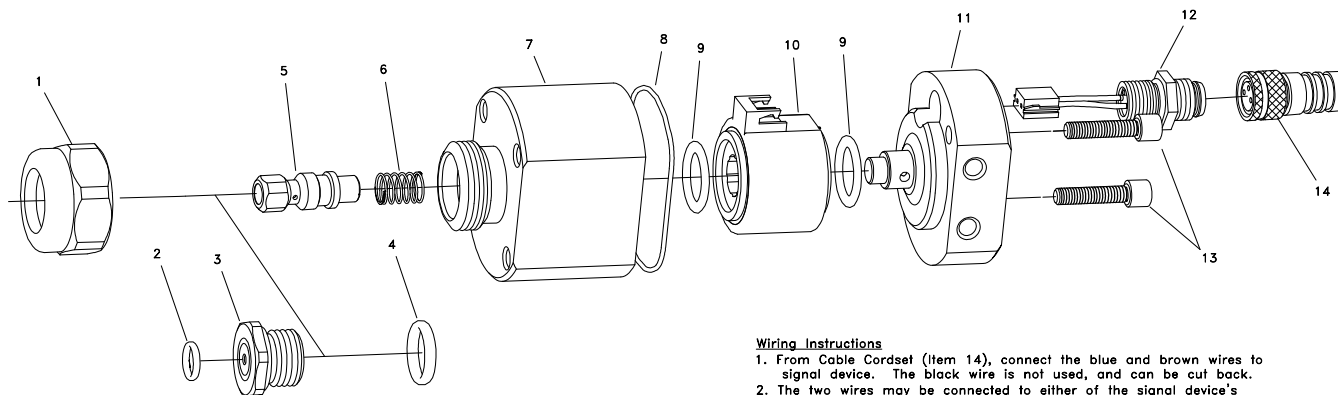
ORDERING INFORMATION (MULTIPLE PACKAGE QUANTITY OF 10 PIECES). HM1500 : HUMIDITY ANALOG VOLTAGE OUTPUT MODULE.

**SAMPLE KIT OF HM1500
IS AVAILABLE THROUGH
HUMIREL WEB SITE**

www.humirel.com

email : sales@humirel.com

The information in this sheet has been carefully reviewed and is believed to be accurate; however, no responsibility is assumed for inaccuracies. Furthermore, this information does not convey to the purchaser of such devices any license under the patent rights to the manufacturer. Humirel reserves the right to make changes without further notice to any product herein. Humirel makes no warranty, representation or guarantee regarding the suitability of its product for any particular purpose, nor does Humirel assume any liability arising out of the application or use of any product or circuit and specifically disclaims any and all liability, including without limitation consequential or incidental damages. « Typical » parameters can and do vary in different applications. All operating parameters, including « Typical » must be validated for each customer applications by customer's technical experts. Humirel does not convey any license under its patent rights nor the rights of others. Humirel products are not designed, intended, or authorized for use as components in systems intended for surgical implant into the body, or other application intended to support or sustain life, or for any application in which the failure of the Humirel product could create a situation where personal injury or death may occur. Should buyer purchase or use Humirel products for any such unintended or unauthorized application, Buyer shall indemnify and hold Humirel and its officers, employees, subsidiaries, affiliates and distributors harmless against all claims, costs, damages and expenses, and reasonable attorney fees arising out of, directly or indirectly, any claim of personal injury or death associated with such unintended or unauthorized use, even if such claim alleges that Humirel was negligent regarding the design or manufacture of the part. Humirel is a registered trade mark of Humirel.



ITEM	PART NO.	DESCRIPTION
1	CP1325-SS	Cap, Stainless Steel
* 2	CP7717-4-VI	O-Ring, Viton®
* 3	CP50693-SS	Seat Insert, Stainless Steel
* 4	CP7717-7-VI	O-Ring, Viton®
* 5	50697-VI	Plunger Sub-Asb., Type 18-FM & 302 St. Steel with Viton® Insert
* 6	CP50691-SS	Spring, Type 302 Stainless Steel
7	CP50682-18FMSS	Cover Body, NPT Version, Type 18-FM Stainless Steel
	CP50682-1-18FMSS	Cover Body, BSPT Version, Type 18-FM Stainless Steel
▲ 8	CP7717-M33.27x1.02-VI	O-Ring, Viton®
▲ 9	CP7717-2/13-VI	O-Ring, Viton® (2 Required)
▲ 10	CP50685	Coil, 24VDC, Glass-Filled PPS with NY Encapsulation
	CP50681-18FMSS	Inlet Body, 1/8 NPT, Type 18-FM Stainless Steel
11	CP50681-1-18FMSS	Inlet Body, 1/8 BSPT, Type 18-FM Stainless Steel
▲ 12	CP50686	Electrical Connector, M8 - 3 Pole (Pico Size)
▲ 13	CP72417-1/2-SSVI	Socket Hd. Screw & O-Ring Sub-Asb., St. Steel & Viton (2 Required)
● 14	50699-5-PVC	Cable Cordset, M8 - 3 Pole (Pico size), Straight Female, PVC

- ▲ Indicates item(s) included in Spare Parts Kit No. AB10000-ELEC-VI-KIT
 * Indicates item(s) included in Spare Parts Kit No. AB10000AUH-03-VI-KIT
 ● 50699-5 Cable is available in Polyurethane (PUR) as an option.

Wiring Instructions

1. From Cable Cordset (Item 14), connect the blue and brown wires to signal device. The black wire is not used, and can be cut back.
2. The two wires may be connected to either of the signal device's outputs. Polarity is not important.
3. Use of a high speed "fly back" diode may be required to help prevent reverse bias current feeding back to signal device.

Rebuild Instructions

1. Remove Cap (Item 1), and UniJet® Tip from Cover Body (Item 7).
2. Unscrew Seat Insert (Item 3) with O-rings (Items 2 and 4) from Cover Body, and allow Plunger (Item 5) and Spring (Item 6) to fall free.
3. Inspect and replace any worn items.
4. Place both O-rings on Seat Insert, and slip Spring on Plunger.
5. Insert Plunger and Spring into Nozzle, and replace Seat Insert by screwing into Cover Body.
6. Replace UniJet® Tip, and Cap.

WARNING

THIS NOZZLE IS NOT CONSIDERED TO BE EXPLOSION PROOF. USE IN AN EXPLOSIVE OR FLAMMABLE ENVIRONMENT MAY RESULT IN SEVERE INJURY OR DEATH.

DESCRIPTION:

AA10000AUH-03 &
 AA810000AUH-03
 PULSAJET® 10000
 AUTOMATIC SPRAY NOZZLE



Spraying Systems Co.
 Spray Nozzles and Accessories
 P.O. Box 7900 - Wheaton, IL 60187-7901

Rev. No. 6
 Ref.

Maintenance Instruction No.
MI 10000AUH-03
 SHEET OF

VAISALA
www.vaisala.com

GMT220 Series Carbon Dioxide Transmitters for Industrial Applications



The GMT220 transmitters withstand harsh and humid environments.

Features/Benefits

- Incorporates Vaisala CARBOCAP® - the silicon-based NDIR sensor
- IP65 protected against dust and spray water
- Several measurement ranges
- Easy installation
- Standard analog outputs and two configurable relays available

Applications include:

- Horticulture and fruit storage
- Greenhouses and mushroom farming
- Safety alarming and leakage monitoring
- Demand controlled ventilation in harsh environments

The Vaisala CARBOCAP® Carbon Dioxide Transmitter Series GMT220 is designed to measure carbon dioxide in harsh and humid environments. The housing is dust- and waterproof to IP65 standards.

The GMT220 series transmitters incorporate the advanced Vaisala CARBOCAP® Sensor. The patented sensor has unique reference measurement capabilities. Its critical parts are made of silicon; this gives the sensor outstanding stability over both time and temperature. By lengthening the calibration intervals, the user saves both time and money.

Interchangeable Probes

The user has a choice of measurement ranges up to 20% of CO₂. The GMT221 is for higher concentrations of CO₂ and the

GMT222 for lower concentrations of CO₂. The GMT220 probes are interchangeable. They can be removed and reattached or replaced at any time – without the need for calibration and adjustment. The probes can be attached directly to the transmitter body or, when used with a cable, installed remotely into hard-to-reach places or areas with dangerously high levels of CO₂.

The interchangeability of the GMT220 transmitter's probes truly facilitates field maintenance.

The end user can carry out field maintenance without any additional equipment or heavy and expensive calibration gas bottles by simply replacing a probe.

Probes that have been replaced can be sent to Vaisala for recalibration.

Technical Data

Performance

Measurement Ranges	
GMT221	0 ... 2 %
for high concentrations	0 ... 3 %
	0 ... 5 %
	0 ... 10 %
	0 ... 20 %
GMT222	0 ... 2000 ppm
for low concentrations	0 ... 3000 ppm
	0 ... 5000 ppm
	0 ... 7000 ppm
	0 ... 10 000 ppm
Accuracy (including repeatability, non-linearity and calibration uncertainty) at 25 °C and 1013 hPa	
GMT221	±(1.5 % of range + 2 % of reading)
(applies for concentrations above 2 % of full scale)	
GMT222	±(1.5 % of range + 2 % of reading)
Temperature dependence, typical	-0.3 % of reading / °C
Pressure dependence, typical	+0.15 % of reading/hPa
Long-term stability	<±5 %FS/2 years
Response time (63 %)	
GMT221	20 seconds
GMT222	30 seconds
Warm-up time	30 seconds, 15 minutes full specifications

Inputs and Outputs

Outputs	0 ... 20 or 4 ... 20 mA
	and 0 ... 10 V
	12 bits
Resolution of analog outputs	
Recommended external load:	
current output	max. 400 Ohm
voltage output	min. 1 kOhm
Two pre-or user-defined relay outputs	
Relay contacts	max. 30VAC/60VDC, 0.5A
Connections	screw terminals, 0.5 ... 1.5 mm ²
Operating voltage	16 ... 35 VDC or 24 VAC (±20%)
Power consumption	<4 W

Operating Environment

Operating temperature	-20 ... +60 °C (-4 ... +140 °F)
with display	0 ... +50 °C (+32 ... +122 °F)
Storage temperature	-30 ... +70 °C (-22 ... +158 °F)
Operating pressure (compensated range)	700 ... 1300 hPa
Humidity	0 ... 100 %RH, non-condensing
Electromagnetic compatibility	EN61326-1, Generic Environment

Mechanics

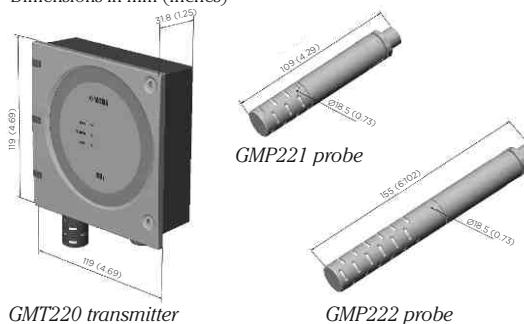
Housing material	
transmitter body	ABS plastic
probe	PC plastic
Housing classification	IP65
Weight:	
GMT221	max. 280 g
GMT222	max. 300 g
Probe cable length	2 m and 10 m (optional)

Accessories

Spare probe	GMP221, GMP222
(use the order form to define measurement range etc.)	
Clips (2 pcs) for attaching the probe	25245GM
Mounting flange for the probe	GM45156SP
Probe cables	
2 m	25665GMSP
10 m	210848GMSP
Calibrator for interchangeable probes	GMK220
Wall Assembly Plate	GM45160
In-soil adapter for probe	211921GM
Serial COM adapter	19040GM
Calibration adapter for probe	26150GM

Dimensions

Dimensions in mm (inches)



GMT220 transmitter

GMP222 probe

VAISALA

www.vaisala.com

Please contact us at
www.vaisala.com/requestinfo



Scan the code for
 more information

Ref. B210827EN-E ©Vaisala 2013

This material is subject to copyright protection, with all copyrights retained by Vaisala and its individual partners. All rights reserved. Any logos and/or product names are trademarks of Vaisala or its individual partners. The reproduction, transfer, distribution or storage of information contained in this brochure in any form without the prior written consent of Vaisala is strictly prohibited. All specifications — technical included — are subject to change without notice.





Data Sheet

4800 Series

Thermal Mass Flow

Ultra-Fast Responding
Mass Flow Controllers & Meters

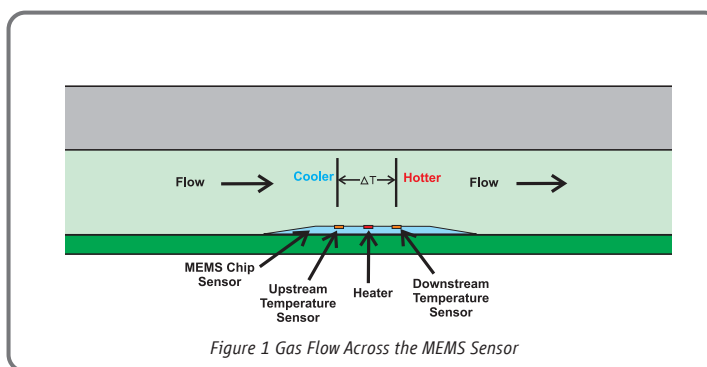
Overview

The Brooks 4800 Series features a broad flow range, compact size, a variety of analog and digital I/O options, a MEMS-based sensor that provides lightning fast response times, and many other benefits for a variety of applications. The 4800 Series of mass flow controllers and mass flow meters is fully RoHS compliant and is an excellent choice for measurement and control of many common gases including air, N_2 , O_2 , Ar, He, H_2 , CO_2 , CO, N_2O , CH_4 , C_3H_6 , and C_3H_8 . The optional Local Operator Interface (LOI) provides a convenient user interface to view, control, and configure the 4800 Series devices eliminating the need for remote secondary electronics.

Product Description

The 4800 Series MEMS-based sensor provides lightning fast response times.

The 4800 Series utilizes a Micro Electro Mechanical System (MEMS) based thermal sensor. Similar to typical thermal sensors, it measures a change in temperature to determine mass flow rate. The difference is that gas flows directly across the sensor, achieving extremely fast response times.



Product Description (Continued)

Fast settling times and stable control come standard with the 4850 controller.

The Model 4850 uses a proprietary PID algorithm to optimize the control valve response to ensure rapid settling times. The 4850 can be counted on to quickly match actual mass flow to any changes in setpoint.

Good things come in small packages.

The MEMS sensor enables a dramatic reduction in size compared to traditional thermal mass flow controllers and thermal mass flow meters. In fact the compact size of the 4800 Series 1" x 3" x 4" (25mm x 76mm x 101mm) takes up less than half the space of typical thermal mass flow controllers.

The 4800 Series is ideal for OEMs.

The broad flow range, fast response time and compact size make for a perfect fit in any OEM system where gas flow needs to be measured or controlled. You can download a free LabView VI to monitor and zero the device.

The Local Operator Interface (LOI) simplifies set-up and operation.

The LOI mounts securely on top of the 4800 Series device. With status LEDs and a large backlit LCD it provides a convenient user interface to view, control and configure the Brooks 4800 Series thermal mass flow devices. This option also allows the user to power the device with a simple power adapter that plugs right in to the wall.

RoHS compliant

Fully RoHS compliant per EU Directive 2011/65/EU.

Variety of input/output options.

The 4800 Series thermal mass flow controllers and thermal mass flow meters come standard with voltage or current and RS-232 I/O.

Easily integrated into modular gas delivery systems

The 4800 Series is available with downport connections making it easy to integrate into modular gas delivery systems.

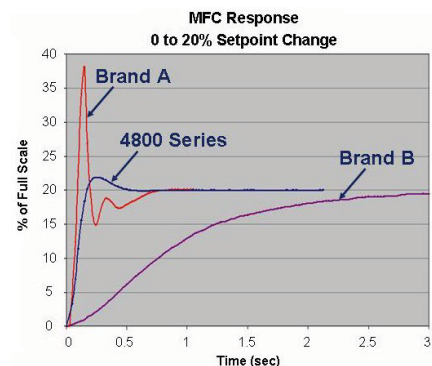


Figure 2 Fast Settling Time

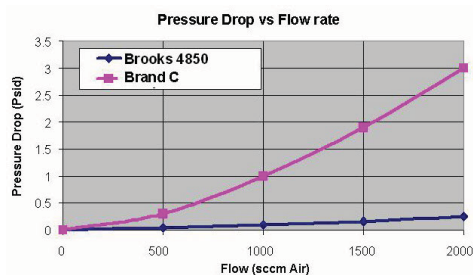


Figure 3 Low Pressure Drop

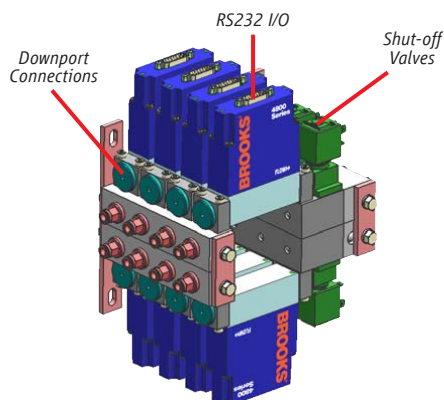
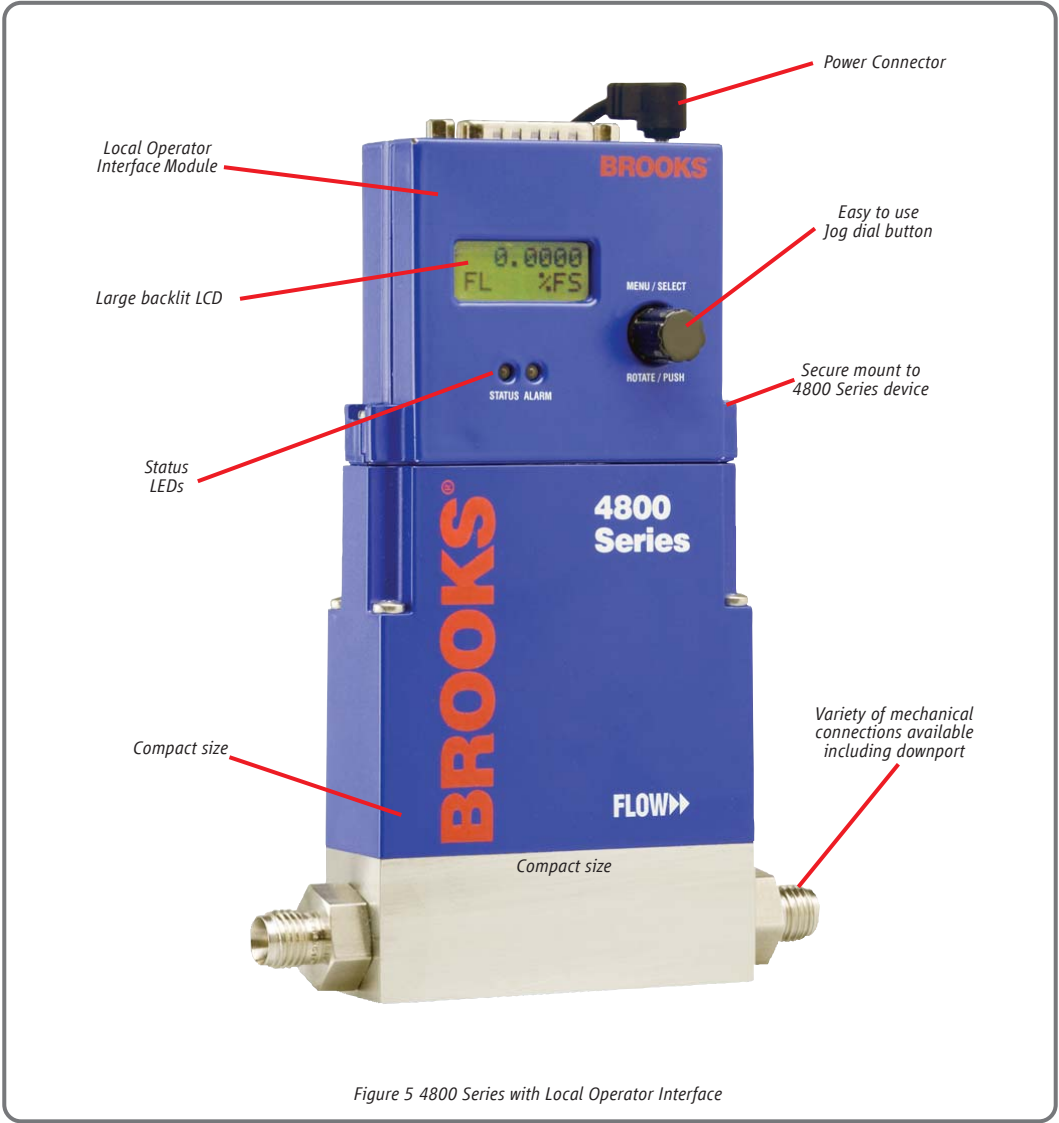


Figure 4 Modular Gas Delivery System



Features and Benefits

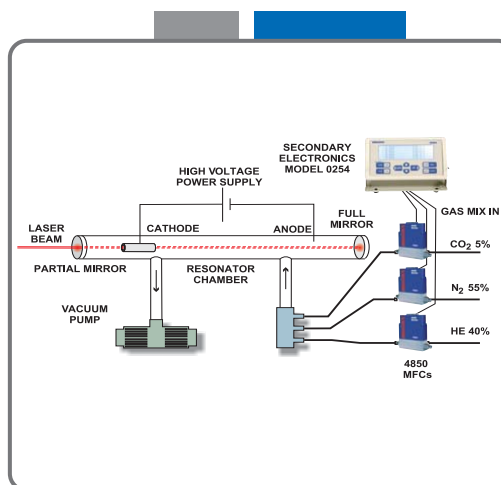
Features	Benefits
Fast response time	Ensure rapid step during process recipe changes
Compact size	Reduces space and eases installation
Optional Local Operator Interface (LOI)	Provides a turnkey solution for local indication, set point control and device configuration eliminating the need for remote secondary electronics
Low pressure drop across the sensor	Provide flow measurement with minimal pressure budget
Variety of analog and digital I/O	Easily aligns with user requirements
Fully RoHS compliant	Meets emerging environmental requirements

Product Applications

Heat Treating, Cutting/Welding, And Other Thermal Processes

The thermal process market is diverse, but the application demands are similar: reliable, accurate control of inert shielding gases and excellent control of O_2 and combustion gases to ensure that the desired outcome is achieved time after time.

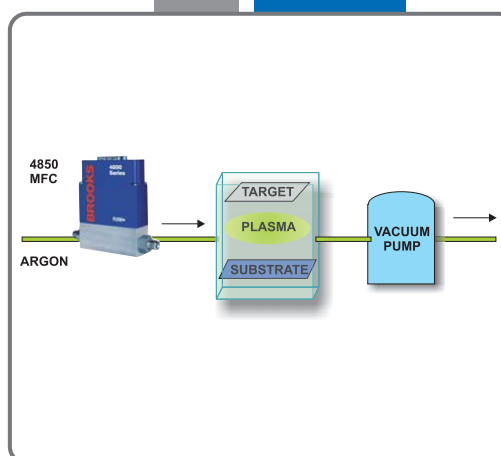
The Model 4850 provides an economical thermal mass flow control solution for flows up to 40 slpm. The 4800 Series utilizes a MEMS mass flow sensor designed specifically for inert and non-corrosive gasses such as those found in thermal applications.



Solar / Thin Film Processing (Physical Vapor Deposition)

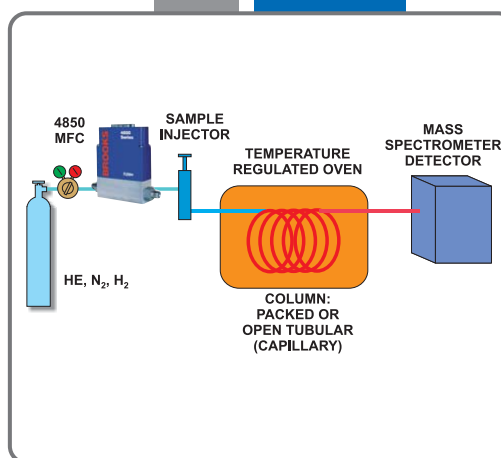
Physical vapor deposition or sputtering is commonly used for creating films of material, often metal, on a substrate. Plasma is used to move and accelerate the atoms of interest toward the target placed in a vacuum chamber. Mass flow controllers are used to control the gas flow to the chamber. Our advanced control valve PID controller can eliminate overshoot that can quench and destabilize the plasma.

The Brooks 4800 Series is a great solution for controlling argon in a plasma process. This product has a very fast response to setpoint without overshoot along with having a very small footprint.



Analytical OEM

Analytical OEMs need to measure and control reagent, calibration and sample gas flows. These applications often require that the flow control device have small physical size, low pressure drop, excellent repeatability and be easy to integrate into their system. The Brooks 4800 Series provides all this and much more. The Model 4850 mass flow controller can store multiple gas calibrations to reduce spares and inventory requirements. This product can also be private labeled for specific OEM requirements.



Product Specifications

Performance

Full Scale Flow Range	50 mL/min - 40 L/min
	(50 sccm - 40 slpm)
	(N ₂ eq., at 0°C Ref)
Control Range	2 - 100%
Flow Accuracy	+/- 3.0% of FS, +/- 1.0% FS optional
Flow Repeatability	+/- 0.15% of FS
Response Time	Flow signal: <0.3 sec
	Flow control: Settling time <0.75 sec from 0 to 100% FS (typical <0.5 sec for all steps)
Temperature Coefficient	+/- 0.1% of FS/°C (N ₂)

Ratings

Gases		Air, N ₂ , O ₂ , Ar, He, CO ₂ , CO, N ₂ O, CH ₄ , C ₃ H ₆ , C ₃ H ₈ (other gases upon request)
Operating Limits	Pressure	0 - 10 barg (0 - 150 psig)
	Temperature	0 - 50°C
	Humidity	5 to 95% R.H. (ambient)
Differential Pressure Range (Controllers)	Minimum:	0.35 bar (5 psid)
	Maximum:	10 bar (150 psid)
Leak Integrity	Inboard to Outboard: 1x10 ⁻⁹ atm scc/sec Helium max.	

Mechanical

Materials of Construction	Wetted parts: stainless steel, fluoroelastomers, silicon-based sensor
RoHS	Fully RoHS compliant per EU Directive 2011/65/EU
Outline Dimensions	Refer to Figures 6 through 8
Process Connections	Inlet/Outlet threads: 9/16" - 18 UNF threads, Refer to Figure 6 for available process connections.

Electrical

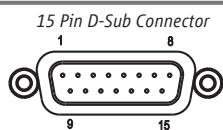
Electrical Connections	15-pin D-sub connector			
	Analog/RS-232: 15-pin D-sub connector			
Power Supply Voltage**	+15 Vdc + 10% or			
	+24 Vdc + 10%			
	Device only uses single sided power supply Inrush current: < 1 A			
Power Requirements	Model	Device	15 Vdc	
		Type	Typical (mA)	Max (mA)
	4850	Controller	130	160
	4860	Meter	30	60
			24 Vdc	
			Typical (mA)	Max (mA)
			150	200
			30	60
Analog Input/Output	0-5 Vdc or 4-20 mA			
Digital Input/Output	RS-232 (Standard with all analog I/O options)			
Valve Override Signal	Valve Controller: Input Open			
	Valve Closed: <0.3 V; open valve: >4.8 V			

** For high flows and/or low differential pressures (using orifices 0.049" (1.25mm) or 0.079" (2.0mm)) only 24 Vdc power is available.

Local Operator Interface (LOI)

Display	Effective display area: 28mm wide, 11mm high	
	Display Contents: 8x2 dot matrix display	
Operating Limits	Temperature	0-50°C
	Operating Humidity	5 to 95% R.H. (ambient)
Electrical Connections	2 15-pin D-sub connectors, one for the connection to the 4800 Series and one for the remote connection	
Power Supply Voltage	The LOI optionally includes a wall mount power adaptor with a 3.5-mm DC-plug. The adaptor works with input voltages of AC 90-240 V/47-63Hz. The adaptor supports European, U.K., Australia and U.S. wall plugs. Power can also be supplied by a remote connection via the D-connector.	
Materials of Construction	Enclosure: ABS plastic with CU-Ni plating	
RoHS	Fully RoHS compliant per EU Directive 2011/65/EU.	
Outline Dimensions	Refer to Figure 8	

Product Dimensions



PIN#	4800 Series / LOI
1	Setpoint Signal Common
2	Flow Voltage Output
3	Not used
4	Flow Current Output
5	Positive Supply Voltage
6	Not used
7	Setpoint Current Input
8	Setpoint Voltage Input
9	Power Supply Common
10	Flow Signal Common
11	Not used
12	Valve Override Input
13	Not used
14	RXD
15	TXD

Table 1 4800 Series Pin-Out Diagram

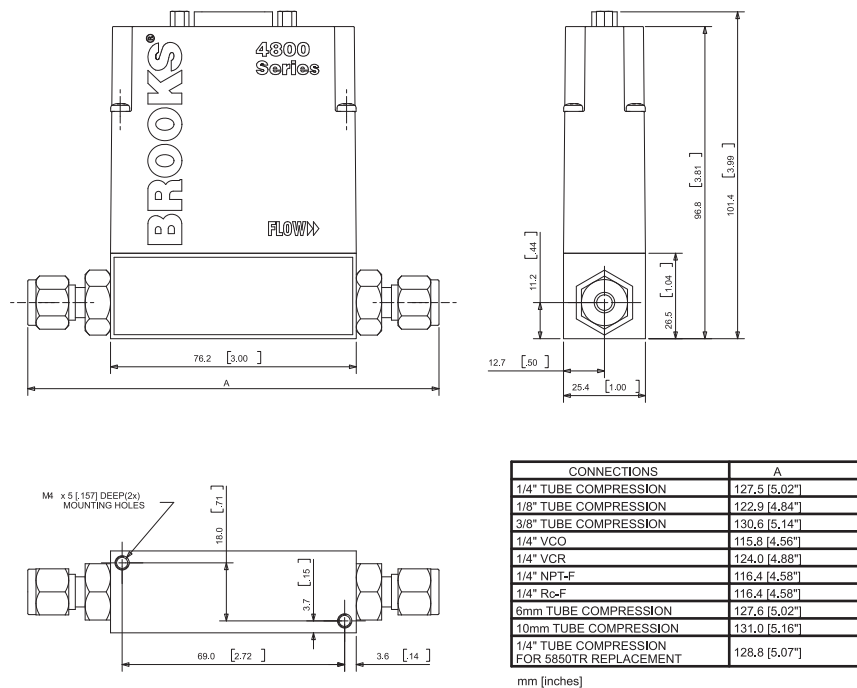
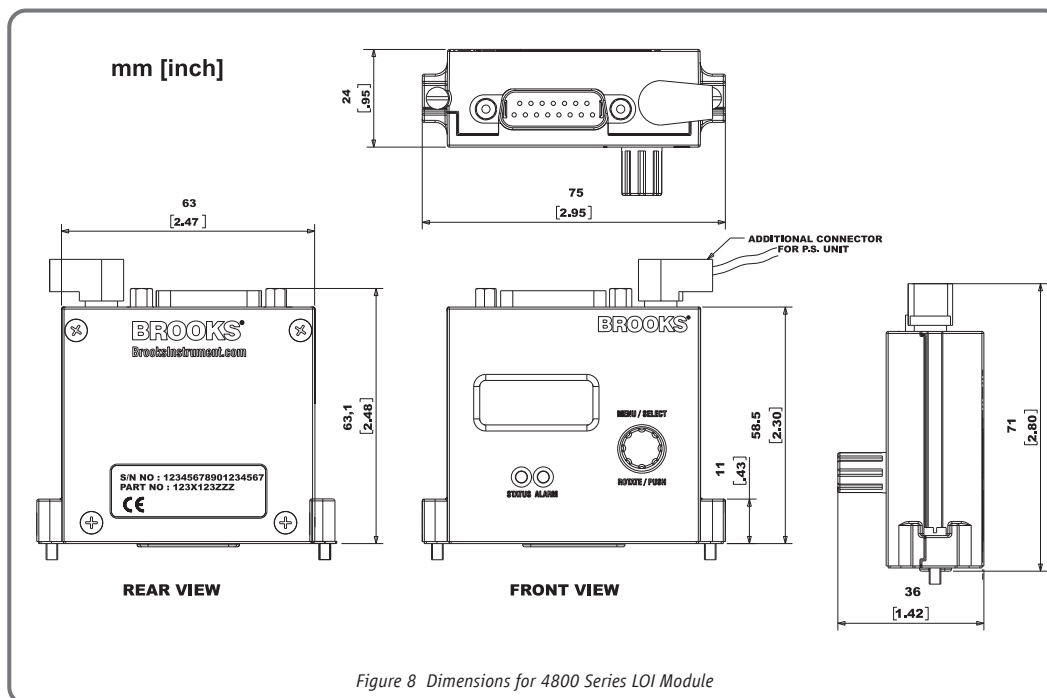
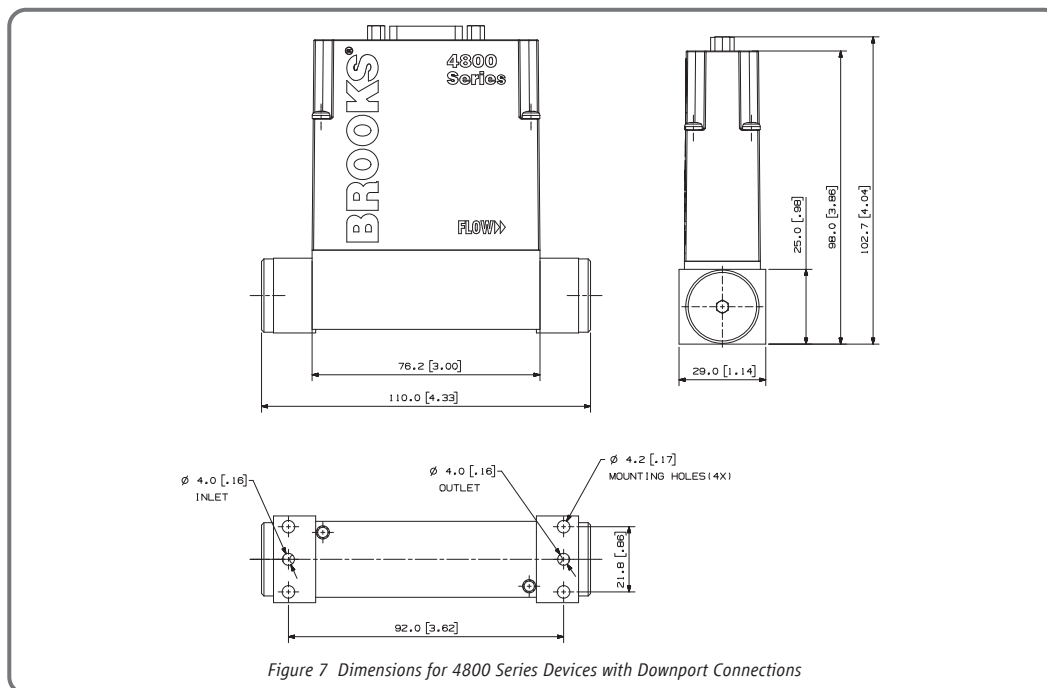


Figure 6 Dimensions for 4800 Series Devices with Standard Process Connections

Product Dimensions



Product Certifications

These certifications cover the 4800 Series thermal mass flow devices as well as the Local Operator Interface (LOI).

EMC Directive 2004/108/EC: per EN 61326:2006

Hazardous Location Classification

The modules shall be installed in a suitable enclosure providing a degree of protection of at least IP54 according to EN 60529, taking into account the environmental conditions under which the equipment will be used. Provisions shall be made to prevent the rated voltage from being exceeded by transient disturbances of more than 40%.

Enclosure: Type 1/IP40

Ambient Temperature:

$0^{\circ}\text{C} \geq \text{Tamb} \leq 50^{\circ}\text{C}$ ($32^{\circ}\text{F} \geq \text{Tamb} \leq 122^{\circ}\text{F}$)

United States and Canada



Non-Incendive
Class 1, Division 2
Groups A, B, C&D; T4

150464

Per UL 1604 and CSA-C22.2 no. 213-m87

Class 1, Zone 2, AEx nA II T4

ANSI/UL 60079-15

Ex nA II T4

Per CSA - E60079-15.02

CSA C22.2 No. 60529-05

Europe - ATEX Directive 94/9/EC

KEMA 06ATEX 0251X EN 60079-0: 2006 EN 60079-15:2005



II 3G Ex nA II T4



Pressure Equipment Directive (97/23/EC):

Sound Engineering Practice

Model Code

Code Description		Code	Option	Option Description			
I.	Base Model Number		4850	Flow Controller, Body 0 (50 sccm-40 slpm)			
			4860	Flow Meter, Body 0 (50 sccm-40 slpm)			
II.	Digital I/O Communications		A	RS-232 + Analog, Select applicable analog I/O			
III.	Model Revision Level		B	Revision			
IV.	Analog I/O, Input/ Output		B	0-5 Vdc / 0-5 Vdc			
			C	4-20 mA / 4-20 mA			
			D	0-5 Vdc / 4-20 mA			
			E	4-20 mA / 0-5 Vdc			
			0	None			
V.	Power Supply		1	15 Vdc			
			2	24 Vdc			
VI.	Mechanical Connections		1A	9/16" -18unf straight thread			
			B1	1/4" tube compression w/filter			
			C1	1/8" tube compression w/filter			
			D1	3/8" tube compression w/filter			
			E1	1/4" VCR w/filter			
			F1	1/4" VCO w/filter			
			G1	1/4" NPT-F w/filter			
			H1	6mm tube compression w/filter			
			J1	10mm tube compression w/filter			
			S1	Downport, no O-ring cavity			
			T1	1/4" Rc (BSPT) w/filter			
			X1	Downport, with O-ring cavity			
			Y1	1/4" tube w/filter (5850TR replace)			
VII.	Body			Body	O-Ring Seal	Seat	Valve Type
			A	316ss	Viton	None (Meter Only)	None (Meter Only)
			B	316ss	Viton	Viton	Normally Closed
VIII.	Area Classification		1	Standard Location (Safe Area)			
			2	ATEX Zone 2			
			4	CSA Div 2/Zone 2 (Recognized)			
IX.	Valve Orifice Size		A	No Orifice (Meter Only)			
			B	0.001 inch / 0.03mm			
			C	0.002 inch / 0.05mm			
			D	0.003 inch / 0.08mm			
			E	0.005 inch / 0.125mm			
			F	0.008 inch / 0.2mm			
			G	0.012 inch / 0.315mm			
			H	0.020 inch / 0.5mm			
			J	0.031 inch / 0.8mm			
			K	0.049 inch / 1.25mm only available with power supply option code=2 (24 Vdc)			
			M	0.079 inch / 2.0mm only available with power supply option code=2 (24 Vdc)			

Model Code

Code Description	Code Option	Option Description
X. Mass Flow Restrictor Type		Type or Restrictor
		Restrictor Range (sccm N₂ Equivalent @ 0 Deg C ref)
	A	No Restrictor
	C	Plug
	K	K
	M	M
	N	N
	P	P
	Q	Q
	R	R
	S	S
	T	T
	U	U
	V	V
	W	W
	X	X
	Y	Y
	1	1
	2	2
	3	3
	4	4
	5	5
XI. Calibration		Calibration Condition
		Accuracy
		Tracability
	A	None-Uncalibrated
	B	Single Gas
	C	Single Gas
XII. Accessories	0	None
	1	LOI with Power Adapter
	2	LOI without Power Adapter
XIII. Certificates	0	None
	9	Multiple Certs. Describe required certs in notes. Add all applicable changes to list price.
	A	Declaration of Compliance 2.1 (Certificate of Conformance)
	B	Declaration of Compliance 2.1 Leak Test
	C	Declaration of Compliance 2.1 Pressure Test
	D	Declaration of Compliance 2.1 Oxygen Service
XIV. OEM Code	A	Standard Brooks Label

Sample Model Code

I	II	III	IV	V	VI	VII	VIII	IX	X	XI	XII	XIII	XIV
4850	A	B	B	1	1A	A	2	D	K	E	2	9	A

Brooks Service and Support

Brooks is committed to assuring all of our customers receive the ideal flow solution for their application, along with outstanding service and support to back it up. We operate first class repair facilities located around the world to provide rapid response and support. Each location utilizes primary standard calibration equipment to ensure accuracy and reliability for repairs and recalibration and is certified by our local Weights and Measures Authorities and traceable to the relevant International Standards.

Visit www.BrooksInstrument.com to locate the service location nearest to you.

START-UP SERVICE AND IN-SITU CALIBRATION

Brooks Instrument can provide start-up service prior to operation when required. For some process applications, where ISO-9001 Quality Certification is important, it is mandatory to verify and/or (re)calibrate the products periodically. In many cases this service can be provided under in-situ conditions, and the results will be traceable to the relevant international quality standards.

CUSTOMER SEMINARS AND TRAINING

Brooks Instrument can provide customer seminars and dedicated training to engineers, end users, and maintenance persons.

Please contact your nearest sales representative for more details.

HELP DESK

In case you need technical assistance:

Americas	☎ 1 888 554 FLOW
Europe	☎ +31 (0) 318 549 290
Asia	☎ +81 (0) 3 5633 7100

Due to Brooks Instrument's commitment to continuous improvement of our products, all specifications are subject to change without notice.

TRADEMARKS

Brooks	Brooks Instrument, LLC
LabView IV	National Instruments
VCO	Cajon Co.
VCR	Cajon Co.
Viton	DuPont Performance Elastomers

DS-TMF-4800-MFC-eng (0913)



Brooks Instrument
407 West Vine Street
P.O. Box 903
Hatfield, PA 19440-0903 USA
T (215) 362 3700
F (215) 362 3745
E-Mail BrooksAm@BrooksInstrument.com
www.BrooksInstrument.com

Brooks Instrument
Neonstraat 3
6718 WX Ede, Netherlands
T +31 (0) 318 549 300
F +31 (0) 318 549 309
E-Mail BrooksEu@BrooksInstrument.com

Brooks Instrument
1-4-4 Kitasuna Koto-Ku
Tokyo, 136-0073 Japan
T +81 (0) 3 5633 7100
F +81 (0) 3 5633 7101
E-Mail BrooksAs@BrooksInstrument.com

BROOKS[®]
INSTRUMENT

BIBLIOGRAPHY

- [1] Nist/sematech e-handbook of statistical methods. Web. 12 June 2014. <<http://www.itl.nist.gov/div898/handbook/>>.
- [2] Rosana M. Alberici and Wilson F. Jardim. Photocatalytic destruction of vocs in the gas-phase using titanium dioxide. *Applied Catalysis B: Environmental*, 14(1-2):55 – 68, 1997.
- [3] Pangarkar V. G. Bhatkhande, D. S. and A. A. Beenackers. Photocatalytic degradation for environmental applications - a review. *Journal of Chemical Technology and Biotechnology*, 77:102–116, Jan 2002.
- [4] Xuesen Bian, Jianqiu Chen, and Rong Ji. Degradation of 2,4-dichlorophenoxyacetic acid (2,4-d) by novel photocatalytic material of tourmaline-coated tio2 nanoparticles: Kinetic study and model. *Materials*, 6(4):1530–1542, 2013.
- [5] F.J. Blanco-Silva. *Learning SciPy for Numerical and Scientific Computing*. Community experience distilled. Packt Publishing, Limited, 2013.
- [6] Richard L. Bowers and James R. Wilson. *Numerical Modeling in Applied Physics and Astrophysics*. Jones and Bartlett Publishers, Boston, MA 02116, 1991.
- [7] J.P. Boyd. *Chebyshev and Fourier Spectral Methods: Second Revised Edition*. Dover Books on Mathematics. Dover Publications, 2001.
- [8] Marissa Choquette-LabbÃl, Wudneh A. Shewa, Jerald A. Lalman, and Saravanan R. Shanmugam. Photocatalytic degradation of phenol and phenol derivatives using a nano-tio2 catalyst: Integrating quantitative and qualitative factors using response surface methodology. *Water*, 6(6):1785–1806, 2014.
- [9] Delta-T Devices. *Equitensiometer. Soil matric potential sensor; Type EQ2, User Manual*, 1999.
- [10] Kristof Demeestere, Jo Dewulf, and Herman Van Langenhove. Heterogeneous photocatalysis as an advanced oxidation process for the abatement of chlorinated, monocyclic aromatic and sulfurous volatile organic compounds in air: State of the art. *CRITICAL REVIEWS IN ENVIRONMENTAL SCIENCE AND TECHNOLOGY*, 37(6):489–538, 2007.
- [11] A. Devert. *Matplotlib Plotting Cookbook*. Packt Publishing, Limited, 2014.
- [12] "Spyder 2.2 documentation". *Spyder - Documentation*. Web. 20 May 2014. <<https://pythonhosted.org/spyder/>>.
- [13] Umar Ibrahim Gaya and Abdul Halim Abdullah. Heterogeneous photocatalytic degradation of organic contaminants over titanium dioxide: A review of fundamentals, progress and problems. *Journal of Photochemistry and Photobiology C: Photochemistry Reviews*, 9(1):1 – 12, 2008.
- [14] G.H. Golub and J.M. Ortega. *Scientific Computing and Differential Equations: An Introduction to Numerical Methods*. Academic Press, 1992.

- [15] Kaishu Guan. Relationship between photocatalytic activity, hydrophilicity and self-cleaning effect of tio2/sio2 films. *Surface and Coatings Technology*, 191(2&A3):155 – 160, 2005.
- [16] B. Gustafsson. Numerical boundary conditions. In B. E. Engquist, S. Osher, and R. C. J. Somerville, editors, *Large-Scale Computations in Fluid Mechanics*, pages 279–308. AMS, Providence, 1985. Lectures in Applied Mathematics, Vol. 22, Part 1.
- [17] Jean-Marie Herrmann. Heterogeneous photocatalysis: fundamentals and applications to the removal of various types of aqueous pollutants. *Catalysis Today*, 53(1):115 – 129, 1999.
- [18] D. Hoff. Two existence theorems for systems of conservation laws with dissipation. In C. Carasso, P.-A. Raviard, and D. Serre, editors, *Lecture Notes in Mathematics, 1270*, pages 181–194, Berlin, 1986. Springer-Verlag. Nonlinear Hyperbolic Problems. Proceedings of an Advanced Research Workshop held in St. Etienne, France, January 13-17, 1986.
- [19] J. D. Hunter. Matplotlib: A 2d graphics environment. *Computing In Science & Engineering*, 9(3):90–95, 2007.
- [20] Eric Jones, Travis Oliphant, Pearu Peterson, et al. SciPy: Open source scientific tools for Python, 2001–.
- [21] Akira Fujishima Kazuhito Hasimoto, Hiroshi Irie. Tio₂ photocatlysis: A historical overview and future prospects. *Japanese Journal of Applied Physics*, 44(12):8269–8285, 2005.
- [22] Arthit Neramittagapong Kittipon Kasipar Suphakij Khaownetr Sinsupha Chuichulcherm Kitirote Wantala, Sutasinee Neramittagapong. Photocatalytic degradation of alachlor on fe-tio2-immobilized on gac under black light irradiation using box-behnken design. *Materials Science Forum*, 734:306 – 316, 2013.
- [23] Bin Zhao Wei Wei Dannong He Belin He Qunwei Tang Lin Lin, Yuchao Chai. Photocatalytic oxidation for degradation of vocs. *Open Journal of Inorganic Chemistry (OJIC)*, 2013.
- [24] Igor N. Martyanov and Kenneth J. Klabunde. Photocatalytic oxidation of gaseous 2-chloroethyl ethyl sulfide over tio2. *Environmental Science and Technology*, 37(15):3448–3453, 2003.
- [25] Low G.K.C. Matthews R.W., Abdullah M. Photocatalytic oxidation for total organic carbon analysis. *Analytica Chimica Acta*, 223:171–179, 1990.
- [26] T. May. *Boundary Conditions in the Numerical Integration of Hyperbolic Equations*. PhD thesis, University of Reading, Reading, May 1978.
- [27] W. McKinney. *Python for Data Analysis: Data Wrangling with Pandas, NumPy, and IPython*. O'Reilly Media, 2012.
- [28] A. D. Mcnaught and A. Wilkinson. *IUPAC. Compendium of Chemical Terminology, 2nd ed. (the "Gold Book")*. WileyBlackwell; 2nd Revised edition edition, August.
- [29] Kazuya Nakata and Akira Fujishima. Tio₂ photocatalysis: Design and applications. *Journal of Photochemistry and Photobiology C: Photochemistry Reviews*, 13(3):169 – 189, 2012.
- [30] C. Precord. *Wxpython 2.8 Application Development Cookbook*. Packt Publishing, Limited, 2010.

- [31] Noel Rappin and Robin Dunn. *WxPython in action*. Manning, Greenwich, Conn, 2006.
- [32] P. L. Roe and B. van Leer. Non-existence, non-uniqueness and slow convergence in discrete conservation laws. In K. W. Morton and M. J. Baines, editors, *Numerical Methods for Fluid Dynamics III*, pages 520–529, Oxford, 1988. ICFD, Oxford University Press.
- [33] J.M. Stewart. *Python for Scientists*. Cambridge University Press, 2014.
- [34] Shaobin Wang, H.M. Ang, and Moses O. Tade. Volatile organic compounds in indoor environment and photocatalytic oxidation: State of the art. *Environment International*, 33(5):694 – 705, 2007.
- [35] Jian Li Wenjun Liang and Hong He. Photo-catalytic degradation of volatile organic compounds (vocs) over titanium dioxide thin film. *Journal of Photochemistry and Photobiology C: Photochemistry Reviews*, 2012.
- [36] Hai Yang, Shuolin Zhou, Huajie Liu, Weiwei Yan, Liping Yang, and Bing Yi. Photocatalytic degradation of carbofuran in tio2 aqueous solution: Kinetics using design of experiments and mechanism by hplc/ms/ms. *Journal of Environmental Sciences*, 25(8):1680 – 1686, 2013.
- [37] W. Zhang. *Advanced Technology in Teaching: Selected papers from the 2012 International Conference on Teaching and Computational Science (ICTCS 2012)*. Advances in Intelligent and Soft Computing. Springer, 2012.